PolyPublie
Polytechnique Montréal

POLYTECHNIQUE MONTRÉAL
UNIVERSITÉ D'INGÉNIERIE

Titre: Title:	Wide-Field Spatial Frequency Domain Imaging, Diffuse Reflectance and Endogenous Fluorescence Spectroscopy System for Quantitative Tissue Biomarkers in Radical Prostatectomy Specimens
Auteur: Author:	Emile Beaulieu
Date:	2019
Type:	Mémoire ou thèse / Dissertation or Thesis
Référence: Citation:	Beaulieu, E. (2019). Wide-Field Spatial Frequency Domain Imaging, Diffuse Reflectance and Endogenous Fluorescence Spectroscopy System for Quantitative Tissue Biomarkers in Radical Prostatectomy Specimens [Mémoire de maîtrise, Polytechnique Montréal]. PolyPublie. https://publications.polymtl.ca/4023/

Document en libre accès dans PolyPublie
Open Access document in PolyPublie

URL de PolyPublie: PolyPublie URL:	https://publications.polymtl.ca/4023/
Directeurs de recherche: Advisors:	Frédéric Leblond, & Dominique Trudel
Programme: Program:	Génie physique

Ce fichier a été téléchargé à partir de PolyPublie, le dépôt institutionnel de Polytechnique Montréal
This file has been downloaded from PolyPublie, the institutional repository of Polytechnique Montréal

https://publications.polymtl.ca

POLYTECHNIQUE MONTRÉAL
affiliée à l'Université de Montréal

Wide-field spatial frequency domain imaging, diffuse reflectance and endogenous fluorescence spectroscopy system for quantitative tissue biomarkers in radical prostatectomy specimens

EMILE BEAULIEU
Département de génie physique

Mémoire présenté en vue de l'obtention du diplôme de *Maîtrise ès sciences appliquées*
Génie physique

Août 2019

© Emile Beaulieu, 2019.

POLYTECHNIQUE MONTRÉAL
affiliée à l'Université de Montréal

Ce mémoire intitulé :

Wide-field spatial frequency domain imaging, diffuse reflectance and endogenous fluorescence spectroscopy system for quantitative tissue biomarkers in radical prostatectomy specimens

présenté par **Emile BEAULIEU**
en vue de l'obtention du diplôme de *Maîtrise ès sciences appliquées*
a été dûment accepté par le jury d'examen constitué de :

Jean PROVOST, président
Frédéric LEBLOND, membre et directeur de recherche
Dominique TRUDEL, membre et codirectrice de recherche
Samuel KADOURY, membre

DEDICATION

To my mother and father

ACKNOWLEDGEMENTS

I extend very special thanks to my supervisor Prof. Frederic Leblond, who gave me the opportunity to participate in this project; leading me to work on a stimulating problematic in a practical context and a novel, interesting clinical environment, as well as steering the course of my future career. His extensive knowledge of the field and creative ideas were always able to provide a new perspective on problems. Completing my master's degree as part of his team has been a very enriching and pleasant experience, and I have no doubt I will continue to hear of the laboratory in the future.

I also show gratitude to all my colleagues in the LRO and CRCHUM for their invaluable help. Thank you to Audrey Laurence for her crucial help on SFDI, without her this part of the project would not have yielded such satisfactory results, and many other aspects of my system; to Guillaume Sheehy and Fabien Picot for the common *Modern Optics* laboratory charges and precious knowledge of various facets of programming; to Mirela Birlea, Hamida Claudia Syed and my co-director Dominique Trudel for dutifully obtaining prostate specimens and commenting histopathological stainings; to Alireza Akbarzadeh for the help with the redaction of this thesis; to Leticia Angulo for helping kick-start my work on the project; and to Amélie Saint-Georges of the microfluidics for oncology laboratory for the help on the elaboration of the calibration processes.

I would also like to thank members of the Polytechnique's engineering physics department, especially Jean-Paul Lévesque for his technical know-how and incredible readiness to help, as well as Lyne Dénommé for her assistance with all administrative manners.

RÉSUMÉ

La seule approche chirurgicale présentement utilisée pour le traitement du cancer de la prostate est le retrait complet de l'organe ; la prostatectomie radicale. Similairement à d'autres procédures de résection du cancer, une importante mesure du succès de l'opération est le degré auquel le cancer a été retiré du patient, car les chances de récurrence sont augmentées par la présence de cancer résiduel. Puisque la prostate est entourée de structures génito-urinaires importantes relativement à la qualité de vie du patient, retirer l'entièreté de la prostate tout en évitant d'impacter les structures avoisinantes est une tâche complexe. Par ailleurs, la navigation chirurgicale en prostate nécessite de grandes améliorations étant donné l'inexistence de modalités d'imagerie compatibles pour des méthodes de recalage avec ce cancer, et la faible précision et le peu d'informations spatiales fournies par les méthodes diagnostiques actuelles. Il y a un réel besoin de nouveaux outils permettant la différenciation de tissus lors de la prostatectomie radicale et ainsi la résection ciblée des tissus.

La fluorescence endogène est une technique d'imagerie donnant accès à des informations moléculaires sur un échantillon et a été utilisée dans maintes applications pour la caractérisation de tissus. La méthode a été appliquée sur les tissus prostatiques avec des sondes ponctuelles, mais n'a pas trouvé d'usage en champ de vue macroscopique. Cependant, sans traitement, la fluorescence n'est pas un reflet direct du contenu moléculaire, puisqu'elle est en compétition avec d'autres processus comme l'absorption et la diffusion élastique. À cet effet, des méthodes corrigeant l'absorption et la diffusion ont été élaborées à partir de mesures de réflectance diffuse. Celles-ci étaient limitées aux géométries ponctuelles jusqu'au développement de l'imagerie dans le domaine des fréquences spatiales (*spatial frequency domain imaging*, SFDI), qui permet la reconstruction des coefficients d'absorption (μ_a) et de diffusion (μ_s') en grand-champ. Toutefois, les techniques de correction de fluorescence dérivées du SFDI n'ont été appliquées qu'à des agents de fluorescence externes. Ainsi, ce projet présente un système multimodal grand-champ combinant fluorescence endogène, réflectance diffuse et SFDI pour obtenir des informations moléculaires quantitatives sur des spécimens de prostatectomie radicale.

Premièrement, les modalités de fluorescence, réflectance et SFDI ont été intégrées dans un système d'imagerie avec des spécifications adaptées aux échantillons de prostates ; soit un champ de vue de 5.5 x 5.5 cm, résolution spatiale de 70 μm et profondeur de champ de 1.5 cm. Les processus de calibration ont été élaborés et les paramètres d'acquisition optimisés à l'aide de mesures sur des fantômes optiques. Ces mesures ont permis d'établir la précision

du SFDI à 5.2% pour l'absorption et 4.4% pour la diffusion ; des performances similaires à d'autres systèmes dans la littérature. L'algorithme de quantification de fluorescence implémenté a aussi permis d'augmenter significativement la corrélation entre l'intensité mesurée et la concentration réelle de fluorophore.

Deuxièmement, le système a été adapté à l'utilisation sur des échantillons biologiques, entre autres par l'implémentation de polariseurs croisés pour contrôler les réflexions spéculaires et d'un algorithme de profilométrie pour appliquer des corrections géométriques à la reconstruction SFDI ; réduisant les erreurs de 127% à 3.3% pour μ_a et de 28% à 2.5% pour μ'_s sur une variation en hauteur de 24 mm. Des mesures ont été prises sur un spécimen de prostatectomie radicale et comparées à des colorations histologiques. Les résultats d'analyses statistiques préliminaires sur toutes les modalités ont démontré un potentiel statistiquement significatif de différenciation entre les tissus prostatiques *vs* extra-prostatiques, et bénins *vs* cancéreux. Bien que le nombre d'échantillons analysés soit trop bas pour prononcer des conclusions immédiates sur la performance des biomarqueurs acquis, des mesures supplémentaires sur d'autres spécimens permettraient une analyse statistique plus complète et ainsi une transition vers une application *in vivo* de différenciation des tissus lors de prostatectomies radicales assistées par robotique.

ABSTRACT

The only current surgical approach to the treatment of prostate cancer is radical prostatectomy, which enforces the complete resection of the organ. Similarly to other forms of cancer resection, the degree of success of the surgery is directly influenced by the completeness of cancer removal, as residual cancer increases the risks of recurrence. Because the prostate is close to critical genitourinary structures with a high impact on patient quality-of-life, achieving complete resection with a minimum amount of side-effects on the surrounding tissues is a challenging task. Surgical guidance in the prostate requires vital improvement due to the lack of proper co-registration imaging methods and inaccurate diagnostic techniques which give very limited spatial information. Consequently, there is a need for new tools to characterize tissue during radical prostatectomy and guide resection.

Endogenous fluorescence provides molecular information from the tissue and thus has found use for tissue characterization in multiple applications. Although the technique was applied to prostate tissue in point probes, it has never been explored in macroscopic geometries. Fluorescence also competes with other optical events like absorption and elastic scattering, which makes it indirectly related to tissue molecular content. Optical properties derived from diffuse reflectance measurements can be used to correct these optical events and compute quantified fluorescence. Such correction models were limited to point geometries until the development of the spatial-frequency domain imaging (SFDI) technique, which allowed the extraction of absorption (μ_a) and scattering (μ'_s) coefficients in wide-field configurations. However, SFDI-based quantification has only been applied to external fluorescence agents. This project presents the development of a wide-field multimodal system that combines endogenous fluorescence, diffuse reflectance, and SFDI to obtain quantitative molecular information from radical prostatectomy samples.

At first fluorescence, reflectance and SFDI were integrated into a single system with a field of view of 5.5 x 5.5 cm, spatial resolution of 70 μm and depth of field of 1.5 cm adapted to the prostate samples. Calibration processes and acquisition parameters were determined with experiments on optical phantoms. SFDI reconstruction was accurate within 5.2% and 4.4% for absorption and scattering respectively; performances similar to other systems in the literature. Quantification of fluorescence also resulted in a significant increase in the correlation of measured intensity to fluorophore concentration.

Subsequently, the system was modified for use on biological samples, notably with the addition of crossed polarisers to control specular reflections and sample-geometry corrections

for SFDI based on a profilometry algorithm; the latter which reduced errors from 127% to 3.3% for μ_a and from 28% to 2.5% for μ_s' over a 24 mm height variation. Measurements were conducted on radical prostatectomy specimens and the results were compared to histopathological stainings. Preliminary statistical analyses on all modalities indicated statistically significant potential for differentiation between prostatic *vs* extra-prostatic tissue, and benign *vs* malign tissue. While the sample number was too low to prove the performance of the acquired biomarkers, additional measurements on prostate samples would allow to complete statistical analyses and pave the way for translation of the system to *in vivo* tissue differentiation during robot-assisted radical prostatectomy.

TABLE OF CONTENTS

LIST OF TABLES

LIST OF FIGURES

LIST OF SYMBOLS AND ACRONYMS

5-ALA	5-Aminolevulinic Acid
AFLS	Autofluorescence Lifetime Spectroscopy
ANSI	American National Standards Institute
CHUM	Centre Hospitalier de l'Université de Montréal
FDA	Food and Drug Administration
DLP	Digital Light Processing
FI	Fluorescence Imaging
FLIM	Fluorescence Lifetime Imaging Microscopy
FOV	Field of View
FRAP	Fluorescence Recovery After Photobleaching
FRET	Fluorescence Resonance Energy Transfer
HE	Hematoxylin and Eosin
IQR	Interquartile range
LED	Light-Emitting Diode
LCTF	Liquid Crystal Tunable Filter
LLG	Liquid Light Guide
MC	Monte-Carlo
PCa	Prostate cancer
PpIX	Protoporphyrin IX
Q1-Q2-Q3-Q4	Quartile 1,2,3,4
QF	Quantified Fluorescence
RP	Radical prostatectomy
S3	Stokes Shift Spectroscopy
SFDI	Spatial Frequency Domain Imaging
SNR	Signal to Noise Ratio
STD	Standard Deviation
UV	Ultra Violet

LIST OF APPENDICES

CHAPTER 1 INTRODUCTION

1.1 Problematic and theoretical framework

Prostate Cancer (PCa) is the most common cancer among American men and the second leading cause of cancer-related death, making it a high-priority health issue [7–9]. The only current surgical treatment for PCa is Radical Prostatectomy (RP), which entails complete removal of the prostate from the patient [10]. As with other forms of cancer resection surgery, the remission rate is mostly determined by the degree of cancer resection [11–13]. As a common practice, an additional section of tissue, the safety margin, will be removed around the anticipated malign area to remove cancer that may have spread beyond the original tumor scope [14]. However, certain cancer types surrounded by critical structures, such as brain or pancreas, require more conservative margins [15]. As a consequence, co-registration with imaging methods can be used during surgery to precisely target neoplastic tissue [16]. In a general sense, margin size varies with many parameters including surgery type, pre-surgery diagnostic and post-surgery quality of life. [17].

For PCa, the tumor is usually undetectable by standard imaging methods, forbidding the use of co-registration [18]. The standard of care procedures, such as trans-rectal ultrasound guided biopsies and PSA level testing, suffer from low sensitivity and specificity and give limited spatial information, making it difficult to pose an accurate diagnostic regarding the location and extent of the tumor [19, 20]. Close to the prostate are important genitourinary structures, such as the bladder and microscopic nerves, that impact continence and sexual function. To lower risks of damage to these structures, and thus increase post-procedure patient satisfaction, smaller surgical margins will often be favored for RP [21, 22]. However, if cancer is left un-resected at the margins due to cancer spread beyond the prostatic capsule, resulting in a positive margin, the patient requires additional treatment and may undergo a deteriorated prognosis [23, 24]. Consequently, having complete cancer resection while allowing the least amount of damage to the surrounding tissues can be a challenging task. Due to the shortcomings of current diagnostic tools for PCa, there is a crucial need for a tool allowing the rapid characterization of prostatic tissue. A system that differentiates prostate tissues, for example healthy *vs* cancerous or prostatic *vs* extra-prostatic, would ensure targeted resection of cancer and complete removal of the prostate without impact on other genitourinary structures during RP, thus reducing risks of recurrence and impacts on patient quality-of-life.

As such, several imaging techniques, such as optical coherence tomography [25], Raman spectroscopy [26], diffuse reflectance spectroscopy [27] as well as exogenous [28] and endogenous fluorescence [29], have been applied to prostatic tissue differentiation. The application of these techniques on the prostate so far has been limited to point probes offering at most millimeter size Field of View (FOV), which can limit clinical use. Optical coherence tomography enhances the contrast between tissues of distinct structures and refractive indices. Raman spectroscopy is based on the emission of energy specific to certain chemical bonds to identify tissue molecular content. Diffuse reflectance is the analysis of the white-light reflectance signal based on the tissue's properties of absorption and elastic scattering. Exogenous fluorescence relies on an external contrast agent with preferential accumulation in cancerous tissue to identify tumors.

Endogenous fluorescence was applied with success to multiple pathologies [1]. It exploits the intrinsic fluorescence of molecules in the tissue, which under proper excitation emit light with a specific spectrum. Therefore, endogenous fluorescence gives access to specific information on molecular content without the need to inject external agents [30]. It has found more widespread application in wide-field systems than other imaging techniques [3, 31]. A caveat of the imaging method is that fluorescence emission competes with other processes like absorption and elastic scattering, which vary locally in tissue. This means the detected fluorescence is not directly a quantitative representation of the sample's molecular content [2].

By using a multimodal approach combining fluorescence and diffuse reflectance it is possible to correct the effects of absorption and elastic scattering to obtain quantitative fluorescence results [32]. This quantified fluorescence gives access to molecular information and can be used as a biomarker for tissue identification. These corrections were initially limited to point probe geometries due to the complexity of modelling diffuse reflectance for wide-field geometries [33]. However, a recently developed imaging process called Spatial Frequency Domain Imaging (SFDI) based on structured illumination allows the reconstruction of absorption and elastic scattering properties in wide-field geometries [34]. SFDI has seen rapid improvement and a variety of applications, including breast cancer detection [35]. It has also been commercialized by the company *Modulated Imaging*. With the use of SFDI-derived properties, fluorescence could be quantified to reflect molecular content even in wide-field geometries. This expanded the applications and clinical relevance of the multimodal fluorescence and diffuse reflectance approach [6].

Although the current application of the SFDI fluorescence correction models has been limited to external agents, this project's objective is to push the technique to a novel usage in wide-field endogenous fluorescence. The system would provide quantitative molecular based

information that may be used to identify and differentiate tissues during radical prostatectomy procedures, thus reducing risks of damage to surrounding structures while maximizing cancer resection.

1.2 Thesis organisation

Including this introductory chapter, the thesis is divided into seven chapters. In the second chapter, a short review of the theoretical background on quantitative fluorescence imaging is presented. Specifically, a section on the SFDI technique with some insights into the concept of structured light transport and imaging is provided. Then, two sections on the theory of fluorescence and photo-luminescence, as well as the available approaches towards fluorescence quantification are detailed. The third chapter presents the proposed system, its relevance and novelty in the current state of the art, as well as the various hypotheses and objectives tackled in the project. The fourth chapter presents the work accomplished on the project in the form of an article detailing the imaging system, the validation of all its modalities and the initial results and observations on prostates. In the fifth chapter, additional results related to fluorescence quantification and cancerous prostate tissue differentiation are shown. The sixth chapter details the optical design specifications, acquisition and calibration processes and their optimizations. It also provides context to current system limitations as well as considerations for the *in vivo* transition of the system. The seventh chapter concludes the thesis by summarizing the work done throughout the master's degree while also touching upon possible improvements and future work left for the system.

CHAPTER 2 LITERATURE REVIEW

To facilitate the understanding of the project and its results, some necessary theoretical concepts are presented in this chapter. Firstly, details regarding SFDI are given, as well as more advanced processing details and corrections applied to the technique. Secondly, the basics of fluorescence are discussed, with a focus on endogenous fluorescence and its current usage. Lastly, the quantification techniques for distinguishing intrinsic fluorescence from tissue absorption and scattering, and obtaining filtered spectra corresponding to the molecular content of the tissue are presented along with supplementary context on the radical prostatectomy procedure.

2.1 Spatial Frequency Domain Imaging

2.1.1 Light Transport in Tissue

There are three main interactions of light with biological tissue: reflection, scattering and absorption [5, 36]. An example of these interactions is shown in figure 2.1. Reflection occurs when light bounces off directly from a flat surface; this is mostly governed by the reflectivity of the tissue and does not give much indication regarding the tissue properties, other than the refractive index. It is of little interest for tissue characterization.

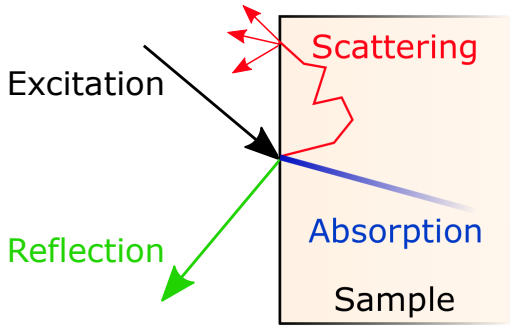

Figure 2.1 Main light-tissue interaction mechanisms.

Scattering is experienced by the light that penetrates the sample. It is related to the refractive index n, scattering coefficient μ_s and anisotropy g, the latter which can be combined into the reduced scattering coefficient $\mu_s' = (1-g)\mu_s$ [37]. In a heterogeneous biological sample, it is caused by the distribution of particles in the medium; in this case cells, organelles, membranes, etc., which in turn lead to local changes in the refractive index. In purely

scattering media, this causes the light to be scattered in various directions inside the tissue until its path emerges from the surface. Furthermore, since it depends mostly on tissue structure, the reduced scattering coefficient μ_s' can be estimated to be a power law

$$\mu_s' = A\left(\frac{\lambda}{\lambda_{ref}}\right)^B, \tag{2.1}$$

dependent on current wavelength λ. Coefficient A corresponds to μ_s' at a reference wavelength λ_{ref} and B is the *scattering power* coefficient characterizing the wavelength dependence of μ_s'. Although this mathematical model has been used in numerous studies, it is important to note that it is not recommended to extrapolate beyond the wavelength range acquired [38]. The scattering phenomenon is either elastic, where the emitted photon has the same energy as the incident photon, or inelastic, where the emitted photon is of lower energy. Rayleigh scattering and Raman scattering are two examples of elastic and inelastic scattering, respectively. In Raman scattering, light loses energy by interacting with vibrational modes of the molecules inside the tissue. This can be exploited to identify the sample since these interactions produce a unique chemical signature.

The light that penetrates the tissue also experiences absorption. The effect is mostly governed by the absorption coefficient μ_a and, unlike scattering, it is the tissue composition that mostly affects absorption. Certain molecules in the tissue, designated as absorbers or chromophores, have electronic transitions that correspond to the energy of light at certain wavelengths; this allows them to be excited by light in these spectral bands. The absorbed energy can be re-emitted as heat or through various photochemical reactions, such as fluorescence, which will be discussed in section 2.2. Consequently, the absorption coefficient can only be modelled if the specific concentration of every tissue component is known. Some examples of the spectra of main absorbers in biological tissue are shown in figure 2.2.

Most biomedical imaging devices make measurements in the near-infrared range of 600-1300 nm, known as the therapeutic window [39]. This range is where hemoglobin and deoxyhemoglobin, the most common absorbers in human tissue, have minimal absorption. Avoiding the sample's main chromophore's absorption peaks leads to increased Signal to Noise Ratio (SNR) and penetration depths; making it an important factor in system design.

2.1.2 Diffuse Reflectance

The scattering, anisotropy, and absorption properties can be used to characterize the tissue structure and its molecular contents. By exciting the tissue with white light and measuring response at multiple wavelengths, without specular reflection, a spectrum of diffuse reflectance

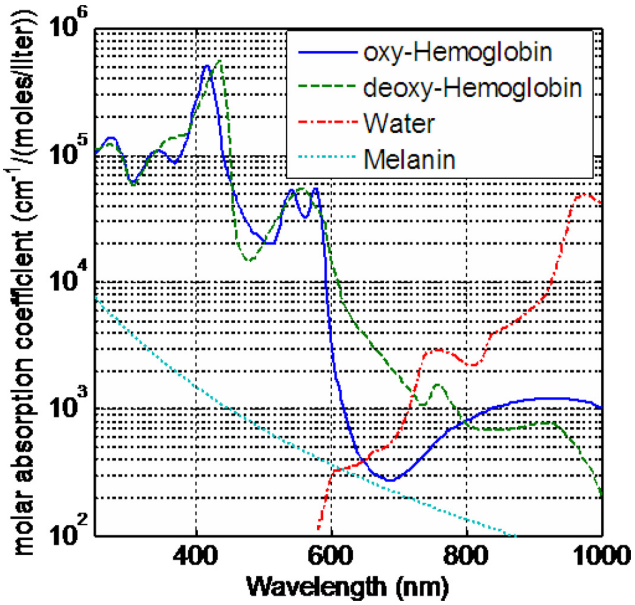

Figure 2.2 Absorption spectra of the main chromophores in human tissue. [5]

is obtained. This measurement reflects several scattering and absorption events occurring at multiple depths in the tissue. Obtaining the absorption and scattering coefficients from the diffuse reflectance spectrum requires modelling tissue reflectance, accounting for multiple parameters including sample geometry, source and detector types and positions [40]. Using various mathematical approaches, several models for determining the optical properties of the tissue from the measured spectra were reported in the literature [41–44]. Yet, none of these methods can be used to model optical properties in macroscopic diffusive reflectance measurements, which limits the extraction of optical properties to point probe geometries ($<$mm^2). Nonetheless, the computed optical properties can be used to extract, most notably, μ_a and μ_s', hemoglobin and deoxyhemoglobin concentrations, as well as scatterer size and density [45, 46].

These tissue properties can be used in several applications to differentiate tissue types [47]. During prostate monitoring for photodynamic therapy, the blood oxygen saturation was observed to maximize the impact of the treatment [48]. In another case, absorption and scattering of the tissue were used to determine scatterer size and discriminate between cancerous and healthy prostate tissue [49]. There has also been a study regarding elastic-scattering guided biopsies for prostate cancer diagnosis [27].

2.1.3 Structured Imaging Theory

In order to overcome the view field limitations of standard diffuse reflectance spectroscopy, a new technique was developed using spatially structured imaging [34]. Implemented by Cuccia *et al.*, the basis of SFDI was the use of a Digital Light Processing (DLP) device to structure illuminating light in sinusoidal patterns that are projected at various spatial frequencies and phases onto the sample. An example of this procedure is shown in figure 2.3. By solving the standard diffusion equation in a homogeneous medium, it was demonstrated that the frequency of the sinusoidal wave affects the penetration depth of light in the tissue. The tissue may be thought of as a low-pass filter, which allows light with lower spatial frequencies to penetrate and be absorbed into deeper layers, and scatters light with higher spatial frequencies at shallower depths.

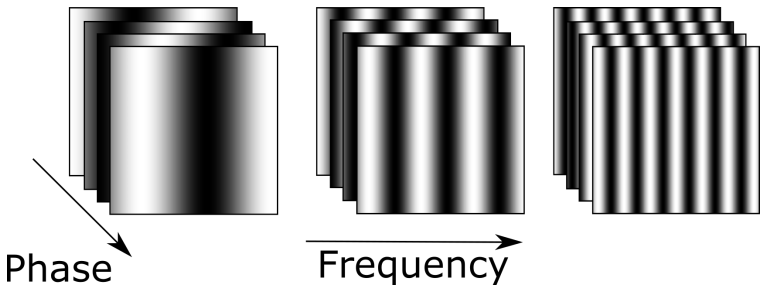

Figure 2.3 Example of structured projection patterns for spatial frequency domain imaging showing three frequencies with four phases each.

In other words, the fluence rate of light propagation within the tissue is mainly dependent on the illumination spatial frequency. This fluence rate could then be used in previously developed diffusion models to find reflectance values unique to a set of a spatial frequency, and absorption and scattering coefficients [41]. Most crucially, all modeling was done with a pure 1-D sinusoidal illumination pattern, generalizable to any sinusoidal pattern in horizontal or vertical directions, and independently of source/detector distances. This flexibility regarding the projected source allowed to model diffuse reflectance in wide-field geometries (>10 cm^2) and thus extract quantitative information on the tissue in macroscopic FOVs.

2.1.4 Structured Imaging Processing

Although the specific mathematical development related to diffusion theory and the fluence rate is left out, the calibration and data processing behind SFDI is explained in this section; with additional mathematical detail found in the Cuccia *et al.* paper establishing the SFDI

technique [34]. The illuminating light S is modulated according to

$$S = \frac{S_0}{2}[1 + M_0 cos(2\pi f_x x + \alpha)], \tag{2.2}$$

where S_0 is the amplitude of the light, f_x is the spatial frequency along the horizontal axis, α is the phase, and M_0 is a constant called modulation depth. All variables are presented in the case of a 1-D sinusoid illumination pattern. As shown in Eq. 2.2, the illumination pattern features both planar and spatially modulated elements, since it is impossible to illuminate negative intensities on the sample. Thus, a measurement of this pattern on tissue gives both a constant base associated with planar illumination (I_{DC}) as well as a signal related to spatial modulation that varies from frequency to frequency (I_{AC}). Measured intensity I can be represented by

$$\begin{aligned} I &= I_{DC} + I_{AC} \\ I_{DC} &= M_{DC}(x) cos(\alpha) \\ I_{AC} &= M_{AC}(x, f_x) cos(2\pi f_x x + \alpha), \end{aligned} \tag{2.3}$$

where M_{DC} is the DC amplitude and M_{AC} is the AC amplitude of the reflected photon density standing wave; with M_{AC} being of interest to distinguish local features in the tissue. The demodulation of the DC and AC terms is done with at least three phase measurements per frequency, noted as I_1, I_2 and I_3. These phases are equally distributed in the 2π radians circle, which allows the elimination of the DC term as follows

$$M_{DC} = \frac{1}{3}\left[I_1(x_i) + I_2(x_i) + I_3(x_i)\right], \tag{2.4}$$

$$M_{AC}\left(x_i, f_x\right) = \frac{2^{1/2}}{3}\left\{\left[I_1(x_i) - I_2(x_i)\right]^2 + \left[I_2(x_i) - I_3(x_i)\right]^2 + \left[I_3(x_i) - I_1(x_i)\right]^2\right\}^{1/2}. \tag{2.5}$$

Note that this can also be achieved with any higher number of phases equally distributed in 2π. In the frequency domain, the AC measurement can be represented as

$$M_{AC}\left(x_i, f_x\right) = I_0 MTF_{system}\left(x_i, f_x\right) R_d\left(x_i, f_x\right), \tag{2.6}$$

where I_0 is the source intensity and R_d is the diffuse reflectance of the sample. The system's response (MTF_{system}) can be eliminated with a reference measurement with known optical properties. For this purpose, it is a common practice to use an optical phantom; a mea-

surement platform made with materials of known absorption and/or scattering properties. There are many types of optical phantoms, such as intralipid based liquid phantoms, solid phantoms based on PDMS or gelatin, and biological tissue-based phantoms [50]. Choosing a proper reference phantom with optical properties similar to those of the imaged sample leads to improved accuracy in SFDI reconstruction [34]. Since the reference measurement $M_{AC,ref}$ also depends on the system, it can be used to divide the sample measurement

$$R_d\left(x_i, f_x\right) = \frac{M_{AC}\left(x_i, f_x\right)}{M_{AC,ref}\left(x_i, f_x\right)} R_{d,ref}\left(f_x\right), \tag{2.7}$$

thus eliminating MTF_{system} and I_0. The only unknowns left in this equation are both diffuse reflectance values. The simplest approach for finding the reflectance value for the reference phantom $R_{d,ref}$ is to apply the diffusion approximation to the radiative transfer equation. However, since in most of the common biological tissues the scattering is not so dominant, this approximation does not lead to reliable values [51]. Consequently, for biomedical imaging, it is more common to use transport-based Monte-Carlo (MC) simulations to obtain $R_{d,ref}$, which will not be covered in detail here. It should be noted that those MC simulations usually work best for semi-infinite homogeneous media, and their simulated results for finite or heterogeneous media may suffer substantial inaccuracy.

Using the $R_{d,ref}$ determined via MC simulation in Eq. 2.7 allows to solve for R_d. The same MC code can then be used inversely to compute the optical properties responsible from the measured reflectance. An efficient approach to this inverse problem is to create a look-up table by generating reflectance values for a large variety of optical properties at each of the measured spatial frequencies. Each value is assigned to a spot in the table, creating a quick method to calculate the error of the measured value against the simulated value for each optical property set at each frequency. By using a least-squares optimization method, the absorption and scattering of the sample are obtained. This whole process is repeated for every pixel of the image to create a wide-field map. Note that at least two frequencies are needed for this method to obtain precise results. A visualization of the method for a case with two frequencies is shown in figure 2.4, where the error to minimize is the distance to the intersection point. It can be observed that reconstruction is less precise for lower albedo values as the intersection points become increasingly condensed.

It is possible to improve the results given by such tables by optimizing the choice of spatial frequencies to the sample's expected range of optical properties [52]. The more the lines are orthogonal to each other, the lesser is the coupling between absorption and scattering that may lead to errors in the reconstruction. This problem of coupling is especially pronounced

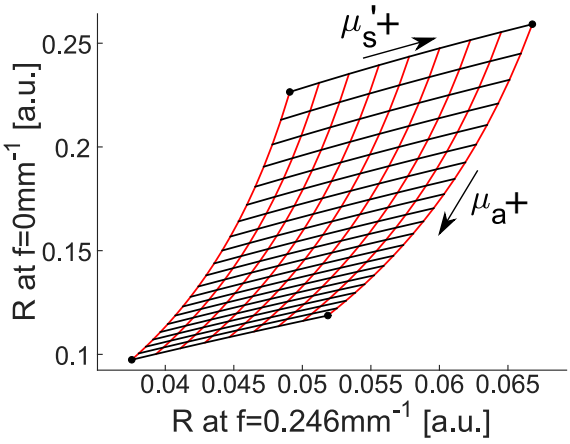

Figure 2.4 Visualization of two-frequency spatial frequency domain imaging lookup table for reconstructing optical properties from reflectance measurements. Each intersection point represent a spot in the table; a set of absorption and scattering properties.

for samples with higher absorption and lower scattering. Another method for improving the accuracy of the reconstruction is to measure at additional spatial frequencies, which leads to a larger number of references in the lookup table but increases acquisition time.

2.1.5 Structured Imaging Enabled Profilometry

In SFDI diffuse reflectance modelisation, whether the diffusion approximation to the radiative transfer equation or Monte-Carlo simulations are used, it is always assumed that the sample geometry is flat, as it is unrealistic to accurately model the specific geometry of each measured sample. However, in practical applications, the samples come with uneven surfaces, which imposes a considerable source of error in the optical property reconstruction [53].

To address this problem, the surface of the sample needs to be reconstructed. A convenient method for surface reconstruction is the phase-shifting profilometry technique [54]. This method is based on the projection of sinusoidal patterns at multiple phases on the sample, as it is done in SFDI. Due to the source-detector angular difference, patterns are deformed locally at detection by the tissue geometrical features. The additional phase present in the distorted patterns can be calculated using each of the phase-shifted patterns. When compiling all phase measurements, fringe patterns of different curvatures and widths appear on these geometrical features. The obtained phase is initially comprised between 0 and 2 π, so a phase unwrapping is performed at each point on the sum of phases, giving a full profile of phase variation on the sample.

The exact application of the technique to SFDI was developed by Gioux *et al.* [55]. A relation between the measured phase variation and height variation is computed by making calibration measurements on the reference sample in which height and surface angle are varied in the expected range of the sample geometry. These measurements are also used to build a table of $M_{AC,ref}$ *vs* height. By using the phase *vs* height variation relation, the tissue sample's height is reconstructed. Then, the $M_{AC,ref}$ *vs* height table is used to create a $M_{AC,ref,corrected}$, which is $M_{AC,ref}$ adjusted pixel by pixel to correct for the sample's height variations. The correction is applied to $M_{AC,ref}$ rather than M_{AC} directly since the M_{AC} *vs* height relation is unknown. For angle calibration, a model-based approach is used by multiplying $M_{AC,ref,corrected}$ by the cosine of the angle between the normal of the surface and the detection axis. The division of M_{AC} by $M_{AC,ref,corrected}$ is done as shown in Eq.2.7 and allows the extraction of a sample height/system influence corrected R_d, and thus μ_a and μ'_s.

This profilometry technique integrates to the SFDI workflow smoothly, allowing correction for the height variations of the sample and reducing reconstruction errors, especially for the absorption coefficient. The phase-shifting algorithm does not require any additional measurements to regular SFDI, making it without impact on acquisition time. The calibration measurements, however, must be done for every specific hardware configuration, including changes in polarisation.

2.1.6 Advances in spatial frequency domain imaging

There have been other developments than profilometry-based geometrical corrections regarding the caveats of SFDI. One of them is the reduction of the error on high absorption or low albedo tissue. Studies have shown that using a higher absorption reference measurement can improve the results, but this does not solve the coupling problem with the lookup table [56]. Others have used empirical lookup tables based on high absorption phantom measurements to improve results [57]. A semi-empirical model has also been introduced for measurements in the sub-diffusive domain and was applied in combination with the standard diffusion model to obtain accurate absorption and scattering values on tissue [58]. The model exploits the fact that absorption has minimal influence on high spatial frequencies to use an equation for diffuse reflectance modelling independent of absorption.

Additionally, the transport model was adapted to better compensate for border effects and achieve absorption-based tomographic imaging. This improved model was notably applied to brain tumors [59–61]. Finally, by projecting a single frequency and using alternative processing methods for the image in the Fourier domain, real-time SFDI was achieved while retaining similar accuracy on the reconstruction of optical properties [62]. By projecting

multiple patterns at once, profilometry was also implemented to this Single Snapshot imaging of Optical Properties (SSOP) technique [63].

2.2 Fluorescence

2.2.1 Fluorescence Properties

Luminescence is the emission of light not induced by heat. Photo-luminescence is a subset of these phenomena where the emission is caused by the absorption of a photon ($\hbar\omega_0$). Photo-luminescence includes fluorescence ($\hbar\omega_F$), phosphorescence ($\hbar\omega_P$) and Raman emission ($\hbar\omega_{R-S}, \hbar\omega_{R-AS}$). Figure 2.5 illustrates these various photo-luminescent phenomena. As was discussed in section 2.1.1, Raman emission is the product of the photon inelastic scattering with a molecule. Fluorescence and phosphorescence both result from the excitation of an electron by absorption; with fluorescence emitted very quickly, usually in the nanoseconds, while phosphorescence is emitted orders of magnitude slower, *i.e.* the microseconds [64]. This is because phosphorescence is associated with forbidden electronic transitions.

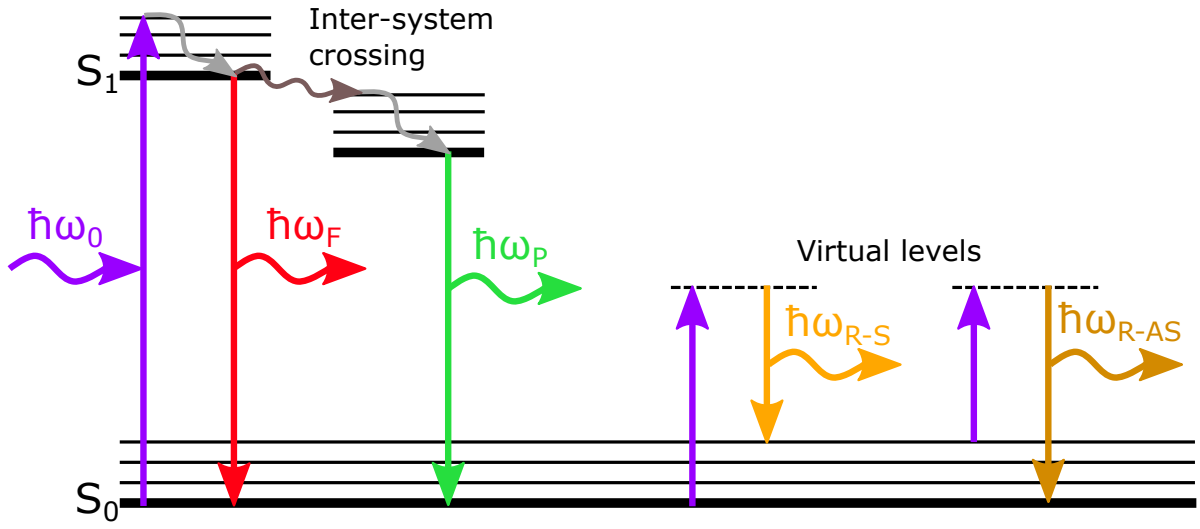

Figure 2.5 Jablonski diagram of photo-luminescent effects.

As a whole, fluorescence found more use in the biomedical domain [30]. Fluorescent molecules, also referred to as fluorophores, have many properties. Fluorescence lifetime is a measure of how quickly the emission fades once excitation is stopped; this is highly dependent on the electronic transition speed which itself can be influenced by a variety of environmental factors [1,65]. Quantum yield quantifies the fraction of emitted photons per excitation photons. Each fluorophore also has an emission spectrum as well as an excitation spectrum; these dictate

the efficiency of excitation depending on wavelength, and the emission wavelengths and their relative intensities, respectively. Note that the emission spectrum is not dependent on the wavelength of excitation. The Stokes shift is defined as the wavelength difference between the absorption and emission peaks. Finally, photobleaching is the process in which the emission of a fluorophore lowers in intensity after successive excitation periods, due to progressive chemical bonds breakage under light excitation.

2.2.2 Fluorescence Types

There are two types of fluorescence in the context of biomedical imaging: exogenous fluorescence and endogenous fluorescence. Exogenous fluorescence is fluorescence achieved by adding an external agent to the sample. This fluorescent agent can be used directly to tag specific structures in a sample or indirectly, as some chemical compounds lead to an accumulation of a fluorophore inside certain tissue types [66]. For this fluorescence type, the fluorophores are present in high quantities in the structures of interest and also have known excitation and emission peaks, that can be chosen to minimize competition with other optical events such as tissue absorption and scattering processes. However, finding a fluorophore that accumulates only in the structures of interest can be challenging as, even if the signal is strong, the precision of the structure identification depends entirely on the specificity of the accumulation. The process of getting approval for the common use of an external agent on a human patient is also highly complex and costly, which adds roadblocks to clinical implementation of the technique [67].

Endogenous fluorescence, or autofluorescence, is the fluorescence emitted by molecules naturally present in biological tissue. Table 2.1 shows a list of fluorophores commonly found in human tissue. Most of the excitation peaks and several of the emission peaks of these fluorophores are in the UV region, which is not ideal due to typically high tissue absorption in this wavelength range. Furthermore, the concentration of endogenous fluorophores is very low in human tissue. Due to these two reasons, the detected intensity of endogenous fluorescence is usually a few orders of magnitude weaker than that of the exogenous fluorescence [68]. Moreover, since multiple endogenous fluorophores are excited at once, the resulting emission spectrum is more complex, often requiring additional processing like spectral unmixing. Despite these difficulties, endogenous fluorescence provides molecular information on the tissue, which can be used as surrogate for the cellular function or to identify tissue types [4, 69, 70].

Table 2.1 Excitation and emission peaks of some fluorophores found in human tissue. [1–4]

Fluorophore	Excitation peak [nm]	Emission peak [nm]
Amino acids		
-Tryptophan	280	350
-Tyrosine	275	300
-Phenylalanine	260	280
Structural proteins		
-Collagen	325,360	400,405
-Elastin	300-340	420-460
-Phenylalanine	290,295	340,400
Enzymes/coenzymes		
-FAD/flavins	450	535
-NADH	290,351	440,460
-NADPH	336	464
Lipids		
-Phospholipids	436	540,560
-Lipofuscin	340-395	540,430-460
-Ceroid	340-395	430-460,540
Porphyrins	400-450	630,690

2.2.3 Fluorescence Imaging Techniques

There are a high number of imaging techniques using fluorescence in biomedical imaging, as every fluorescence property can be measured and exploited. Fluorescence Lifetime Imaging Microscopy (FLIM) computes fluorescence lifetime with precise measurements of the fluorescence emission decay curve; data that can then be used to characterize tissue [71]. Fluorescence Resonance Energy Transfer (FRET) uses the quantum efficiency of a non-radiative energy transfer between two fluorophores which is strongly dependent on the donor-acceptor distance, thus notably allowing the observation of several protein-protein interactions [72]. Fluorescence Recovery After Photobleaching (FRAP) exploits the delay for fluorescence recovery after periods of photobleaching to obtain a measure of molecular mobility in tissue [73]. Fluorescence Imaging (FI) analyses the emission intensity spectrum for a certain excitation wavelength to quantify sample molecular content [74].

A specific point of interest for fluorescence is the translation of these techniques to wide-field imaging, as many fluorescence spectroscopy methods are based on microscopes or fiber-optic probes and offer view fields of at most a few mm^2 [75,76]. For the prostate application, wide-field would represent a macroscopic FOV >10 cm^2 and the only technique to be applied to the macroscopic scale is FI. Endogenous fluorescence imaging endoscopes have been used to differentiate dysplasia, neoplasia and *in vivo* brain tumors [3,31,77]. In the case of exogenous

fluorescence imaging, the use of 5-Aminolevulinic Acid (5-ALA) to cause a specific accumulation of Protoporphyrin IX (PpIX) in cancerous tissue has found to multiple applications, notably in phototherapy and photodiagnosis [78]. 5-ALA has become common in surgical use in the United States since it has been approved by the Food and Drug Administration (FDA), although Canada has not yet allowed the use of the substance [79]. One notable usage of 5-ALA was with macroscopic imaging systems to guide the resection of brain tumors [80]. Nevertheless, there is some evidence that PpIX has limited specificity and accumulates in other tissue as well, which can lead to false positives and unnecessary resections [81, 82].

FI has found a few applications in prostate cancer detection and treatment. The use of exogenous fluorophores is limited, but a group has explored the use of 5-ALA to cause a specific accumulation of PpIX in cancerous prostate regions [28]. For endogenous fluorescence, Autofluorescence Lifetime Spectroscopy (AFLS) in combination with reflectance spectroscopy was used to achieve good classification results on prostate cancer [83]. Stokes Shift Spectroscopy (S3) has also shown reliable results in differentiating the cancerous prostate tissue from healthy tissue [29, 84]. However, there is no reported article considering the application of wide-field fluorescence set-ups for prostate cancer detection.

2.3 Fluorescence Quantification

2.3.1 Definition of Fluorescence Quantification

In biological media, there are multiple light interaction phenomena other than fluorescence, as presented in section 2.1.1. Consequently, fluorescence competes with processes like absorption and elastic scattering, which not only influences the fraction of light exciting fluorophores but also the fraction of fluorescence emission detected at the tissue surface, as illustrated in figure 2.6. This lowers signal and disrupts the relation between fluorescence intensity and molecular content, since regions with homogenous fluorophore concentration but heterogenous absorption and/or scattering properties yield different emission intensities. Since absorption and scattering often varies locally on a biological sample, it is challenging to obtain quantitative fluorescence information for tissue analysis [2].

Consequently, mathematical models were developed by several groups to account for the absorption/scattering properties and obtain a quantitative signal; quantified fluorescence [32]. This also led to the creation of specially adapted probes that sample geometries in which these properties are negligible [85]. Additionally, Monte Carlo methods were implemented for more complex geometries or time-resolved measurements [86].

These analytical methods are unsuited to wide-field geometries, where the effects become too

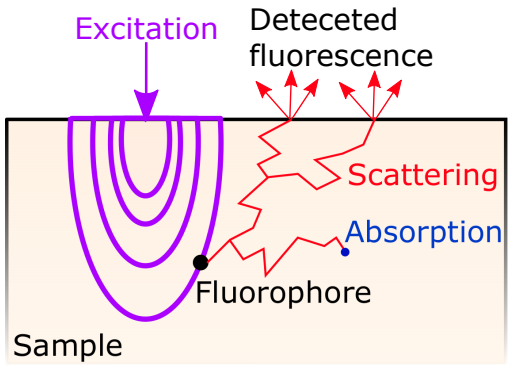

Figure 2.6 Process of fluorescence excitation and emission with possible interactions in tissue.

complex to be modeled accurately. This initially led to a different, more empirical approach for absorption/scattering corrections in wide-field systems [33]. However, the development of SFDI allowed the implementation of fluorescence quantification models with optical properties in wide-field set-ups. Indeed, fluorescence quantification is the linking factor between the two main imaging techniques presented in this literature review; SFDI and FI.

2.3.2 Reflectance Ratio Fluorescence Corrections

The idea of fluorescence quantification stems from the use of combined datasets from fluorescence and diffuse reflectance for cancer detection [77]. This led to the investigation of normalizing these datasets with each other, which yielded improved results over the non-normalized datasets [87, 88]. The intuition for this was based on the fact that intrinsic fluorescence (QF), once divided by reflectance (R_d), is linearly proportional to fluorophore concentration ($C_{fluorophore}$)

$$\begin{aligned} F_{raw} &= KC_{fluorophore}R_d \\ \frac{F_{raw}}{R_d} &\propto C_{fluorophore}, \end{aligned} \tag{2.8}$$

where K is a constant number depending on various factors such as fluorophore quantum yield and instrument response [88]. This ratio-based correction marks a clear departure from earlier point-probe approaches due to the empirical nature of the correction. Thanks to the relative simplicity of implementation and rapidity of execution, the reflectance division correction has found widespread usage in wide-field systems, as far as the implementation in real-time imaging [89]. Although, once again, it is important to mention the technique is not

rigorous from a theoretical standpoint

Building upon this technique, by restricting the division to areas of interest of the spectrum, Valdés *et al.* developed an algorithm that divides the measured fluorescence (F_{raw}) by reflectance integrated over the excitation wavelengths ($R_{d,x}$) and over the emission wavelengths ($R_{d,m}$) along with a calibration factor (α) to obtain quantified fluorescence (QF) [90]

$$QF = \frac{F_{raw}}{R_{d,x}\left(R_{d,m}\right)^{\alpha}}. \tag{2.9}$$

This semi-empirical model assumes that most of the absorption occurs at the excitation wavelength and that the emission region is dominated by scattering. The α coefficient is determined by making fluorescence and reflectance measurements on optical phantoms with various optical properties and a single fluorophore concentration. Then, multiple α values are applied to correct the measurements. The coefficient minimizing the Standard Deviation (STD) between the fluorescence intensity values of the different phantoms is selected for the correction. Another approach is to use multiple phantom sets with increasing fluorophore concentrations. In this case, a linear plot is used and the R^2 of a linear fit serves as a measure for both the STD within same-concentration phantoms and the accurate scaling of corrected intensity between concentrations.

This method was demonstrated on a point probe [91]. It was also integrated with a wide-field neurosurgery guidance system based on PpIX fluorescence quantification, leading to more accurate tumor identification [92]. The major disadvantage of this technique is that if the Stokes shift of the fluorophore is too small, the two assumptions cannot be satisfied. This also applies to endogenous fluorescence since there is a continuous emission spectrum that can be close to the excitation wavelength. Furthermore, using an exponential fitting method on phantoms can lead to a result that is too specific to this calibration, and thus less applicable to biological tissue. Moreover, the exponential fitting may increase the noise level in the final result.

2.3.3 Optical Properties Fluorescence Corrections

With the advent of SFDI-enabled wide-field reconstruction of absorption and scattering, some model-based fluorescence correction techniques were now translatable to the macroscopic scale. A first subset of methods were developed based on a photon migration model by Wu *et al.*, which provided a relationship between fluorescence and diffuse reflectance in turbid media while introducing corrections with optical properties [44]. This model was then modified by Zhang *et al.* to encompass a wider range of wavelengths, from 370 to 700 nm, which included

the high absorption region of hemoglobin and was, therefore, more appropriate for Ultra-Violet (UV) excitation in tissue [93]. The final transition into wide-field was made by Yang *et al.*, which demonstrated fluorescence quantification with the model using SFDI-derived absorption (μ_a) and scattering (μ_s') coefficients [6]. They obtained corrected fluorescence (QF) using

$$QF(\lambda) = \frac{F_{raw}(\lambda)}{\frac{1}{\mu_{s,x}l}\left(\frac{R_{0,x}R_{0,m}}{\epsilon_x\epsilon_m}\right)^{1/2}\frac{R_x}{R_{0,x}}\left(\frac{R_m}{R_{0,m}}+\epsilon_m\right)}, \tag{2.10}$$

$$\epsilon = exp\left(S(1-g)\right) - 1, \tag{2.11}$$

where g is sample anisotropy, found in literature, and both l and S are empirical parameters fit to the system. F_{raw} is the fluorescence measurement, R is the diffuse reflectance measurement, while the R_0 values are reflectance evaluated without absorption. The x and m subscripts denote whether the variable is evaluated at the excitation wavelength or emission wavelength, respectively. Firstly, there are two empirical parameters that require fitting and can be specific to an individual source-detector configuration. Secondly, the equation also uses the reflectance without absorption. To obtain this value, it is necessary to find ($\mu_a = \text{x}$, $\mu_s' = \text{y}$) on the pixel and then reference the SFDI lookup table to find its reflectance value corresponding to ($\mu_a = 0$, $\mu_s' = \text{y}$). This is not only more computationally expensive, but the lookup table is not a perfect representation of reality, thereby increasing the measurement's incertitude [34]. Nevertheless, the method was used by Yang *et al.* to reduce the variation of fluorescence intensity to a higher degree than simple reflectance ratio in tissue-based phantoms with fluorescein. Since the paper did not provide metrics to quantify the results, the main results graph is shown in figure 2.7. There were no further reported studies using this technique in biological samples or surgical context.

Another way of approaching the problem was outlined by Gardner *et al.*, where they used empirical factors dependent on diffuse reflectance C, k, as well as effective penetration depth δ and absorption/scattering properties (μ_a, μ_s') [43]. Quantified fluorescence (QF) was modeled from the fluorescence measurement (F_{raw}) as

$$QF = F_{raw}\left\{\frac{C_{1,x}C_{3,m}}{k_{1,x}/\delta_x + k_{3,m}/\delta_m} - \frac{C_{2,x}C_{3,m}}{k_{2,x}/\delta_x + k_{3,m}/\delta_m}\right\}^{-1}, \tag{2.12}$$

$$\delta(\lambda) = \left\{3\mu_a\left[\mu_a + \mu_s(1-g)\right]\right\}^{-1/2}. \tag{2.13}$$

Once again, the x and m subscripts are used to denote if the value is at the excitation or emission wavelength. Gardner *et al.* specified their coefficients for two cases of sample/air

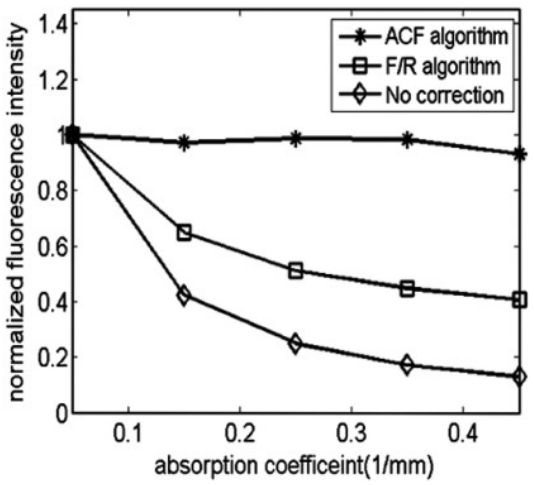

Figure 2.7 Normalized fluorescence intensity of a series of phantom with same fluorophore concentration but increasing absorption coefficient. Results are presented without correction, with a simple ratio correction and with the ACF correction algorithm of eq.2.10. [6]

refractive indices ratios, but it was chosen to show here only the case where the ratio is 1.38 since it is more relevant to biological tissue. The coefficients were computed with the diffuse reflectance measurement R_d and defined as

$$\begin{aligned} C_1 &= 3.09 + 5.44R_d - 2.12exp(-21.5R_d), \\ k_1 &= 1 - (1 - 1/\sqrt{3})exp(-20.1R_d), \\ C_2 &= 2.09 - 1.47R_d - 2.12exp(-21.5R_d), \\ k_2 &= 1.63exp(3.40R_d), \\ C_3 &= 0.28 + 0.78R_d - 0.14exp(-10.7R_d), \\ k_3 &= 1 - 0.31exp(-6.12R_d). \end{aligned} \tag{2.14}$$

The usage of these six empirical parameters calculated for a specific refractive index is a disadvantage of the technique, as they are bound to be inaccurate in biological tissue which does not have the specified ratio of 1.38. Moreover, the refractive index varies with wavelength and locally in tissue, which would introduce errors. The method also requires the optical properties of the tissue at the emission wavelength. While less detrimental to exogenous fluorescence, SFDI measurements must be taken at every detected wavelength for endogenous fluorescence, which drastically increases acquisition time.

The model was applied in macroscopic quantification of PpIX for the detection of skin tumors

using SFDI and fluorescence measurements [94, 95]. Particularly relevant to this project was the development of a bi-modal endoscope for quantitative imaging of doxorubicin, a drug used in ovarian cancer treatment, employing this algorithm [96]. The study also implemented the SFDI profilometry algorithm mentioned in section 2.1.5 in their analysis. They achieved 15% error for the quantification of drug concentration in biological mice tissue. The error was explained by the use of an endoscope which lowered the accuracy of the reconstruction of optical properties.

The final fluorescence correction technique was developed by Kim *et al.*, initially in a fiber optics probe used for PpIX measurements [97]. They posed true intrinsic fluorescence (QF) as a product of fluorophore absorption (μ_{af}) and quantum yield (Q)

$$QF = \mu_{af,x} Q_{x,m} = \left(\frac{\mu_{a,x}}{1 - R_{t,x}}\right)\left(\frac{F_{raw}}{R_{d,m}}\right), \tag{2.15}$$

then provided expressions of theses parameters using tissue absorption and reduced scattering (μ_a,μ_s') as well as diffuse reflectance

$$\begin{aligned} R_{t,x} &= \frac{a_x'}{1 + 2\kappa(1 - a_x') + [1 + (2\kappa/3)\sqrt{3(1 - a_x')}]}, \\ a_x' &= \frac{\mu_{s,x}'}{\mu_{a,x}\mu_{s,x}'}, \\ \kappa &= \frac{1 + r_{id}}{1 - r_{id}}, \\ r_{id} &= -1.44\left(\frac{n_s}{n_e}\right)^{-2} + 0.71\left(\frac{n_s}{n_e}\right)^{-1} + 0.67 + 0.0636\frac{n_s}{n_e}. \end{aligned} \tag{2.16}$$

F_{raw} is the fluorescence measurement and R_d the diffuse reflectance measurement. Yet again, subscripts x and m denote use at excitation and emission, respectively. The modelled reflectance (R_t) is calculated with the reduced albedo (a') and the internal reflection parameter (κ). The albedo depends on μ_a, μ_s' and κ is determined by an empirical formulation (r_{id}), computed with the refractive indices of the sample (n_s) and of the exterior (n_e). The model assumes that fluorophore absorption is negligible compared to tissue absorption and that absorption at excitation is high. There is an empirical parameter in the equation, but it does not require fitting to a specific system and can be adapted for different refractive indices. However, the method does not account for local refraction index changes.

One study applied this quantification method to PpIX fluorescent liquid phantoms and tissue

phantoms with PpIX inclusions using a benchtop system and point probe [56]. They lowered relative STD from 107% to 15.4% and 10.1% with the imaging system and probe, respectively. A notable point of the study was that some of their optical phantoms had a very low albedo, showing that the correction method applies to biological tissue close to the UV region. Another group also implemented the correction method in real-time measurements of quantified PpIX fluorescence using SSOP [98]. With their wide-field system, they reduced the relative STD from 34.5% to 4.0%. Although there is no reported system implementing profilometry corrections to quantified fluorescence obtained with Eq. 2.15, this quantification method is the only one to be applied to real-time imaging and the most readily adaptable to different systems and samples.

2.3.4 Relevance in prostate cancer treatment

2.3.4.1 Surgical context

RP is the only curative surgical approach to PCa treatment and is a procedure performed in most patient's active treatments [99]. Multiple approaches are used for the surgery, which can be placed in two categories: open surgery and laparoscopy [100]. For open surgery, a larger opening is made directly leading to the organ, while for laparoscopy the instruments are inserted through small (Φ ~12.7 mm) openings in the patient's abdominal cavity. The development of laparoscopic robot-assisted procedures, which improve the freedom of movement compared to the traditional laparoscopic techniques, has increased the prevalence of this second approach compared to open surgery [101]. This is why this specific application was considered for the project.

Laparoscopy could be considered the more challenging approach in the scope of optical system development, since instrumentation needs to be more compact and flexible. However, exterior lighting has less impact in this surgery type. Other factors to consider for the surgical context are that, due to the location of the organ deep in the waist and the presence of other biological structures, the surgical cavity for RP is small in both surgery types [102], and the necessity to cut tissue for resection makes the presence of blood in the cavity likely [103].

The priorities of an imaging system used during RP would be to identify cancerous tissue to allow complete cancer resection and to differentiate critical extra-prostatic structures, such as nerves, to reduce the risks of damaging them. However, in the current surgical context, no image co-registration methods or tissue differentiation systems are used [18].

2.3.4.2 Imaging considerations

In research, as explained in the thesis introduction, several imaging techniques have been applied to prostate tissue characterization, but all have been limited to millimeter-sized FOVs. Reported works are for systems applied to malign *vs* benign *vs* hyperplasic tissue differentiation or to the detection of nerves surrounding the prostate tissue. No system has been found satisfying both needs identified by the surgical context. Considering the small size of the surgical cavity and limitations of laparoscopic approaches for RP, the use of two different imaging systems would likely necessitate swapping instruments. This would make co-registration of the results difficult and complicate the procedure. Moreover, the FOV size of reported works would require multiple measurements in the surgical area to guide resection.

Fluorescence quantification can be applied in macroscopic FOVs, which would cover the entire surgical cavity. The image could be used to simultaneously identify cancerous prostate tissue and characterize surrounding tissues, thus meeting both surgical needs. The technique can also compensate for the local levels of blood, corresponding to variations in μ_a, in the imaging field, which makes it particularly relevant for the *in vivo* context.

CHAPTER 3 PROJECT OBJECTIVES

Among the wide-field endogenous fluorescence imaging systems, there is none that provides quantitative information about the molecular content of the tissue. However, there exist several exogenous fluorescence imaging systems that use SFDI and diffuse reflectance methods to provide quantified fluorescence signal. Nonetheless, these systems are limited to external fluorescence agents such as PpIX or treatment-related drugs; they do not offer any quantitative information regarding the molecular composition of the tissue. Moreover, in the literature, there is no available report on macroscopic prostate imaging systems.

We present the development of a robust system capturing hyperspectral endogenous fluorescence, diffuse reflectance, as well as the absorption and scattering coefficients through SFDI to produce quantitative fluorescence information over a macroscopic FOV on RP specimens. The system is used to take whole-prostate snapshot measurements, providing quantitative molecular-based biomarkers over the whole FOV. The information obtained with the system may be used during or after RP to differentiate tissue types, such as prostatic *vs* extra-prostatic or healthy *vs* cancerous, and improve the patient's medical treatment.

The first step of the project was the conceptualization of the acquisition system and data processing algorithms. Optical design was done to reach specifications, such as FOV, depth of field, spatial resolution, etc., adapted to the prostate application and to integrate fluorescence, diffuse reflectance, and SFDI into a compact spectroscopy system with excitation and detection parameters suitable to the samples. Calibration and data treatment processes were elaborated for each acquisition modality to remove system influence and any other undesirable measured factors. Modalities were tested and their performance characterized. Multimodal acquisitions were then made to select a fluorescence quantification algorithm with optimal characteristics and performance for the wide-field system and its application.

Hypothesis 1	Wide-field acquisitions of fluorescence, reflectance and SFDI can be integrated on a spectroscopic system to obtain quantitative information on tissue fluorophores & chromophores.
Objectives	1.1- Design, fabricate the SFDI system. Validate accuracy on tissue phantoms within prostate optical property range. 1.2- Design, fabricate the fluorescence/reflectance spectroscopy system. Conceive data processing algorithms to correct system influence. 1.3- Implement, validate various fluorescence quantification algorithms in tissue phantoms. Select the most adapted to the prostate application.

While the conceptualization of the system was mostly based on measurements on optical phantoms, where the properties are known and the sample geometry is flat, the system had to be adapted to biological samples as the second step of the project. These measurements presented a particular set of challenges due to the uneven sample geometry. Consequently, a surface profile correction was implemented and polarisers were added to mitigate specular reflections. Measurements were then taken on prostate samples. Finally, observations were made on the quality of the results along with preliminary tests of the system's capacity to differentiate tissue by referencing features noted by pathologists following examination of Hematoxylin and Eosin (HE) stainings of the samples, considered as gold standard.

Hypothesis 2	Quantitative fluorescence and absorption/scattering properties obtained with the system present potential for the identification of prostate regions and/or differentiation of healthy and cancerous tissue.
Objectives	2.1- Produce absorption/scattering maps and quantified fluorescence over a whole radical prostatectomy specimen without sample geometry or specular reflection artefacts. 2.2- Compute differentiation potential of the modalities for prostatic *vs* extra-prostatic tissue & benign *vs* malign prostate tissue using statistical analyses.

The following chapter presents an article that details most of the steps undertaken towards the validation of theses hypotheses and objectives, with some additional design considerations and results relegated to the general discussion. The project's scope is more of a proof-of-concept regarding the potential of the acquired biomarkers rather than a complete study of tissue differentiation; additional measurements on prostate specimens leading to the application of a robust data classification model are left to future students.

CHAPTER 4 ARTICLE 1 : DEVELOPMENT OF A WIDE-FIELD OPTICAL SPECTROSCOPY TISSUE CHARACTERIZATION SYSTEM INTEGRATING REFLECTANCE SPECTROSCOPY AND SPATIAL FREQUENCY DOMAIN IMAGING TO QUANTIFY INTRINSIC FLUORESCENCE IN RADICAL PROSTATECTOMY SPECIMENS

4.1 Contents

The paper presented in this chapter was focused on the calibration steps and validation of the various modalities of the imaging system, as well as the quantitative fluorescence results obtained on prostate accompanied with preliminary tests assessing the application to tissue differentiation. Since systems exploiting fluorescence, reflectance and SFDI had already been developed before the study, it was chosen not to show the optical conception and design of the system in the article.

The calibration process was presented in detail and justified in the article, to show the logical steps leading to the final data. Corrections were made to eliminate factors such as the unevenness of excitation across the FOV, the wavelength-dependent transmission of the system, the integration time, dark counts, as well as the sample geometry for SFDI. Also shown is the method of fluorescence quantification. Note that, for the needs of the article, the term *quantified fluorescence* (QF) used in the thesis was changed to *attenuation-corrected fluorescence* (CF).

To investigate the performance of the system, a validation study was conducted. Particular points of interest were the absorption/scattering reconstruction errors for SFDI in low and high absorption cases, leading to the choice of an appropriate reference phantom for prostate measurements, the accuracy of profilometry and subsequent geometrical corrections, as well as the performance of the fluorescence quantification algorithm. Those tests consisted of the validation of hypothesis 1.

Finally, the results obtained on a prostate sample were presented for all modalities. While the sample size was too low to conduct a complete analysis of the results, initial observations were made by using six biologically distinct regions on the prostate as identified on the gold standard by a pathologist. Statistical differences between the regions for quantified fluorescence, μ_a and μ_s' were noted and a differentiation test between prostatic and extra-prostatic tissue using those same modalities presented a similarly significant potential for differentiation. Those measurements and their analysis allowed validation of hypothesis 2.

4.2 Authors & contributions

Before the establishment of the current project in the laboratory of radiological optics of the Polytechnique Montréal, some elements related to SFDI had already been developed. Although it was modified throughout the project, an initial algorithm for the reconstruction of optical properties had been programmed by doctoral student Audrey Laurence. However, there was no functioning SFDI system for measurements before the project. Preliminary work was done for phase-shifting profilometry by doctoral students Guillaume Sheehy and Leticia Angulo, but the algorithm was fully developed and adapted to correct absorption/scattering for the geometry of diffusive samples by Audrey Laurence during the project.

The study presented in the following article was conducted by master's student Emile Beaulieu, doctoral student Audrey Laurence, research assistant Mirela Birlea, doctoral students Guillaume Sheehy and Leticia Angulo, doctors Mathieu Latour and Roula Albadine, urologist Fred Saad, pathologist Dominique Trudel, and professor Frédéric Leblond. The first author's contribution is evaluated at >90% for conception and characterization of the system, elaboration of the acquisition/calibration processes and data treatment algorithms for fluorescence quantification, conduction of the validation experiments for all modalities, as well as measurement and data interpretation of radical prostatectomy specimens. The authors of this paper are affiliated to the Polytechnique Montréal's engineering physics department, the Centre Hospitalier de l'Université de Montréal (CHUM) research center and the University of Montreal's pathology department. The article was submitted to the Journal of Biomedical Optics (*J. Biomed. Opt.*) on July 4^{th}, 2019. The references used in the article are self-contained in the chapter.

4.3 Development of a wide-field optical spectroscopy tissue characterization system integrating reflectance spectroscopy and spatial frequency domain imaging to quantify intrinsic fluorescence in radical prostatectomy specimens

Emile Beaulieu,[a,b] Audrey Laurence,[a,b] Mirela Birlea,[b,c] Guillaume Sheehy,[a,b] Leticia Angulo-Rodriguez,[a] Mathieu Latour,[b,c] Roula Albadine,[b,c] Fred Saad,[b] Dominique Trudel,[b,c] Frédéric Leblond[a,b,*]

[a]Polytechnique Montreal, Dept. of Engineering Physics, C.P. 6079, Succ. Centre-ville, Montreal, Canada, QC H3C 3A7

[b]Centre Hospitalier Universitaire de Montreal Research Center (CRCHUM), 900 Rue Saint-Denis, Montreal, Canada, QC H2X 0A9

[c]University of Montreal, Dept. of Pathology and Cellular Biology, C.P. 6128, Succ. Centre-ville, Montreal, Canada, QC H3T 1J4

Abstract. The development of a multimodal optical imaging system is presented integrating endogenous fluorescence and diffuse reflectance spectroscopy with single-wavelength spatial frequency domain imaging (SFDI) and surface profilometry. The system images specimens at visible wavelengths with a spatial resolution of 70 μm, field of view of 25 cm^2 and depth of field of $\sim$1.5 cm. Phantom experiments are presented that demonstrate the system can reconstruct absorption and reduced scattering coefficient maps using SFDI with <6% errors. A phase-shifting profilometry technique is implemented and the resulting 3-D surface used to compute a geometric correction ensuring optical properties reconstruction errors are maintained to <6% in curved media with height variations <20 mm. The SFDI-computed properties, along with diffuse reflectance spectra, are used to demonstrate, in tissue phantoms, fluorescence correction can be achieved using a diffusion light transport-based model. The system is used to image a human prostate, demonstrating its ability to distinguish prostate tissue (anterior stroma, hyperplasia, peripheral zone) as well as tissue from extra-prostatic regions (urethra, ejaculatory ducts, peri-prostatic tissue). These techniques could be integrated in robotic-assisted surgical systems to enhance information provided to surgeons and improve procedural accuracy by minimizing the risk of damage to extra-prostatic tissue during radical prostatectomy procedures.

Keywords: Spectroscopy, radical prostatectomy, urology, fluorescence, diffuse reflectance, spatial frequency domain imaging.

***Frédéric Leblond**, E-mail: frederic.leblond@polymtl.ca

4.3.1 Introduction

The most common cancer in American men is prostate cancer, which is associated with increasing incidence rates across the world[1–3]. The only curative surgical treatment in prostate cancer is radical prostatectomy, which remains a first-line option in many diagnostics with 1330 procedures per million in 2011 in America. Despite increases in active surveillance, radical prostatectomy is still a mainstream therapeutic option for prostate cancer, especially with the development of robot-assisted surgery[4–8]. Procedure remission rates are strongly influenced by the extent to which completeness of cancer resection is attained[9,10]. Because cancer often extends beyond the prostatic capsule[11], ensuring safety margins is often the adopted surgical strategy. The extent of surgical detection is then determined by multiple factors, including patient pre-surgical PSA levels, clinical stage and pathological findings at diagnosis, as well as expected quality-of-life after the surgery[12–14]. Optimal resection while

minimizing damage to critical genitourinary structures, including the bladder and hard to visualize nerves is a major objective[15]. Smaller margins lower the risk of damage to surrounding tissue and increases post-procedure patient satisfaction[16,17]. However positive margins from un-resected cancer extending beyond the prostate decrease survival rates and result in additional treatments[18,19]. Balancing these two factors can be a challenging task.

Unlike other surgical oncology approaches where co-registration methods with other imaging modalities are used to guide resection (*e.g.* magnetic resonance imaging, MRI, in brain cancer)[20], prostate cancer is not detectable using standard imaging techniques except with MRI in some high-grade cases[21]. This means surgeons rely on low accuracy methods, including prostate-specific antigen (PSA) testing and transrectal ultrasound (TRUS)-guided biopsies, to plan the operation and pre-determine margin size[22]. As a result of the limitations of current prostate cancer diagnostic approaches, there is a need for new tools to enhance intraoperative tissue information and to enable identification of prostate tissue. For example, differentiating prostate tissue from extra-prostatic structures could ensure complete removal of the prostate during radical prostatectomy procedures, reducing the risk of recurrence of the disease which would result in additional disease and treatment related morbidity. It would also minimize the risk of damage to non-prostatic tissue. Moreover, such a surgical guidance tool could benefit robotic assisted surgery, which reports higher rates of genitourinary complications when compared to standard approaches.[23].

Up until now, point probes were used to characterize prostate tissue using optical coherence tomography (OCT)[24], Raman spectroscopy[25], diffuse reflectance spectroscopy[26] as well as exogenous fluorescence from aminolevulinic acid-induced protoporphyrin IX (PpIX)[27] and endogenous fluorescence[28] in millimiter-size fields of view. Endogenous fluorescence results from tissue-native fluorescent molecules, thus giving access to molecular information without the need to inject a tracer[29]. Although most intrinsic tissue fluorophores excitation bands are in the ultraviolet (UV), multiple molecules can still be detected through excitation above the UVA region (>380 nm) into the violet-blue part of the visible spectrum. Those include nicotinamide adenine dinucleotide (NADH) and flavins that can be used as a surrogate for cellular metabolism associated mitochondrial activity[30,31]. Other fluorophores that can be excited with visible light comprise the structural proteins elastin and collagen as well as porphyrins, which were shown to accumulate specifically in some cancers[32]. Intrinsic tissue fluorescence detection has been achieved for multiple tissue types and pathologies[33], including for the detection of cancer in prostate and breast[34]. Although most work in mesoscopic intrinsic tissue fluorescence characterization was done with point probes, it was also adapted in a limited number of studies to macroscopic wide-field imaging in surgical oncology[35,36].

A practical limitation when attempting to detect intrinsic tissue fluorescence is the small quantum yields of the fluorophores when compared to the absorption cross sections of common tissue chromophores (*e.g.* hemoglobin and pigment molecules such as melanin) and elastic scattering from cell nuclei, membranes and organelles. These competing interaction mechanisms affect the fluorescence signal, which is *non-quantitative* in the sense that tissue regions with an homogeneous concentration of fluorophores but with heterogeneous absorption/scattering properties will show different levels of detected fluorescence[37]. As a result, several mathematical models based on light transport in turbid media were developed for point probes to decouple absorption and scattering from fluorescence[38–40]. Although these neglect smaller signal influences in the surgical context such as local pH and depth of signal, with such corrections, numerical values associated with *attenuation-corrected fluorescence* (CF) signals strongly related to molecular content could be obtained, providing high-quality biomarkers for eventual use in advanced data analyses (e.g. machine learning).

Point-probe measurements typically offer fields of view of a few mm^2, which for some surgical applications can be insufficient for clinical acceptance[41,42]. As a result some groups have worked on the development of macroscopic attenuation-corrected fluorescence imaging approaches with attenuation corrections adapted to wide-field imaging geometries, although standard modeling approaches are less readily applicable than for point-probes[43]. However, the advent of spatial frequency domain imaging (SFDI), allowing quantification of absorption/scattering properties across wide field images by using structured imaging, permitted the development of accurate light-transport based corrections[44–46]. This led to the recent application of CF imaging to obtain molecular information in macroscopic field of views[47]. Such systems have been applied on PpIX quantification for skin cancer[48,49], brain tumor surgery[50,51] and photodynamic therapy (PDT) drug concentration monitoring[52]. Performances allowing real-time CF imaging have also been reached[53].

Here we are presenting the development and detailed tissue phantoms characterization of a wide-field spectroscopic imaging system detecting reflectance spectra in the visible range as well as endogenous fluorescence resulting from violet light excitation. The system also integrates SFDI to obtain absorption/scattering coefficients and 3-D surface profile within a spectral band close to the fluorescence excitation wavelength. This information, along with reflectance and fluorescence spectra, is used in the scope of a light transport-based attenuation-corrected fluorescence (CF) model to compute a measure that can be used as a surrogate for the concentration of intrinsic tissue fluorescent molecules. Thus, the goal of the system is to use this biomarker, combined with tissue absorption and scattering coefficients, to characterize biological tissue. The calibration and development process of the system leading to SFDI-reconstructed absorption and reduced scattering coefficients is presented with mea-

surements in both low and high absorption intralipid-based optical phantoms. PDMS solid phantoms are used to implement a geometric correction accounting for sample geometry and fluorescence correction is tested on intralipid optical phantoms. As proof-of-principle, multimodal images (absorption and scattering coefficients, diffuse reflectance and fluorescence, CF) of a human prostate following a radical prostatectomy procedure are presented. To our knowledge, this is the first time macroscopic wide-field CF measurements are presented in terms of intrinsic tissue fluorescence. Statistical analyses are presented with evidence that biologically-distinct prostate regions can be distinguished based on tissue optical properties, including prostatic *vs.* extra-prostatic tissue.

4.3.2 Materials and Methods

4.3.2.1 Wide-field imaging system

4.3.2.1.1 System hardware

The multimodal wide-field system was composed of a central detection branch surrounded by two distinct illumination branches, one for fluorescence & reflectance spectroscopy and one for single-wavelength SFDI (Fig. 4.1). Light detection was achieved using an sCMOS camera with a 4/3" array composed of 2048 x 2048 pixels, each of dimensions 6.5 x 6.5 μm (C11440-22CU, Hamamatsu, Japan). The camera was connected through a relay lens to a liquid crystal tunable filter (LCTF) with operation range between 400 and 720 nm (VIS, Varispec, USA) and a manually adjustable linear polarizer was introduced in the detection path to control tissue specular reflections. A high precision aspherical objective (LM25XC, Kowa, USA) was used as the main interface for image acquisition.

Both illumination branches used the same light source consisting of seven high-power (79 – 536 mW) light emitting diodes (LED) centered at 405, 435, 475, 515, 550, 570 and 630 nm (Spectra X, Lumencor, USA) outputted through a 3 mm-diameter liquid light guide. For the excitation of the various modalities, the LEDs had overlapping spectra and could be powered simultaneously to emulate white light in order to acquire reflectance spectra or individually for fluorescence spectroscopy (405 nm) and SFDI (435 nm). The 405 nm LED was used for fluorescence excitation since it overlapped the absorption spectra of multiple endogenous fluorophores including NADH, flavins, porphyrins and elastin[53]. The liquid light guide output was collimated to ensure direct projection onto the sample. In the case of reflectance & fluorescence, the source was connected to a two-slot optical rail allowing rapid switching between: i) a linear polarizer with optical axis manually adjusted to be at 90° with respect to the linear polarizer in the detection branch, or ii) two successive 390 ± 40 nm OD >6 bandpass filters (BrightLine FF01-390/40-25, Semrock, USA) used to cut off fluorescence

excitation from the measurements. For SFDI, a light engine (CEL5500, DLI, USA) with a digital light processing chipset (DLP5500, Texas Instruments, USA) was used for spatial light modulation. The light engine casing was mechanically re-engineered to accommodate extra lenses, ensuring optical coupling with the liquid light guide. An adjustable linear polarizer was added to the light path to allow control of specular reflections.

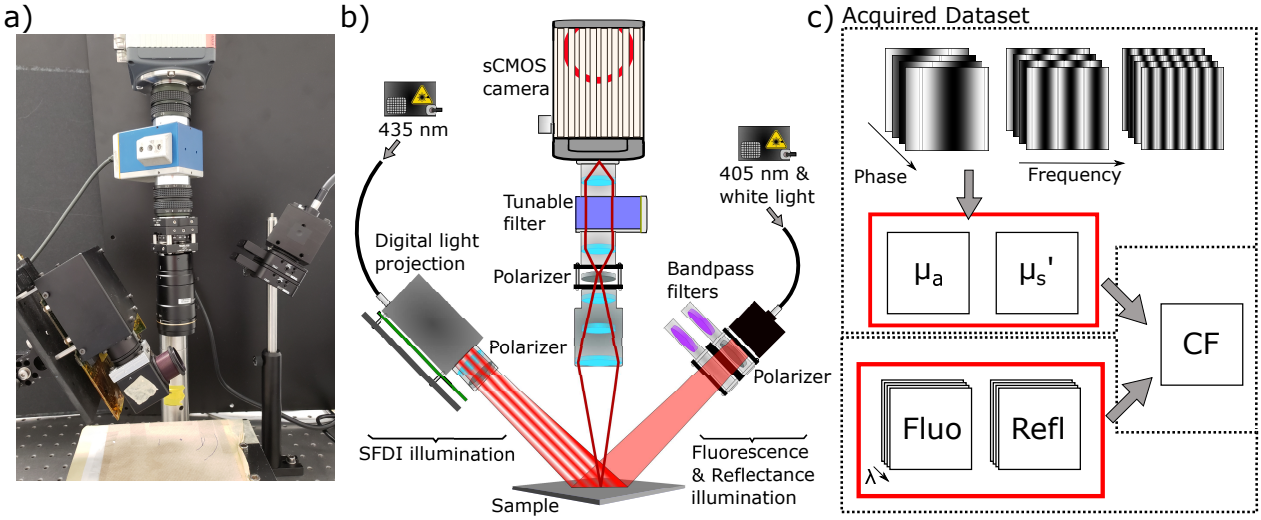

Figure 4.1 (a) Photograph of the multimodal imaging system. (b) System schematics highlighting coupling optics and the two projection branches allowing diffuse reflectance & fluorescence spectroscopy as well as single-wavelength SFDI. (c) Flowchart representing the data acquisition and processing workflow.

4.3.2.1.2 Acquisition control

Data acquisition was done using a custom LabVIEW program (National Instruments, USA) controlling camera and LCTF parameters (number of spectral bands, spectral range, imaging time) for reflectance & fluorescence detection and pattern projection for SFDI measurements (*e.g.* spatial frequency and phase of sine waves). The software implemented an auto-exposure algorithm to adjust imaging time for each wavelength in order to maximize signal-to-noise ratio (SNR). Reflectance & fluorescence spectroscopy measurements were acquired with the LCTF scanning from 420 to 650 nm with steps of 5 nm while SFDI data was acquired at a fixed LCTF wavelength centered at 435 nm.

4.3.2.2 System characterization and data processing

4.3.2.2.1 Imaging specifications

The spatial resolution of the system was determined by imaging a standard 1951 USAF resolution target and defined by the smallest element with distinct contrast. The field of view was quantified with the same measurement by using target elements as scale. The depth of field was also determined using the resolution target, this time varying the height of a z-axis stage on which the sample was deposited to determine the range (in centimeters) for which imaging can be achieved at a pre-specified spatial resolution associated with a drop of 25% when compared to the resolution in the focal plane. Note that these specifications were determined for non-diffusive media to allow comparison to other systems.

4.3.2.2.2 SFDI data calibration and geometric optical properties correction

Spatial frequency domain imaging relies on projecting sine wave patterns at multiple spatial frequencies (k_x) and phases to extract the so-called tissue transfer matrix: $\mathrm{M}_{ac}(k_x)$ [55]. Because this transfer matrix is a function of tissue optical properties (absorption coefficient, μ_a, reduced scattering coefficient, μ_s'), tissue response can be measured at multiple frequencies to recover wide field absorption and scattering images[56]. In order to account for the instrument response function, the technique requires the measured transfer function to be normalized against a reference measurement made on a sample with known tissue optical properties[57]. An intralipid-based liquid phantom was used to compute the reference matrix function and white Monte Carlo simulations (Virtual photonics technology initiative, USA) were used to create a lookup table for the μ_a/μ_s' couples under the hypothesis that the imaged geometry was a flat semi-infinite slab.

A correction algorithm was implement to account for the sample's height and angle, which can otherwise cause errors during the reconstruction of SFDI optical properties[58]. The profile-based correction method consists of normalizing the tissue transfer function using measured reference transfer matrices for a range of distances consistent with expected height variations when imaging specimens[59]. Briefly, by measuring a reference transfer functions at various heights -$\mathrm{M}_{ac,ref}(h)$- a relationship was found between phase variation and height, which allowed to compute a correction factor for every imaged pixel. Angle correction was implemented by multiplying the reference matrix function with the cosine of the angle formed by the normal surface vector and the camera detection axis. The technique used four different phases since this was found to reduce noise in reconstructed 3-D profiles[60].

4.3.2.2.3 Fluorescence and reflectance data calibration

Figure 4.2 shows the calibration/normalization procedure applied for reflectance & fluorescence spectroscopy measurements in order to account for the instrument response function and produce attenuation-corrected fluorescence (CF) images. It included: i) a shading correction based on a reflectance standard (Spectralon, SRM-99, Labsphere, USA) measurement to compensate for inhomogeneities in the illumination field, and ii) a normalization with a spectral irradiance standard (63355, Newport, USA) to account for varying system transmission across wavelengths. The shading correction for reflectance consisted in a division by the normalized hyperspectral reflectance standard measurement. For fluorescence, the images were instead divided by a normalized intensity map of the standard's reflectance at 405 nm. Spectral response variations were accounted for by dividing all sample measurements by a correction curve corresponding to a hyperspectral measurement on the spectral irradiance standard divided by its theoretical spectrum.

4.3.2.2.4 Attenuation-corrected fluorescence

As the final processing step, a tissue light transport-based correction factor was computed and applied to the fluorescence images to produce images in which the fluorescence signal was independent from elastic scattering and absorption from chromophores. Fluorescence attenuation correction at every point in the image was achieved using the SFDI-derived optical properties values and the spectroscopic reflectance measurement. The model developed by Kim et al.[61] for point probe measurements was used, which consists in modelling the attenuation-corrected fluorescence (CF) as

$$CF(\lambda) = \left(\frac{\mu_{a,x}}{1 - R_{t,x}}\right)\left(\frac{F_{raw}(\lambda)}{R(\lambda)}\right), \tag{4.1}$$

where experimental measurements are the fluorescence spectrum $F_{raw}(\lambda)$ and the reflectance spectrum $R(\lambda)$ both measured with the LCTF-based system. The diffusion theory modeled reflectance at the excitation wavelength ($R_{t,x}$) is a function of the internal reflection parameter κ and the reduced albedo a'. These coefficients depend on the refractive index of the sample (n =~1.33 for biological tissues[61]) as well as the absorption (μ_a) and reduced scattering (μ_s') coefficients at the excitation wavelength measured using SFDI.

The assumptions made in deriving the model in Eq. (4.1) were that the tissue absorption at excitation is high when compared to its value at the emission wavelength and that the fluorophore absorption at the excitation wavelength is negligible compared to tissue absorption from chromophores. If satisfied, these allow the approximation of the effect of optical

properties at emission with the diffuse reflectance measurement, thus explaining why only the absorption & scattering properties at excitation are used. Common absorbers found in prostate are water, seminal fluid and hemoglobin[63]. However, for *ex vivo* measurements it is expected that seminal fluid will be the main absorber since blood concentration is much lower than under *in vivo* conditions. Both hemoglobin and seminal fluid have absorption peaks near the fluorescence excitation wavelength at 405 nm with significantly lower values at higher wavelengths in the visible[64,65]. Moreover, although the extinction coefficient for intrinsic tissue fluorophores excited at 405 nm can be important, it is usually orders of magnitude smaller when compared to tissue chromophores[33,49,66]. As a result, both conditions for validity of the CF model in Eq. (4.1) are expected to be satisfied in the prostate when measuring intrinsic tissue fluorescence. It should be noted that the use of this method for multiple fluorophores, such as in endogenous fluorescence, is novel and it is approximated that this does not undermine its validity. Furthermore, due to low LCTF and DLP transmission at 405 nm leading to poor signal to noise in SFDI images at this wavelength, SFDI measurements were conducted at 435 nm. Although this means the optical properties used were not exactly at the excitation wavelength, 435 nm is still within the absorption peaks of the chromophores so this compromise should not have an important impact on the results[64,65].

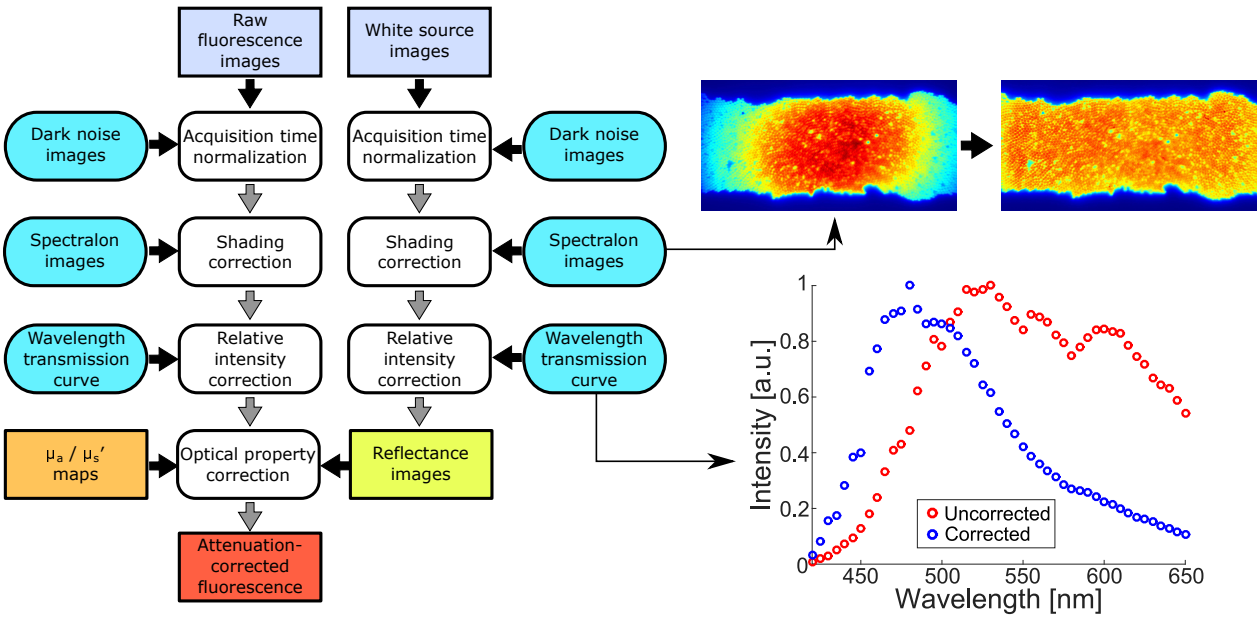

Figure 4.2 Flowchart of data processing for reflectance & fluorescence spectroscopy imaging with images showing an example of shading correction on a fluorescent bead layer. Also shown is a representative relative intensity spectral correction for the instrument response function.

4.3.2.3 SFDI and profilometry measurements

4.3.2.3.1 Low absorption tissue phantoms

Liquid optical phantoms, made with water, intralipid (Sigma-Aldrich, USA) and food coloring dye (McCormick, USA), were used to test the SFDI reconstruction capabilities. Theoretical values of the reduced scattering coefficient were obtained from the literature[67,68] while the absorption coefficient was measured using a custom single-point fibre optics spectrophotometer. A reference set of 72 optical phantoms was made with optical properties (at 435 nm) ranging from $\mu_a = 0.022$ mm^{-1} to 0.44 mm^{-1} and μ_s' = 0.72 mm^{-1} to 2.16 mm^{-1}. The μ_s'/μ_a ratio in this phantom set ranged from 1.64 to 98.1, in most cases satisfying the so-called diffusion approximation[69]. SFDI measurements were made for each phantom at 6 spatial frequencies (k_x = 0.041, 0.082. 0.123, 0.144, 0.164, and 0.246 mm^{-1}), each at 4 different phases ($\Delta\phi$ = 0°, 90° , 180° , 270°). The specific spatial frequencies used were previously determined by measuring optical phantoms with 15 frequencies and testing different subsets to determine the number and value of frequencies minimizing mean error on absorption and scattering coefficients. The conditions used for this experiment correspond to those for most reported SFDI systems, allowing comparison of the system's performance to other groups. The average power of the source over the imaging field of view was ∼0.045 mW/cm^2. Reference phantoms with different optical properties were used to reconstruct optical properties maps for all phantoms and the average reconstructed properties across the imaging field were compared to the theoretical values to quantify accuracy. Error bars on the results were computed as standard deviation across the image. Only results associated with the reference phantom minimizing overall reconstruction errors were reported.

4.3.2.3.2 High absorption tissue phantoms

The optical properties of prostate tissue at our measurement wavelength of 435 nm are not expected to satisfy the diffusion approximation[70–72] in part because the excitation source overlaps high hemoglobin absorption bands[65]. In order to validate SFDI in conditions closer to what is expected in prostate specimens, a second liquid phantom experiment was conducted with 8 phantoms with absorption ranging from $\mu_a = 0.22$ mm^{-1} to 1.32 mm^{-1} and reduced scattering ranging from μ_s' = 0.72 mm^{-1} to 1.92 mm^{-1}. The μ_s'/μ_a ratio in those phantoms ranged from 3 to 1. SFDI measurements were made following the same procedure, processed using the same model and interpreted using the same metrics as with the lower absorption phantoms and the average reconstructed error computed. These results guided the selection of an SFDI reference phantom maximizing μ_s' and μ_a reconstruction accuracy in an optical property range representative of the prostate sample.

4.3.2.3.3 Profilometry measurements

An experiment using a solid phantom with homogeneous optical properties was devised to validate the profilometry technique and the geometric correction applied when computing optical properties of irregular surfaces. Using a PDMS base, the optical properties were varied using TiO_2 for scattering and nigrosin for absorption[73]. The solution was mixed and cast into a mold in the form of a staircase with 8 steps of equal heights totalling 24 mm. Two phantoms were made, each with different optical properties at 435 nm: (μ_a, μ_s') = (0.02 mm^{-1}, 0.88 mm^{-1}) and (μ_a, μ_s') = (0.026 mm^{-1}, 0.62 mm^{-1}). Using the lower absorption phantom as reference, the 3-D profile and the transfer matrix (M_{ac}) function were computed for the higher absorption phantom. Profilometry measurements were made at 435 nm with 4 phases ($\Delta\phi = 0°$, 90° , 180° , 270°) at 8 spatial frequencies (k_x = 0.0041, 0.0165, 0.041, 0.082, 0.123, 0.144, 0.164, 0.246 mm^{-1}). Height and optical property values were averaged over 8 regions, each corresponding to a step, and error bars were computed as standard deviationThe maps of optical properties before and after applying the geometric correction were compared by computing the average optical properties reconstruction error for all regions of interest.

4.3.2.4 Fluorescence and reflectance spectroscopy tissue phantoms

Liquid phantoms were made to evaluate the CF technique using the fluorophore PpIX, which was chosen because it had an excitation band at 405 nm. For fluorescence, light fluence was ∼4.5 mW/cm^2 while for reflectance the sum of all LEDs amounted to ∼15 mW/cm^2. In total, 9 optical phantoms were made with fluorophore concentrations 1.25, 2.5, 5 μg/ml, absorption coefficients μ_a = 0.05, 0.15, 0.25 mm^{-1} and reduced scattering μ_s' = 0.75, 1.15, 1.5 mm^{-1}. These phantoms were made ensuring they satisfy the assumptions of the model in Eq. (4.1). Both reflectance and fluorescence measurements were made from 420 to 650 nm with steps of 5 nm (47 bands in total). SFDI measurements were made at 435 nm (∼0.045 mW/cm^2) with 8 spatial frequencies (k_x = 0.0041, 0.0165, 0.041, 0.082, 0.123, 0.144, 0.164, 0.246 mm^{-1}) and 4 phases. The CF technique was evaluated based on the intensity of the 635 nm PpIX emission peak by quantitatively evaluating the correlation between the real fluorophore concentration and the raw fluorescence or the CF values computed from Eq. (4.1). The value used was the CF average over the image and error bars corresponded to standard deviation. The wavelength at which the algorithm is tested has no impact on the results, as it can be applied identically at each emission wavelength.

4.3.2.5 Ex vivo human prostate imaging

A prostate specimen was imaged from a patient that underwent radical prostatectomy at the Centre Hospitalier de l'Université de Montréal (CHUM) and gave informed consent to participate in the institution's prostate cancer repository. Inclusion criteria were that preliminary biopsy results produced more than 2 positive cores with >10% of the core being cancerous. Excised prostates weighing <35 g were excluded from the study. Following surgery, the whole organ was sent to the pathology ward where it was weighed, inked and identified according to institutional standards. A 5-10 mm slice was cut, placed between 2 cardboard sheets and immersed in 0.9% NaCl (4° C) prior to being transported to the optical imaging laboratory at the CHUM research center where the multimodal optical imaging system is located. A photograph of the prostate was taken followed by measurements with the system (<30 min). The specimen was then reintegrated into the standard pathology workflow. Inspection of the stained slices by a pathologist led to the identification of the following biologically distinct prostate regions: 1) anterior stroma, 2) urethra, 3) hyperplasia, 4) ejaculatory ducts, 5) peri-prostatic, 6) peripheral zone. The regions were then spatially registered with the spectroscopic/SFDI measurements as shown in Fig. 4.7.

Optical imaging was done using the same illumination/acquisition parameters as for the phantom experiments in Section 4.3.2.4. On average, detection integration time was 4 s per band for reflectance and 5 s per band for fluorescence, totalling 188 s and 235 s, respectively. Due to high prostate absorption and very limited illumination power (>2 orders of magnitude smaller than levels allowed for skin according to ANSI laser safety standards), 10 s exposure time was required for each SFDI spatial frequency and phase for a total of 320 s. Reconstruction of absorption/scattering coefficients with SFDI was done using a transfer matrix computed based on measurements from the high absorption reference phantom. Using sample average μ_a and μ_s', an estimation of system penetration depth could be obtained with a Monte-Carlo model[74]. Optical properties (μ_a, μ_s' and CF) were then averaged over each of the 6 prostate regions and univariate statistical analyses performed to test whether optically-derived properties could be used to distinguish them. Specifically, a Kruskal-Wallis test was performed for each source of optical contrast between all prostate regions and boxplots were produced showing median (2^{nd} quartile, Q2), 1^{st} quartile (Q1), and 3^{rd} quartile (Q3), interquartile range (IQR), minimum value (Q1 - 1.5 x IQR) and maximum value (Q3 + 1.5 x IQR) as well as outliers. Regions 1,3 and 6 were then grouped as prostatic tissue and regions 2,4 and 5 as extra-prostatic tissue. Boxplots were produced and a Kruskal-Wallis test performed to test the hypothesis that the two tissue categories could be distinguished.

4.3.3 Results

4.3.3.1 Characterization of the imaging system

Based on measurements from the resolution target, the system had a spatial resolution of 70 μm, a field of view of 5.5 x 5.5 cm and a depth of field of 1.5 cm. An image of the resolution target taken with the system is presented in fig. 4.10 (appendix). Although they were determined for non-diffusive media, these technical specifications seem consistent with macroscopic whole prostate tissue interrogation at mesoscopic scales as well as with expected height variations (typically <1 cm) when imaging prostate specimens.

4.3.3.2 SFDI and profilometry

4.3.3.2.1 Low tissue absorption regime

For each phantom, the SFDI-recovered optical properties (μ_a, μ_s') were averaged over the imaging field of view and the standard deviation evaluated. The reference phantom used for image reconstruction had $\mu_a = 0.05$ mm^{-1} and $\mu_s' = 1.2$ mm^{-1}. The average error (across all phantoms) from the theoretical values was 5.2% for absorption and 3.9% for scattering. Figure 4.3 (a) and (b) shows the reconstructed optical properties against the theoretical properties of the phantoms. The average standard deviation was 7.2% for μ_a and 3.6% for μ_s'. When restricting the optical properties to $\mu_a \leq 0.11$ mm^{-1} for absorption, average errors were 5.1% for μ_a and 3.2% for μ_s'. The average error on the excluded phantoms (0.17 mm^{-1} $\leq \mu_a \leq$ 0.44 mm^{-1}) was 5.6% for μ_a and 5.5% for μ_s'. However, when using a reference phantom of 0.3 mm^{-1} absorption and 1 mm^{-1} reduced scattering on those high absorption phantoms, average errors of 4.3% and 3.9% were obtained.

4.3.3.2.2 High tissue absorption regime

For high absorption phantom experiments, reconstructions were based on a reference phantom with $\mu_a = 0.66$ mm^{-1} and $\mu_s' = 1.1$ mm^{-1}. Results obtained are shown in Fig. 4.3 (c) and (d). Average errors of 5.2% and 4.4% were obtained for absorption and reduced scattering, respectively. The average standard deviations were 5.2% and 5.0%for absorption and reduced scattering.

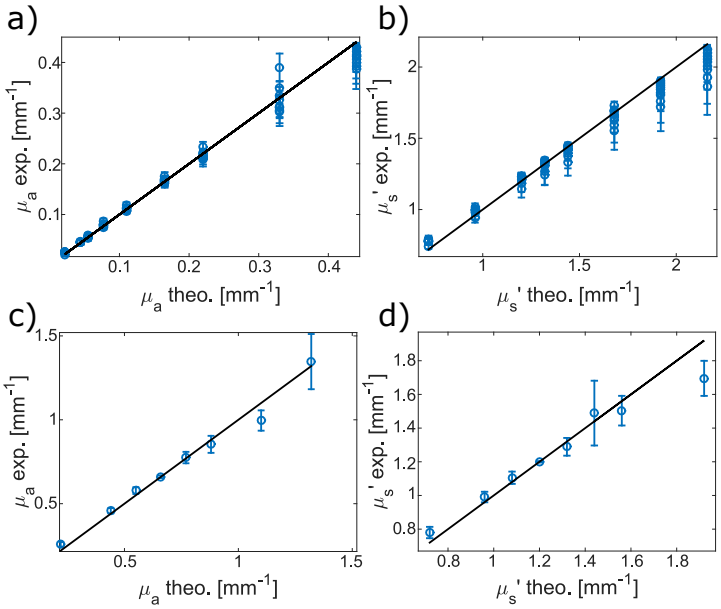

Figure 4.3 Experimental average *vs.* theoretical SFDI optical properties: (a) absorption coefficient in the low absorption regime, (b) reduced scattering coefficient in the low absorption regime, (c) absorption coefficient in the high absorption regime, (d) reduced scattering coefficient in the high absorption regime. Each point in (a) and (c) is associated with a different reduced scattering value and each point in (b) and (d) is associated with a different reduced absorption value

4.3.3.2.3 Profilometry

Implementation and validation of the profilometry correction to optical properties reconstruction with SFDI was demonstrated from measurements on the staircase phantoms shown in Fig. 4.4a. Figure 4.4b shows the recovered height values using the profilometry technique, while Fig. 4.4c and Fig. 4.4d show the SFDI-computed absorption and reduced scattering coefficients on each step, respectively, with and without the geometric correction applied. The geometric correction allowed to reduce the average error on all steps from 127% to 3.3% for absorption and from 28% to 2.5% for reduced scattering.

4.3.3.3 Fluorescence and reflectance spectroscopy

The attenuation-corrected fluorescence (CF) as well as the uncorrected (raw) fluorescence from the PpIX peak at 635 nm are shown in Fig. 4.5 as a function of the real fluorophore concentration (C_{PpIX}) in the phantoms. Figure 4.5a shows raw fluorescence measurements for all μ_a and μ_s' values evidencing almost no linear trend (correlation) with the real PpIX concentration (R^2 = 0.42). This is because, for a given concentration of PpIX, different

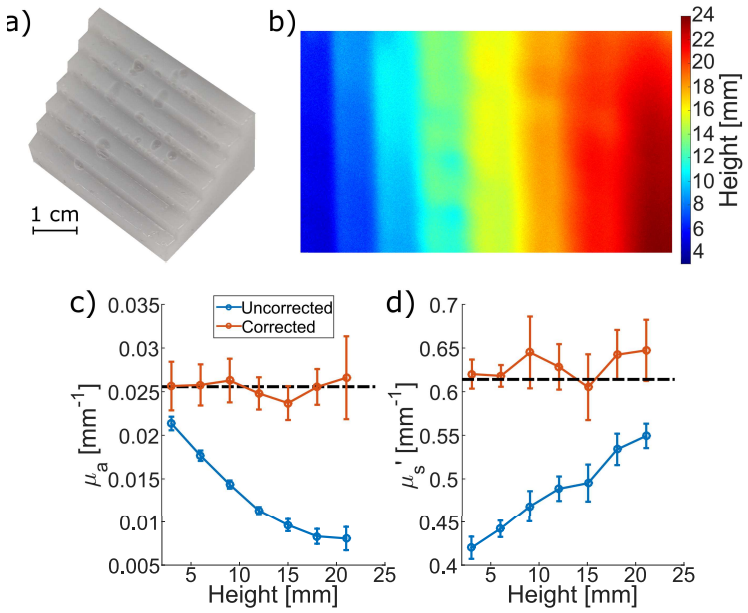

Figure 4.4 (a) Photograph of a staircase phantom, (b) reconstruction of the phantom surface with the profilometry technique. SFDI-reconstructed (c) absorption and (d) reduced scattering coefficients averages on steps with and without the geometric correction.

variations in absorption and scattering affect the level of detected light and can be misconstrued as variations in fluorophore concentration. However, Fig. 4.5b shows that using the CF model improved the correlation between real concentration and detected signals to $R^2 = 0.83$.

4.3.3.4 Ex vivo human prostate imaging

Figure 4.6 shows images of the prostate specimen slice for all modalities, including the absorption coefficient (in mm^{-1}), the reduced scattering coefficient (in mm^{-1}) as well as reflectance, raw fluorescence and attenuation-corrected fluorescence (CF). Each point on the reflectance, fluorescence and CF images are spectra (Fig. 4.7). The fluorescence correction algorithm was applied at each emission wavelength separately. To simplify graphical representation of the data, all images were dimensionally reduced by computing and showing only the sum over all detected wavelengths. The optical properties maps for reflectance are presented at 435 and all data were corrected with the geometric correction from the profilometry technique. To highlight how much the geometric correction impacted the images, Fig. 4.11 (Appendix) shows the reconstructed 3-D profile of the prostate specimen and displays both corrected and uncorrected images in terms of absorption, reduced scattering and CF. Striped patterns

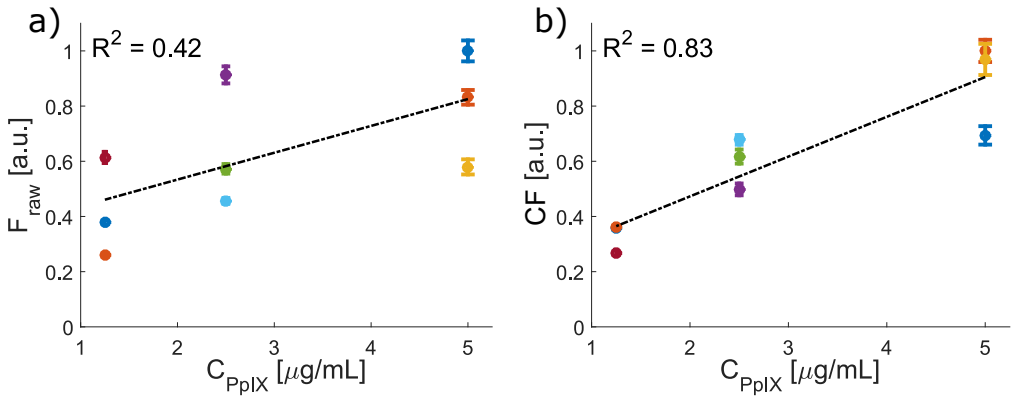

Figure 4.5 Measure of average PpIX emission peak intensity correlation to real PpIX concentration in liquid optical phantoms as an indicator of the impact of absorption and scattering on emission for (a) raw fluorescence and (b) attenuation-corrected fluorescence. Each phantom is represented by a point of a specific color persistent through (a) and (b).

visible on the sample height reconstruction can be explained by noise causing inaccuracies in phase demodulation, which appear amplified due to low overall height variation. Using sample average $\mu_a = 0.52$ and $\mu_s' = 1.71$, a penetration depth averaging 513 μm across all spatial frequencies for 75% of signal was found. This shallow depth allows the usage of system specifications for non-diffusive media as an appropriate estimator of actual system performance.

Table 4.1 presents the average values and standard deviation for absorption, scattering and CF for each of the 6 biologically distinct regions identified by the pathologist. The average SNR per detection band for the reflectance signal is also reported to highlight potential decreases in signal quality in certain regions of interest. The SNR was computed as the square root of total detected light intensity assuming all measurements were shot noise (photonic noise) dominated. Figure 4.8 shows the corresponding boxplots associated with average SNR, absorption and reduced scattering coefficients as well as CF area under curve. A Kruskal-Wallis test combined with pairwise comparisons demonstrated that, for all three sources of optical contrast, every region showed statistically significant differences from one another ($p<0.01$). To highlight the impact of the geometric correction, Table 4.2 (Appendix) shows the average values and standard deviation for absorption, scattering and CF with and without taking the reconstructed 3-D profile into consideration.

The data was further divided into prostatic (regions 1, 3, 6) and extra-prostatic tissue (regions 2, 4, 5) categories and Fig. 4.9 shows the corresponding boxplots associated with average SNR, absorption and reduced scattering coefficient as well as CF. A Kruskal-Wallis test

demonstrated that, for all three source of optical contrast, prostatic and extra-prostatic tissue showed statistically significant differences from one another ($p<0.01$).

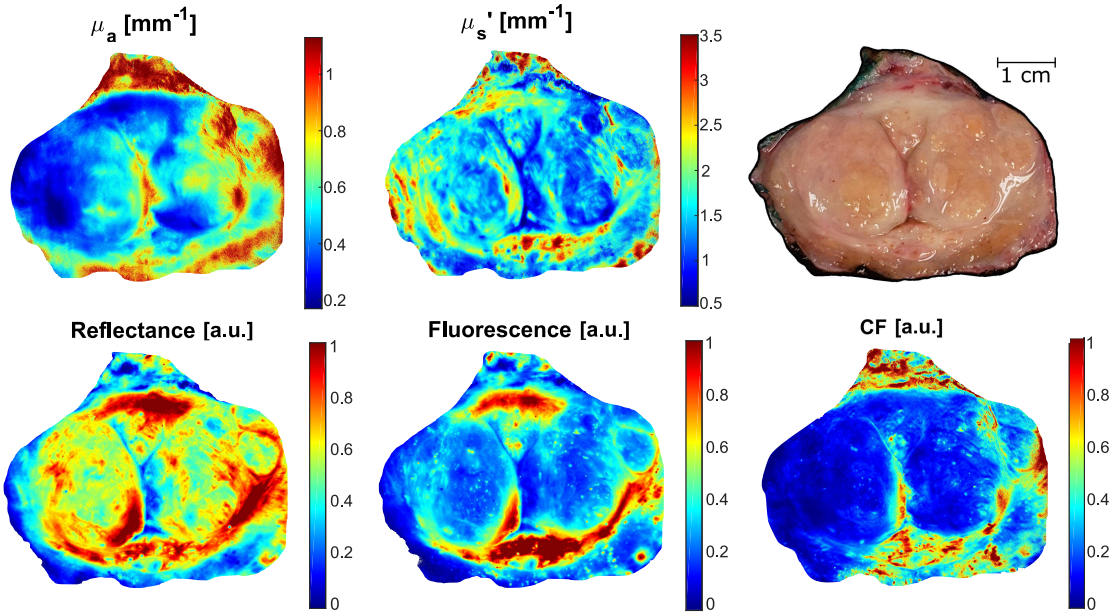

Figure 4.6 Photograph and multimodal optical spectroscopy images of a prostate specimen slice in terms of the absorption coefficient, the reduced scattering coefficient, the reflectance (integral under the curve for every spectrum), the raw fluorescence (integral under the curve for every spectrum) and the attenuation-corrected fluorescence (integral under the curve for every spectrum).

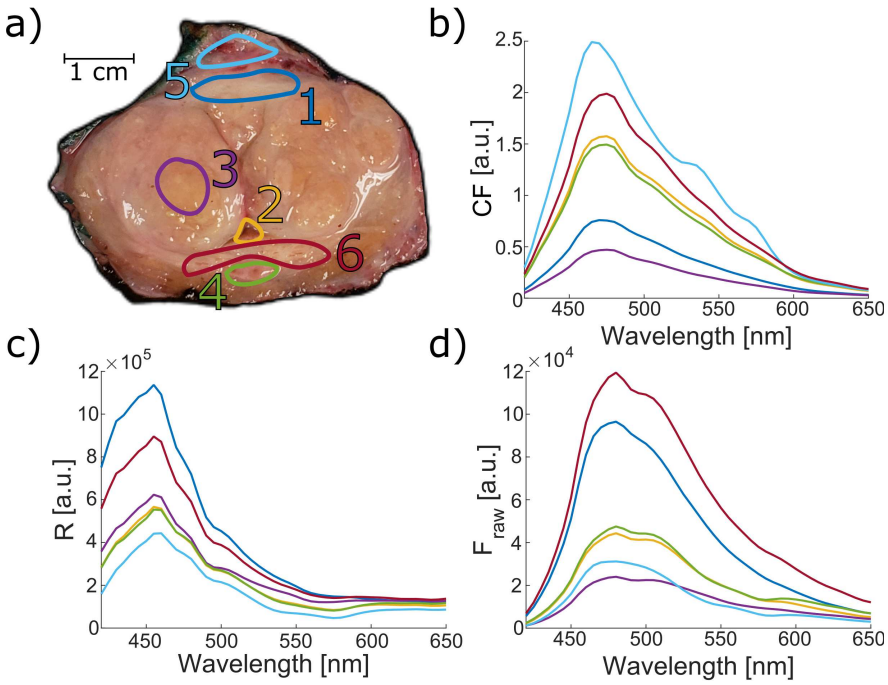

Figure 4.7 (a) Photograph of the prostate specimen with biologically distinct regions identified by a pathologist: 1) anterior stroma, 2) urethra, 3) hyperplasia, 4) ejaculatory ducts, 5) peri-prostatic, 6) peripheral zone. Average spectra computed for each region of interest: (b) attenuation-corrected fluorescence (CF), (c) reflectance and (d) raw fluorescence. No legend is provided for the spectra but the colors for the contour delineations in (a) match those of their associated spectra in (b), (c) and (d).

Table 4.1 Average and standard deviation of quantitative characteristics for each region of the prostate specimen interrogated with the multimodal spectroscopic imaging system, including the number of image pixels over which they were computed.

Prostate region	**# of pixels**	$\overline{SNR}$**/band**	**CF [a.u.]**	μ_a **[mm^{-1}]**	μ_s**'[mm^{-1}]**
Anterior stroma (1)	14432	207 ± 13	15.2 ± 2.4	0.30 ± 0.06	2.09 ± 0.24
Urethra (2)	1938	141 ± 35	32.6 ± 10.3	0.74 ± 0.09	1.23 ± 0.53
Hyperplasia (3)	28942	112 ± 8	9.7 ± 2.1	0.43 ± 0.07	1.44 ± 0.19
Ejaculatory ducts (4)	1498	149 ± 15	31.1 ± 5.0	0.66 ± 0.08	1.60 ± 0.38
Peri-prostatic (5)	9203	112 ± 31	53.1 ± 27.3	1.22 ± 0.31	1.88 ± 1.03
Peripheral zone (6)	19813	237 ± 28	40.9 ± 11.3	0.52 ± 0.10	2.43 ± 0.46

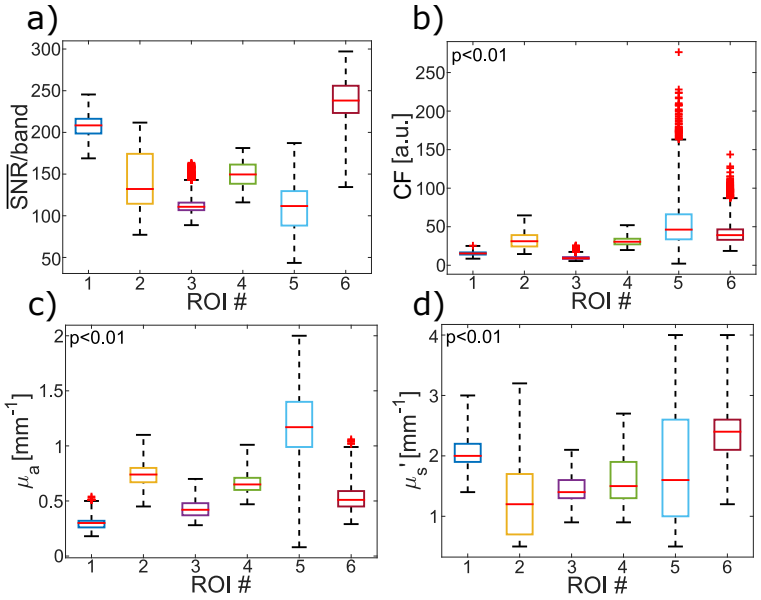

Figure 4.8 Boxplots comparing (a) the SNR per spectral band, (b) the attenuation-corrected fluorescence (CF), (c) the absorption coefficient and (d) the reduced scattering coefficient of all prostate regions of interest (ROI): 1) anterior stroma, 2) urethra, 3) hyperplasia, 4) ejaculatory ducts, 5) peri-prostatic, 6) peripheral zone. Outliers are represented as red crosses.

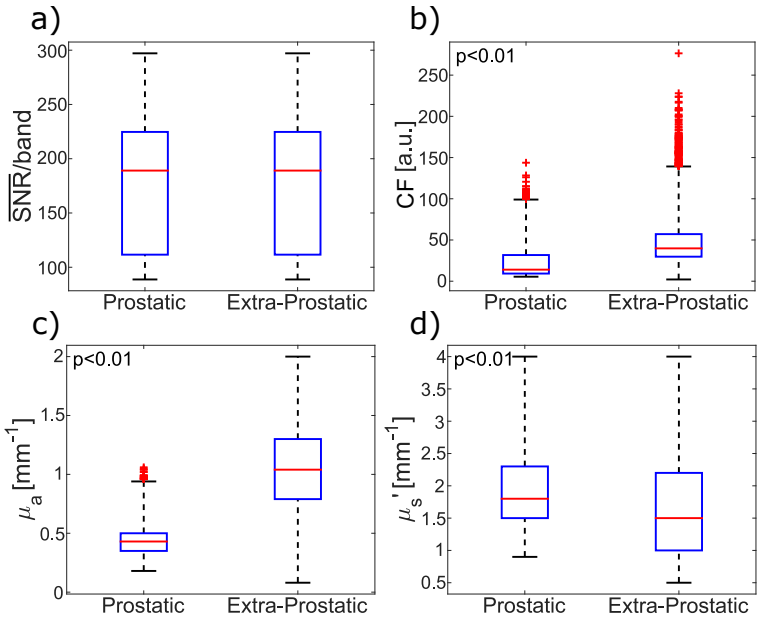

Figure 4.9 Boxplots comparing (a) the SNR per spectral band, (b) the attenuation-correction fluorescence (CF), (c) the absorption coefficient and (d) the reduced scattering coefficient between prostatic and extra-prostatic regions of the specimen. Outliers are represented as red crosses.

4.3.4 Discussion and Conclusions

This study presented the development and tissue phantoms validation of a multimodal wide-field imaging system as well as initial proof-of-concept *ex vivo* measurements in a human prostate, demonstrating new quantitative tissue biomarkers that could potentially distinguish biologically-distinct regions, including prostatic *vs.* extra-prostatic structures. It is the first step in a larger-scale project with the goal of automating tissue characterization during radical prostatectomy procedures to limit the risk of tissue damage and eventually assess whether the system can detect cancer that has invaded tissue beyond the prostate.

In the SFDI-based reconstruction of absorption and reduced scattering that were reported here, the average error across both low and high absorption phantom experiments were similar to other studies[52,55,75–78]. However, there was a small increase in reconstruction error (+0.5%) for reduced scattering in the high absorption dataset when compared to the low absorption dataset. It should be noted that part of the observed errors could be explained by inherent uncertainties associated with the properties used as *theoretical* values for the optical phantoms. For phantoms with $\mu_a = 0.17$ mm^{-1} to 0.44 mm^{-1}, reconstructions based on a reference phantom with $\mu_a = 0.05$ mm^{-1} led to increased errors (0.4% for μ_a, 1.6% for μ_s') when compared with the average dataset results (*i.e.* $\mu_a = 0.022$ mm^{-1} to 0.44 mm^{-1}). When choosing a reference phantom of similar albedo ($\mu_a = 0.3$ mm^{-1}), reconstruction errors decreased by 1% when compared to the average dataset error. This phenomenon was also observed in other work and highlights the importance of choosing a reference with optical properties as close as possible to the interrogated tissue associated with the biological application of interest[55]. Despite reported decreases in performance for the high absorption phantom experiments, the reference used for that dataset led to acceptable system performances across a range of absorption and reduced scattering coefficients representative of prostate samples. Options to further improve the results would be to implement another model for SFDI developed by Kanick et al[79] or to use an empirical lookup table[69] to increase performance in high absorption media.

The profilometry technique was able to reconstruct a staircase phantom of 24 mm height with distinct steps of 3 mm height differences. When surface profile was not accounted for in SFDI-reconstructed optical properties maps, the impact of height differences was observed to be more pronounced in absorption than reduced scattering. However, the error in absorption was drastically reduced once a geometric correction was implemented and reduced scattering results were also improved significantly. The profilometry-based geometric correction performed well across the whole 24 mm height range and this was preliminarily deemed appropriate for imaging prostate specimens where height variations are expected to be <10 mm.

The residual error bars on reconstructed absorption and scattering of the staircase phantom -after height correction- were mainly caused by reconstructed height variations within each stair and could be a consequence of bubbles on the surface of the PDMS phantom.

In the fluorescent phantom studies, the calibration procedure and the correction model were able to remove the instrument response function and to a large extent correct for non-fluorescence attenuation factors despite the relatively large spread in absorption and reduced scattering coefficients compared to other PpIX quantification studies[53,61,80,81]. In fact, the CF method significantly improved the correlation between real PpIX concentration and the fluorescence intensity measurements from $R^2 = 0.42$ to 0.83. It can be observed that the highest intensity emitters in F_{raw}, corresponding to (μ_a, μ_s') = (0.05, 0.75) mm^{-1} phantoms, are overcorrected to lower intensities by the CF method. In these phantoms, chromophore concentration is low, thus making fluorophore absorption significant. This causes an overestimation of μ_a in the SFDI reconstruction and thus an intensity decrease in CF. The overcorrection increases in severity with increasing fluorophore concentrations, which supports this explanation. As fluorophore concentrations are low and chromophore absorption high in biological tissue, this will not affect results on prostate specimens[33,49,66].

An important challenge in developing the multimodal imaging system was signal contributions from specular reflections. Although specular reflections were always negligible in liquid phantoms, they had an important impact when imaging biological tissue including prostate specimens. The illumination and detection polarisers were originally crossed at exactly 90° but this often led to images with regions where signal was dominated by specular reflections. This was caused by the preferential polarization of elements in the detection system, notably the LCTF. By allowing manual adjustment of both polarisers, they could be crossed in a specific orientation minimizing specular reflections for all modalities while maintaining high transmission across the preferential polarisation axis of the system.

The optical properties maps for the prostate specimen showed distinct features for absorption and reduced scattering, evidencing both phenomena were reconstructed with minimal optical contrast crosstalk. Introducing the profilometry-based correction helped further decouple sample geometry artefacts from those maps. In fact, the geometric correction appeared to correct those effects efficiently since there were mostly no noticeable variations in absorption and scattering that matched height/angle variations visually detected either in the photograph of the prostate or its 3-D profile. Some biologically-distinct regions, such as the urethra, could be clearly distinguished from surrounding tissue in the absorption/scattering maps and were also characterized by a geometric depression.

Overall, absorption values were high in the prostate and on average of the same order as

reduced scattering, justifying the use of a high absorption reference phantom in SFDI reconstructions. No values for comparison were found in literature, with most studies measuring absorption and scattering in the 600-1000 nm range which gives results unrepresentative of the 435 nm wavelength[72]. There were important variations in optical properties within the imaged sample, potentially resulting in uneven accuracies in optical properties reconstruction across the imaging field. This is since, as observed in the liquid phantom experiment, the SFDI reconstruction accuracy decreases when absorption and reduced scattering values differ greatly from that of the reference phantom. One approach to reduce this problem could be to use multiple reference optical phantoms, which would allow the selection of the most appropriate reference for each region of the sample following a rapid initial reconstruction. The detected trends in absorption and scattering in the prostate were also evidence that the fluorescence correction model was valid since the light transport conditions used in deriving it were respected.

Fluorescence and reflectance spectroscopy images were also free of specular reflection artefacts. Furthermore, because these signals are not entirely uncorrelated, there were image features seen in the SFDI images that could also be seen in the spectroscopy images. As an example, the anterior stroma, which is characterized by a low absorption coefficient, also featured high reflectance and fluorescence. After applying the geometric correction and the fluorescence correction model, the resulting CF image was not visibly dependent on the SFDI-derived maps or any other geometrical features. The only still noticeable feature was the urethra geometric depression, representing only a small fraction of the sample.

The fluorescence spectra acquired at each point in the image presented a similar shape to that of other studies for prostate tissue and to other biological tissue excited at similar wavelengths; although direct comparisons were not found[82,83]. The fluorescence spectrum of the sample's main chromophore also presents resembling spectral features[64]. The reflectance spectra did not present typical features associated with hemoglobin since it is not the main absorber in the prostate samples. No studies using prostate slice samples were found for comparison. Due to the validation of the system's modalities in phantoms and the results of attenuation correction on prostate, it could be asserted that CF images acquired with the system gave access to molecular-based information of the sample, thus fulfilling the goal of providing quantitative data for tissue analysis.

Statistical analyses of the prostate imaging results revealed that all comparisons between regions had a significant p-values for absorption, reduced scattering and CF area under curve. Note that this analysis does not use the full potential of the CF biomarker, since several features on the spectrum could be used as features for differentiations, as opposed

to the singular values of μ_a and μ_s'.In the boxplots, the median can highlight absolute value differences in optical properties between regions, the IQR can be used as a surrogate for tissue heterogeneity and the maximum, minimum and number of outliers can be indicators of extreme variations in data that may have a biological origin but could also be attributable to low levels of data SNR or to artifacts due to the geometric correction not being able to fully account for tissue curvature changes. Most regions had noticeable differences in median values for all modalities. Although there were some exceptions, such as the urethra and ejaculatory ducts in CF, these differed significantly in IQR and maximum-minimum values. Peri-prostatic tissue tended to have higher variability but was also the region with the lowest SNR in reflectance signal, potentially explaining this observation. In general, CF had a smaller IQR compared to the other sources of optical contrast but it had the highest number of outliers. This could be traced back to the noise amplification due mathematical operations (divisions and multiplications) required to apply the CF model. On the other end, absorption had more marked differences in median and IQR between regions than other modalities, meaning chromophore concentrations varied importantly. It was also noted that μ_s' values had the highest heterogeneity for all regions. However, there was a significant variation in SNR between the regions, with several medians and IQR that prevented a straightforward visible interpretation of the results when comparing individual regions.

When comparing the prostatic and extra-prostatic tissue, the p-values indicated again that all modalities showed potential for differentiation. The difference in median was small for CF, but prostatic tissue presented a different Q1-Q2-Q3 distribution, had a smaller maximum-minimum range and less outliers. Absorption had significant median differences and values did not overlap in IQR. Reduced scattering presented a difference in medians and IQR. Furthermore, the SNR was very similar between the two categories, meaning differences between tissue categories were likely not due to noise-induced variability.

In summary, the prostate imaging results demonstrate the system's capacity to differentiate biologically-distinct regions with similar visual aspect. However, while making these preliminary observations in the data, it is important to keep in mind that the low number of samples prevents immediate conclusions as to the actual performance of the obtained biomarkers. Further steps in data analysis would include a more thorough evaluation of the CF biomarker by using its whole spectrum in machine learning algorithms to find significant spectral features. Although the current acquisition time of ~15 minutes is unsuitable for surgical applications, it could be improved by ~2 orders of magnitude by increasing illumination power, currently significantly lower than ANSI safety standards, and replacing the LCTF, which has <10% transmission in certain spectral bands. In order to further test the use of CF combined with SFDI-reconstructed optical coefficient maps for prostatic tissue differen-

tiation, the system should be used in a larger scale study on multiple prostates. This would lead to the creation of a large dataset for the organ containing information based on multiple modalities. Referencing these images with histopathology would allow thorough statistical analysis, establishing more firmly the potential of the technique for tissue differentiation, notably between prostatic and extra-prostatic tissue and eventually cancerous and healthy tissue.

4.3.5 Appendix

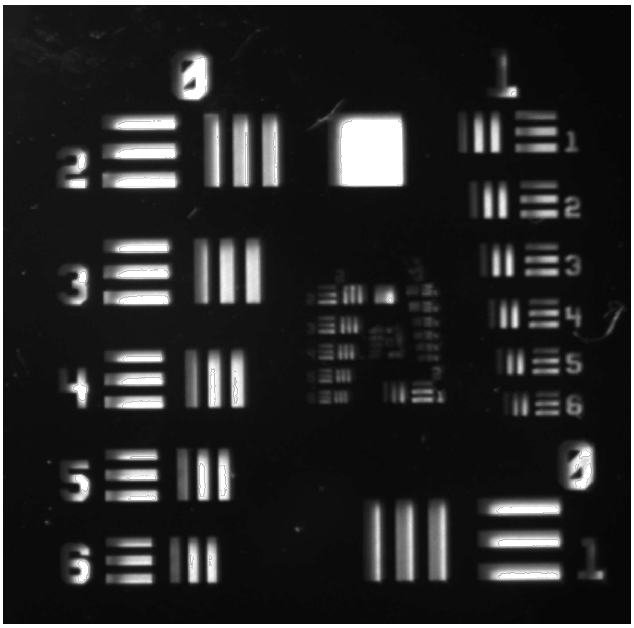

Figure 4.10 Image of a USAF resolution target taken by system (cropped to region of interest)

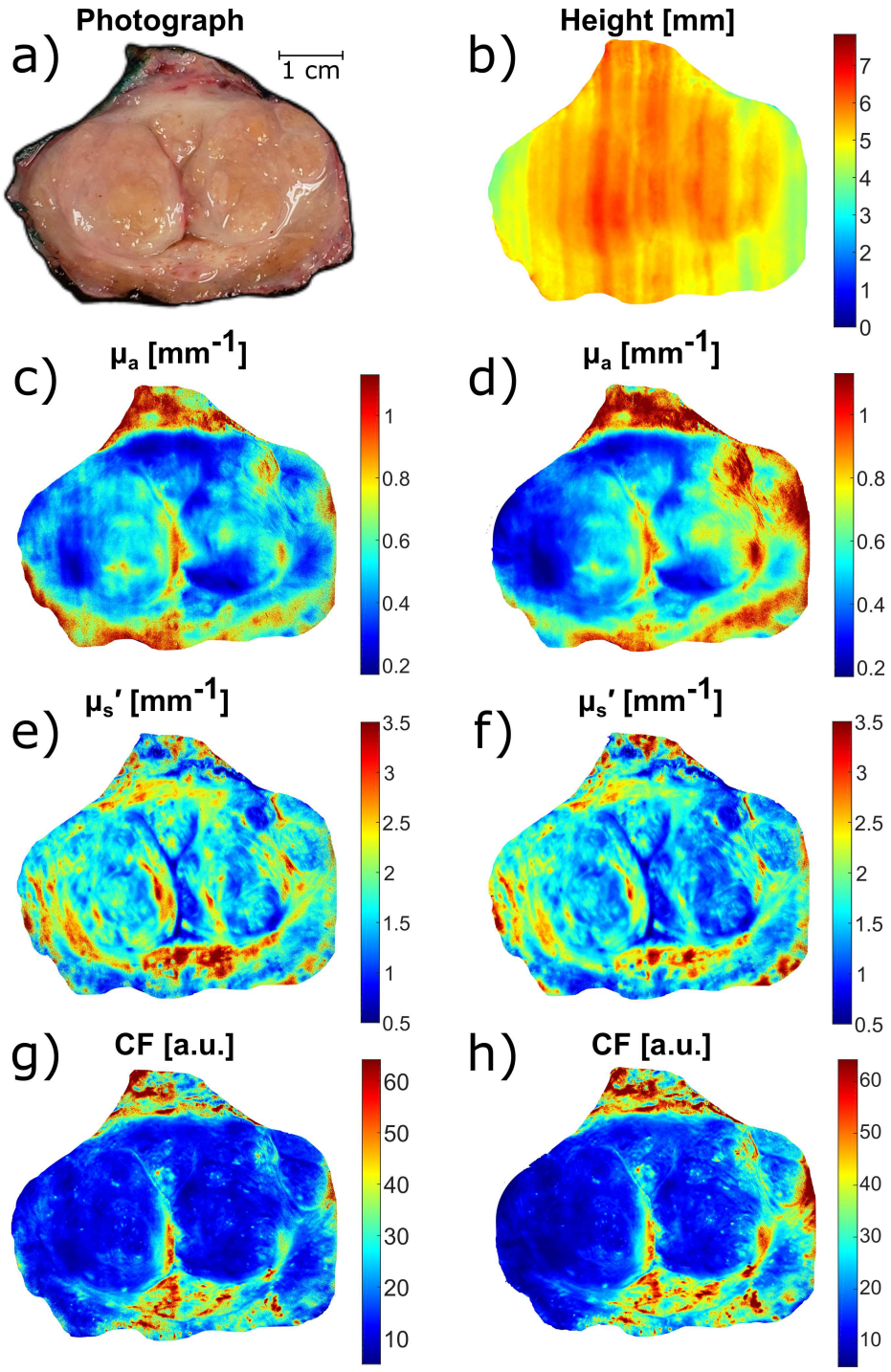

Figure 4.11 (a) Photograph and (b) 3-D profile of a prostate specimen slice. Multimodal optical spectroscopy images of the same specimen slice in terms of the absorption coefficient (c) with and (d) without geometry correction, the reduced scattering coefficient (e) with and (f) without geometry correction and the attenuation-corrected fluorescence (CF) (integral under the curve for every spectrum) (g) with and (h) without geometry correction.

Table 4.2 Average and standard deviation of quantitative characteristics for each region of the prostate specimen interrogated with the multimodal spectroscopic imaging system with and without the profilometry-based sample geometry correction.

Prostate region	**CF [a.u.]**	**CF_{corr} [a.u.]**	μ_a **[mm^{-1}]**	$\mu_{a,corr}$ **[mm^{-1}]**	μ_s**'[mm^{-1}]**	$\mu_{s,corr}$**'[mm^{-1}]**
Anterior stroma (1)	12.6 ± 2.1	15.2 ± 2.4	0.25 ± 0.04	0.30 ± 0.06	2.31 ± 0.24	2.09 ± 0.24
Urethra (2)	33.7 ± 12.7	32.6 ± 10.3	0.76 ± 0.14	0.74 ± 0.09	1.40 ± 0.68	1.23 ± 0.53
Hyperplasia (3)	11.1 ± 2.1	9.7 ± 2.1	0.49 ± 0.06	0.43 ± 0.07	1.59 ± 0.25	1.44 ± 0.19
Ejaculatory ducts (4)	29.2 ± 5.9	31.1 ± 5.0	0.62 ± 0.10	0.66 ± 0.08	1.77 ± 0.47	1.60 ± 0.38
Peri-prostatic (5)	45.7 ± 26	53.1 ± 27.3	1.04 ± 0.32	1.22 ± 0.31	1.66 ± 0.87	1.88 ± 1.03
Peripheral zone (6)	38.3 ± 12.6	40.9 ± 11.3	0.49 ± 0.11	0.52 ± 0.10	2.81 ± 0.57	2.43 ± 0.46

4.3.6 Disclosures

No conflicts of interest, financial or otherwise, are declared by the authors.

4.3.7 Acknowledgments

This work is supported by the TransMedTech Institute, the Discovery Grant program from Natural Sciences and Engineering Research Council of Canada (NSERC) and the Collaborative Health Research Program (CIHR and NSERC). Special thanks are extended to Sylvain Gioux of the University of Strasbourg for his help in the implementation of SFDI-based 3-D profile reconstruction and correction. This work was made possible through open-source software resources offered by the Virtual Photonics Technology Initiative, at the Beckman Laser Institute, University of California, Irvine.

4.3.8 References

1. Center MM, Jemal A, Lortet-Tieulent J, et al. International variation in prostate cancer incidence and mortality rates. *Eur Urol.* 2012;61(6):1079-1092. doi:10.1016/j.eururo.2012.02.054

2. Hsing AW, Tsao L, Devesa SS. International comparisons of prostate cancer incidence and mortality. *Int J Cancer.* 2000;85(July 1999):60-67.

3. Roehrborn CG, Black LK. The economic burden of prostate cancer. *BJU Int.* 2011;108(6):806-813. doi:10.1111/j.1464-410X.2011.10365.x

4. Denmeade SR, Isaacs JT, Denmeade SR, Isaacs JT, Comprehensive K. A history of prostate cancer treatment. 2014;2(5):389-396. doi:10.1038/nrc801.A

5. Makarov D V., Yu JB, Desai RA, Penson DF, Gross CP. The association between diffusion of the surgical robot and radical prostatectomy rates. *Med Care.* 2011;49(4):333-339. doi:10.1097/MLR.0b013e318202adb9

6. Heidenreich A, Bastian PJ, Bellmunt J, et al. EAU guidelines on prostate cancer. Part 1: Screening, diagnosis, and local treatment with curative intent - Update 2013. *Eur Urol.* 2014;65(1):124-137. doi:10.1016/j.eururo.2013.09.046

7. Halpern JA, Shoag JE, Artis AS, et al. National trends in prostate biopsy and radical prostatectomy volumes following the us preventive services task force guidelines against prostate-specific antigen screening. *JAMA Surg.* 2017;152(2):192-198. doi:10.1001/jamasurg.2016.3987

8. Tyson MD, Andrews PE, Ferrigni RF, Humphreys MR, Parker AS, Castle EP. Radical Prostatectomy Trends in the United States: 1998 to 2011. *Mayo Clin Proc.* 2016;91(1):10-16. doi:10.1016/j.mayocp.2015.09.018

9. Grossfeld GD, CHang JJ, Broering JM, et al. Impact of Positive Surgical Margins on Prostate Cancer Recurrence and the Use of Secondary Cancer Treatment: Data From the Capsure Database. *J Urol.* 2000;163(4):1171-1177. doi:10.1016/S0022-5347(05)67716-6

10. Nagtegaal ID, Marijnen CAM, Kranenbarg EK, Van De Velde CJH, Han J, Van Krieken JM. Circumferential Margin Involvement Is Still an Important Predictor of Local Recurrence in Rectal Carcinoma Not One Millimeter but Two Millimeters Is the Limit. *Am J Surg Pathol.* 2002;26(3):350-357. doi:10.1210/endo-125-5-2253

11. Davis BJ, Pisansky TM, Wilson TM, et al. The radial distance of extraprostatic extension of prostate carcinoma: Implications for prostate brachytherapy. *Cancer.* 1999;85(12):2630-2637. https://doi.org/10.1002/(SICI)1097-0142(19990615)85:12<2630::AID-CNCR20>3.0.CO;2-L

12. Nakao A, Takeda S, Sakai M, et al. Extended Radical Resection Versus Standard Resection for. *Pancreas.* 2004;28(3):289-292.

13. Urban C, Rey PC, Gatti G, et al. Comparative Study of Surgical Margins in Oncoplastic Surgery and Quadrantectomy in Breast Cancer. *Ann Surg Oncol.* 2005;12(7):539-545. doi:10.1245/aso.2005.12.046

14. Stummer W, Tonn J-C, Mehdorn HM, et al. Counterbalancing risks and gains from extended resections in malignant glioma surgery: a supplemental analysis from the randomized 5-aminolevulinic acid glioma resection study. *J Neurosurg.* 2010;114(3):613-623. doi:10.3171/2010.3.jns097

15. Holzbeierlein J, Peterson M, Smith JA. Variability of results of cavernous nerve stimulation during radical prostatectomy. *J Urol.* 2001;165(1):108-110. doi:10.1097/00005392-200101000-00027

16. Sanda MG, Dunn RL, Michalski J, et al. Quality of Life and Satisfaction with Outcome among Prostate-Cancer Survivors. *N Engl J Med.* 2008;358(12):1250-1261. doi:10.1056/NEJMoa074311

17. Stanford JL, Hamilton AS, Gilliland FD, et al. After Radical Prostatectomy for Clinically Localized Prostate Cancer The Prostate Cancer Outcomes Study. 2015;1024.

18. Yossepowitch O, Bjartell A, Eastham JA, et al. Positive Surgical Margins in Radical Prostatectomy: Outlining the Problem and Its Long-Term Consequences. *Eur Urol.* 2009;55(1):87-99. doi:10.1016/j.eururo.2008.09.051

19. Blute ML, Bostwick DG, Bergstralh EJ, et al. Anatomic site-specific positive margins in organ-confined prostate cancer and its impact on outcome after radical prostatectomy. *Urology.* 1997;50(5):733-739. doi:10.1016/S0090-4295(97)00450-0

20. Orringer DA, Golby A, Jolesz F. Neuronavigation in the surgical management of brain tumors: Current and future trends. *Expert Rev Med Devices.* 2012;9(5):491-500. doi:10.1586/erd.12.42

21. Ayala G, Tuxhorn JA, Wheeler TM, et al. Reactive Stroma as a Predictor of Biochemical-Free Recurrence in Prostate Cancer. *Clin Cancer Res.* 2003;9(13):4792-4801.

22. Aubertin K, Trinh VQ, Jermyn M, et al. Mesoscopic characterization of prostate cancer using Raman spectroscopy: potential for diagnostics and therapeutics. *BJU Int.* 2018;122(2):326-336.

23. Hu J C, Gu X, Lipsitz S R, et al. Comparative effectiveness of minimally invasive vs open radical prostatectomy. *JAMA - J Am Med Assoc.* 2009;302(14):1557-1564. doi:10.1001/jama.2009.1451

24. Rais-Bahrami S, Levinson AW, Fried NM, et al. Optical Coherence Tomography of Cavernous Nerves: A Step Toward Real-Time Intraoperative Imaging During Nerve-Sparing Radical Prostatectomy. *Urology.* 2008;72(1):198-204. doi:10.1016/j.urology. 2007.11.084

25. Crow P, Stone N, Kendall CA, et al. The use of Raman spectroscopy to identify and grade prostatic adenocarcinoma in vitro. *Br J Cancer.* 2003;89(1):106-108. doi:10.1038 /sj.bjc.6601059

26. A'Amar OM, Liou L, Rodriguez-Diaz E, De Las Morenas A, Bigio IJ. Comparison of elastic scattering spectroscopy with histology in ex vivo prostate glands: Potential application for optically guided biopsy and directed treatment. *Lasers Med Sci.* 2013;28(5):1323-1329. doi:10.1007/s10103-012-1245-6

27. Zaak D, Sroka R, Khoder W, et al. Photodynamic Diagnosis of Prostate Cancer Using 5-Aminolevulinic Acid—First Clinical Experiences. *Urology.* 2008;72(2):345-348. doi:10.1016/j.urology .2007.12.086

28. Ebenezar J, Pu Y, Wang W, Yang Y, Alfano RR. Stokes shift spectroscopy pilot study for cancerous and normal prostate tissues. *Opt Lett.* 2012;37(16):3360. doi:10.1364/OL.37.003360

29. Marriott G, Clegg RM, Arndt-Jovin DJ, Jovin TM. Time resolved imaging microscopy. Phosphorescence and delayed fluorescence imaging. *Biophys J.* 1991;60(6):1374-1387. doi:10.1016/S0006-3495(91)82175-0

30. Koenig K, Schneckenburger H. Laser-induced autofluorescence for medical diagnosis. *J Fluoresc.* 1994;4(1):17-40. doi:10.1007/BF01876650

31. Li LZ. Imaging mitochondrial redox potential and its possible link to tumor metastatic potential. *J Bioenerg Biomembr.* 2012;44(6):645-653. doi:10.1007/s10863-012-9469-5

32. Masilamani V, Al-Zhrani K, Al-Salhi M, Al-Diab A, Al-Ageily M. Cancer diagnosis by autofluorescence of blood components. *J Lumin.* 2004;109(3-4):143-154. doi:10.1016/j.jlumin.2004.02.001

33. Wagnieres GA, Star WM, Wilson BC. ln Vivo Fluorescence Spectroscopy and lmaging for Oncological Applications of Technology. *Photochemistry.* 1998;68(5):603-632.

34. Pu Y, Wang W, Yang Y, Alfano RR. Stokes shift spectroscopic analysis of multifluorophores for human cancer detection in breast and prostate tissues. *J Biomed Opt.* 2013;18(1):017005-1-017005-017008. doi:10.1117/1.JBO.18.1.017005

35. Haringsma J, Tytgat GNJ. Fluorescence and autofluorescence. *Bailliere's Best Pract Res Clin Gastroenterol.* 1999;13(1):1-10. doi:10.1053/bega.1999.0003

36. Kluftinger AM, Davis NL, Quenville NF, Lam S, Hung J, Palcic B. Detection of squamous cell cancer and pre-cancerous lesions by imaging of tissue autofluorescence in the hamster cheek pouch model. *Surg Oncol.* 1992;1(2):183-188. doi:10.1016/0960-7404(92)90032-g

37. Richards-Kortum R, Sevick-Muraca E. Quantitative Optical Spectroscopy for Tissue Diagnosis. *Annu Rev Phys Chem.* 1996;47(1):555-606. doi:10.1146/annurev.physchem.47.1.555

38. Patterson MS, Pogue BW. Mathematical model for time-resolved and frequency-domain fluorescence spectroscopy in biological tissues. *Appl Opt.* 1994;33(10):1963-1974. doi:10.1121 /1.2177570

39. Vishwanath K, Pogue B, Mycek MA. Quantitative fluorescence lifetime spectroscopy in turbid media: Comparison of theoretical, experimental and computational methods. *Phys Med Biol*. 2002;47(18):3387-3405. doi:10.1088/0031-9155/47/18/308

40. Pogue BW, Burke G. Fiber-optic bundle design for quantitative fluorescence measurement from tissue. *Appl Opt*. 1998;37(31):7429-7436. doi:10.1364/AO.37.007429

41. Flusberg BA, Cocker ED, Piyawattanametha W, et al. Fiber-optic fluorescence imaging. *Nat Methods*. 2005;2(12):941-950. doi:10.1038/nmeth820.Fiber-optic

42. Leblond F, Davis SC, Valdés PA, Pogue BW. Pre-clinical whole-body fluorescence imaging: Review of instruments, methods and applications. *J Photochem Photobiol B Biol*. 2010;98(1):77-94. doi:10.1016/j.jphotobiol.2009.11.007

43. Bradley RS, Thorniley MS. A review of attenuation correction techniques for tissue fluorescence. *J R Soc Interface*. 2006;3(6):1-13. doi:10.1098/rsif.2005.0066

44. Wu J, Feld MS, Rava RP. Analytical model for extracting intrinsic fluorescence in turbid media. *Appl Opt*. 1993;32(19):3585. doi:10.1364/AO.32.003585

45. Zhang Q, Muller M, Wu J, Feld M. Turbidity-free fluorescence spectroscopy of biological tissue. *Opt Lett*. 2000;25(19):1451-1453. doi:62200 [pii]

46. Gardner CM, Jacques SL, Welch AJ. Fluorescence spectroscopy of tissue: recovery of intrinsic fluorescence from measured fluorescence. *Appl Opt*. 1996;35(10):1780. doi:10.1364/AO.35.001780

47. Yang B, Sharma M, Tunnell JW. Attenuation-corrected fluorescence extraction for image-guided surgery in spatial frequency domain. *J Biomed Opt*. 2013;18(8):080503. doi:10.1117/1.JBO.18.8.080503

48. Saager RB, Cuccia DJ, Saggese S, Kelly KM, Durkin AJ. Quantitative fluorescence imaging of protoporphyrin IX through determination of tissue optical properties in the spatial frequency domain. *J Biomed Opt*. 2011;16(12):126013. doi:10.1117/1.3665440

49. Sunar U, Rohrbach DJ, Morgan J, Zeitouni N, Henderson BW. Quantification of PpIX concentration in basal cell carcinoma and squamous cell carcinoma models using spatial frequency domain imaging. *Biomed Opt Express*. 2013;4(4):531. doi:10.1364/BOE.4.000531

50. Sibai M, Veilleux I, Elliott JT, Leblond F, Wilson BC. Quantitative spatial frequency fluorescence imaging in the sub-diffusive domain for image-guided glioma resection. *Biomed Opt Express*. 2015;6(12):4923. doi:10.1364/BOE.6.004923

51. Valdés PA, Roberts DW, Lu F, Golby A. Optical technologies for intraoperative neurosurgical guidance. *Neurosurg Focus*. 2016;40(March):1-18. doi:10.3171/2015.12. FOCUS15550.

52. Kress J, Rohrbach DJ, Carter KA, et al. A dual-channel endoscope for quantitative imaging, monitoring, and triggering of doxorubicin release from liposomes in living mice. *Sci Rep*. 2017;7(1):1-13. doi:10.1038/s41598-017-15790-y

53. Valdés PA, Angelo JP, Choi HS, Gioux S. qF-SSOP: real-time optical property corrected fluorescence imaging. *Biomed Opt Express*. 2017;8(8):3597. doi:10.1364/BOE.8.003597

54. Ramanujam N. Fluorescence Spectroscopy of Neoplastic and Non-Neoplastic Tissues. *Neoplasia*. 2000;2(1-2):89-117. doi:10.1038/sj.neo.7900077

55. Cuccia DJ, Bevilacqua F, Durkin AJ, Ayers FR, Tromberg BJ. Quantitation and mapping of tissue optical properties using modulated imaging. *J Biomed Opt*. 2009;14(2): 024012. doi:10.1117/1.3088140

56. Bodenschatz N, Krauter P, Liemert A, Wiest J, Kienle A. Model-based analysis on the influence of spatial frequency selection in spatial frequency domain imaging. *Appl Opt*. 2015;54(22):6725. doi:10.1364/ao.54.006725

57. Angelo JP, Chen S-J, Ochoa M, et al. Review of structured light in diffuse optical imaging. *J Biomed Opt*. 2018;24(07):1. doi:10.1117/1.JBO.24.7.071602

58. Bodenschatz N, Brandes A, Liemert A, Kienle A. Sources of errors in spatial frequency domain imaging of scattering media. *J Biomed Opt*. 2014;19(7):071405. doi:10.1117/1.JBO.19.7.071405

59. Gioux S, Mazhar A, Cuccia DJ, Durkin AJ, Tromberg BJ, Frangioni J V. Three-dimensional surface profile intensity correction for spatially modulated imaging. *J Biomed Opt*. 2009;14(3):034045. doi: 10.1117/1.3156840

60. Angulo-rodriguez L, Badawy Y, Leblond F. Development and Validation of Phase-Shifting Profilometry Using a Hyperspectral Spatial Frequency Domain Imaging System Integrated with a Neurosurgical Microscope. *J Bioeng Biomed Sci*. 2019;9(1):1000257. doi:10.4172/2155-9538.1000257

61. Kim A, Moriyama Y, Wilson BC. Quantification of in vivo fluorescence decoupled from the effects of tissue optical properties using fiber-optic spectroscopy measurements. *J Biomed Opt.* 2010;15(December 2010):1-12. doi:10.1117/1.3523616

62. Jacques SL. Optical properties of biological tissues: A review. *Phys Med Biol.* 2013;58(11). doi:10.1088/0031-9155/58/11/R37

63. Grabtchak S, Montgomery LG, Whelan WM. Feasibility of interstitial near-infrared radiance spectroscopy platform for ex vivo canine prostate studies: optical properties extraction, hemoglobin and water concentration, and gold nanoparticles detection . *J Biomed Opt.* 2014;19(5):057003. doi:10.1117/1.jbo.19.5.057003

64. Lee W, Khoo B. Forensic light sources for detection of biological evidences in crime scene investigation: a review. *Malaysian J Forensic Sci.* 2010;1(1):17-27.

65. Sandell JL, Zhu TC. A review of in-vivo optical properties of human tissues and its impact on PDT. *J Biophotonics.* 2011;4(11-12):773-787. doi:10.1002/jbio.201100062

66. Valdés PA, Kim A, Leblond F, et al. Combined fluorescence and reflectance spectroscopy for in vivo quantification of cancer biomarkers in low- and high-grade glioma surgery. *J Biomed Opt.* 2011;16(11):116007. doi:10.1117/1.3646916

67. Phantoms T, Ninni P Di, Martelli F, Zaccanti G. Intralipid: Towards a diffusive reference standard for optical. *Phys Med Biol.* 2011;56(2). doi:10.1088/0031-9155/56/2/N01

68. Spinelli L, Botwicz M, Zolek N, et al. Determination of reference values for optical properties of liquid phantoms based on Intralipid and India ink. *Biomed Opt Express.* 2014;5(7):2037. doi:10.1364/BOE.5.002037

69. Erickson TA, Mazhar A, Cuccia D, Durkin AJ, Tunnell JW. Lookup-table method for imaging optical properties with structured illumination beyond the diffusion theory regime. *J Biomed Opt.* 2010;15(3):036013. doi:10.1117/1.3431728

70. Oraevsky AA, Jacques SL, Tittel FK. Measurement of tissue optical properties by time-resolved detection of laser-induced transient stress. *Appl Opt.* 1997;36(1):402. doi:10.1364/ao.36.000402

71. Svensson T, Andersson-engels S. In vivo optical characterization of human prostate tissue using near-infrared time-resolved spectroscopy. *J Biomed Opt.* 2007;12(1):014022. doi:10.1117/1.2435175

72. Piao D, Bartels KE, Jiang Z, et al. Alternative transrectal prostate imaging: A diffuse optical tomography method. *IEEE J Sel Top Quantum Electron.* 2010;16(4):715-729. doi:10.1109/JSTQE.2009.2034026

73. Pogue BW, Patterson MS. Review of tissue simulating phantoms for optical spectroscopy, imaging and dosimetry. *J Biomed Opt.* 2006;11(4):041102. doi:10.1117/1.2335429

74. Hayakawa CK, Karrobi K, Pera V, Roblyer D, Venugopalan V. Optical sampling depth in the spatial frequency domain. *J Biomed Opt.* 2018;24(07):1. doi:10.1117/1.jbo.24.7.071603

75. Sibai M, Veilleux I, Elliott JT, Leblond F, Roberts DW, Wilson BC. Quantitative fluorescence imaging enabled by spatial frequency domain optical-property mapping in the sub-diffusive regime for surgical guidance. *Proc SPIE.* 2015;9311:93110C. doi:10.1117/12.2080205

76. Tabassum S, Zhao Y, Istfan R, Wu J, Waxman DJ, Roblyer D. Feasibility of spatial frequency domain imaging (SFDI) for optically characterizing a preclinical oncology model. *Biomed Opt Express.* 2016;7(10):4154. doi:10.1364/boe.7.004154

77. Weber JR, Cuccia DJ, Johnson WR, et al. Multispectral imaging of tissue absorption and scattering using spatial frequency domain imaging and a computed-tomography imaging spectrometer. *J Biomed Opt.* 2011;16(1):011015. doi:10.1117/1.3528628

78. Laughney AM, Krishnaswamy V, Rice TB, et al. System analysis of spatial frequency domain imaging for quantitative mapping of surgically resected breast tissues. *J Biomed Opt.* 2013;18(3):036012. doi:10.1117/1.JBO.18.3.036012

79. Kanick SC, Krishnaswamy V, Gamm UA, et al. Scattering phase function spectrum makes reflectance spectrum measured from Intralipid phantoms and tissue sensitive to the device detection geometry. *Biomed Opt Express.* 2012;3(5):1086. doi:10.1364/boe.3.001086

80. St-Georges-Robillard A, Masse M, Cahuzac M, et al. Fluorescence hyperspectral imaging for live monitoring of multiple spheroids in microfluidic chips. *Analyst.* 2018;143(16):3829-3840. doi:10.1039/c8an00536b

81. Valdés PA, Leblond F, Kim A, Wilson BC, Paulsen KD, Roberts DW. A spectrally constrained dual-band normalization technique for protoporphyrin IX quantification in fluorescence-guided surgery. *Opt Lett.* 2012;37(11):1817. doi:10.1364/OL.37.001817

82. Pu Y, Wang W, Tang G, Alfano RR. Changes of collagen and nicotinamide adenine dinucleotide in human cancerous and normal prostate tissues studied using native fluorescence spectroscopy with selective excitation wavelength. *J Biomed Opt.* 2010;15(4):047008. doi:10.1117/1.3463479

83. Alfano RR, Wahl SJ, Pradhan A, Tang GC. Optical spectroscopic diagnosis of cancer and normal breast tissues. *J Opt Soc Am B.* 1989;6(5):1015. doi:10.1364/ JOSAB.6.001015

CHAPTER 5 COMPLEMENTARY RESULTS

The goal of this chapter is to present supplementary results that were not showcased in the article. These include the detailed testing of multiple fluorescence quantification algorithms on both optical phantoms and a prostate specimens, results of SFDI reconstructions on multiple prostate samples, as well as an analysis of benign *vs* malign prostatic tissue differentiation.

5.1 Fluorescence quantification algorithms

As presented in section 2.3, there are multiple approaches to fluorescence quantification. Additionally to the initial selection in section 6.2.1, three quantification methods were experimentally compared to choose the quantification approach for prostate samples:

1. The simple ratio technique (Eq. 2.8) ,
2. The α weighted ratio technique (Eq. 2.9) ,
3. The optical property-based correction of Kim *et al.* (Eq. 2.15).

The same experimental method was used as in section 4.3.2.4; 9 optical phantoms with 3 set of optical properties (μ_a = 0.05, 0.15, 0.25; μ_s' = 0.75, 1.15, 1.5) for 3 PpIX concentrations (1.25, 2.5, 5 μg/ml) were measured with each modality. The emission spectra were computed according to the standard process shown in figure 4.2. The results of these fluorescence quantification tests on phantoms are summarized in figure 5.1.

For the simple ratio correction, a $R^2 = 0.51$ was noted compared to $R^2 = 0.42$ uncorrected results. The change was not significant and major differences between intensities were still be observed. The α correction yielded a marked improvement with $R^2 = 0.87$, yet the method also increased the standard deviation of the intensity values. This was probably due to the fact the high exponential α factor amplified the initial variation present in the reflectance images used. Finally, the optical properties correction led to $R^2 = 0.83$ while maintaining a standard deviation similar to that of the uncorrected data. To test the techniques in a biological context, the same 3 quantification methods were applied to a prostate sample. Visual assessment of the resulting images was made to ascertain if the correction methods resulted in less correlation with other modalities (reflectance R, absorption μ_a, reduced scattering μ_s') or tissue height variations than raw fluorescence F_{raw}. Figure 5.2 shows all relevant results for the comparison of fluorescence quantification methods on prostate samples.

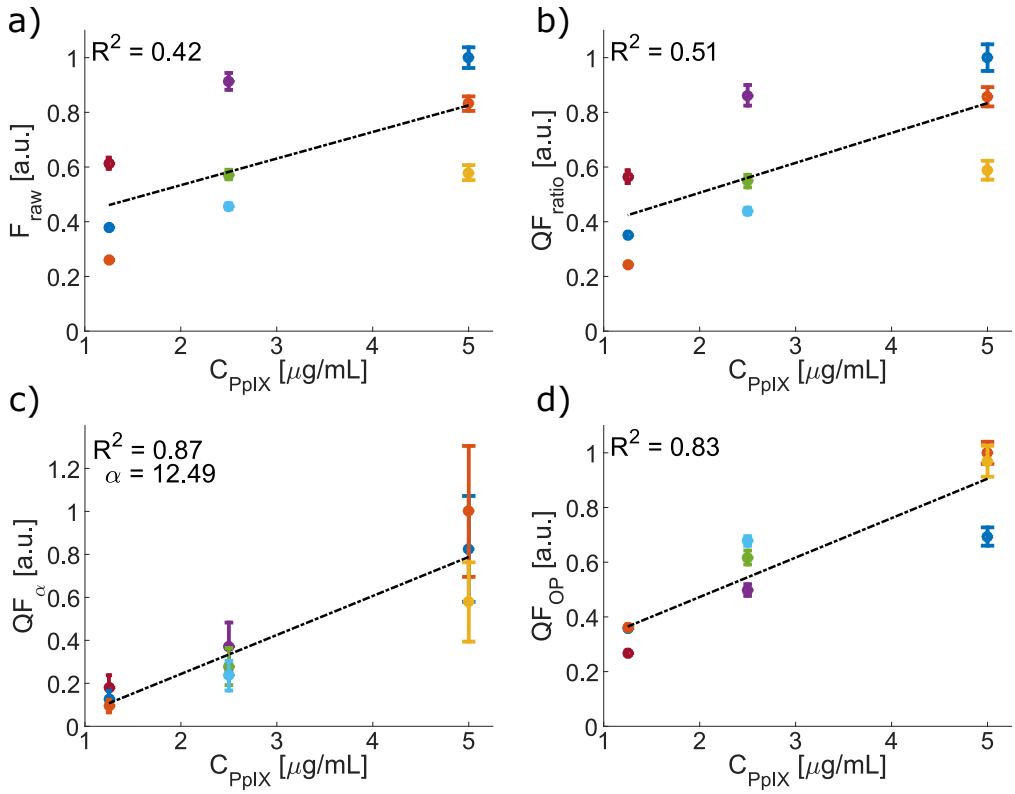

Figure 5.1 (a) Average PpIX fluorescence emission peak intensity obtained with the multimodal imaging system on optical phantoms with varied absorption and scattering properties. Dataset is quantified using (b) the simple ratio technique, (c) the weighted ratio method and (d) SFDI obtained optical properties.

The simple ratio method reduced some of the correlations with the reflectance measurement, but features of both reflectance and μ_s', such as near the top and bottom of the prostate, were still seen after the correction. The α weighted ratio yielded poor results, greatly increasing the scale due to the high exponential value used, as far as to make the image hard to visualize without a logarithmic scale. We concluded that the technique was ill-adapted to the current wide-field imaging system. With the model-based correction, quantified fluorescence did not present any obvious correlations to other modalities or sample height. Most notably, the method significantly reduced the effect of the central urethra depression and the high μ_s' region near the bottom of the sample. In both phantom and biological sample tests, the model-based correction by Kim *et al.* yielded the most satisfactory results, which justified its use for the system.

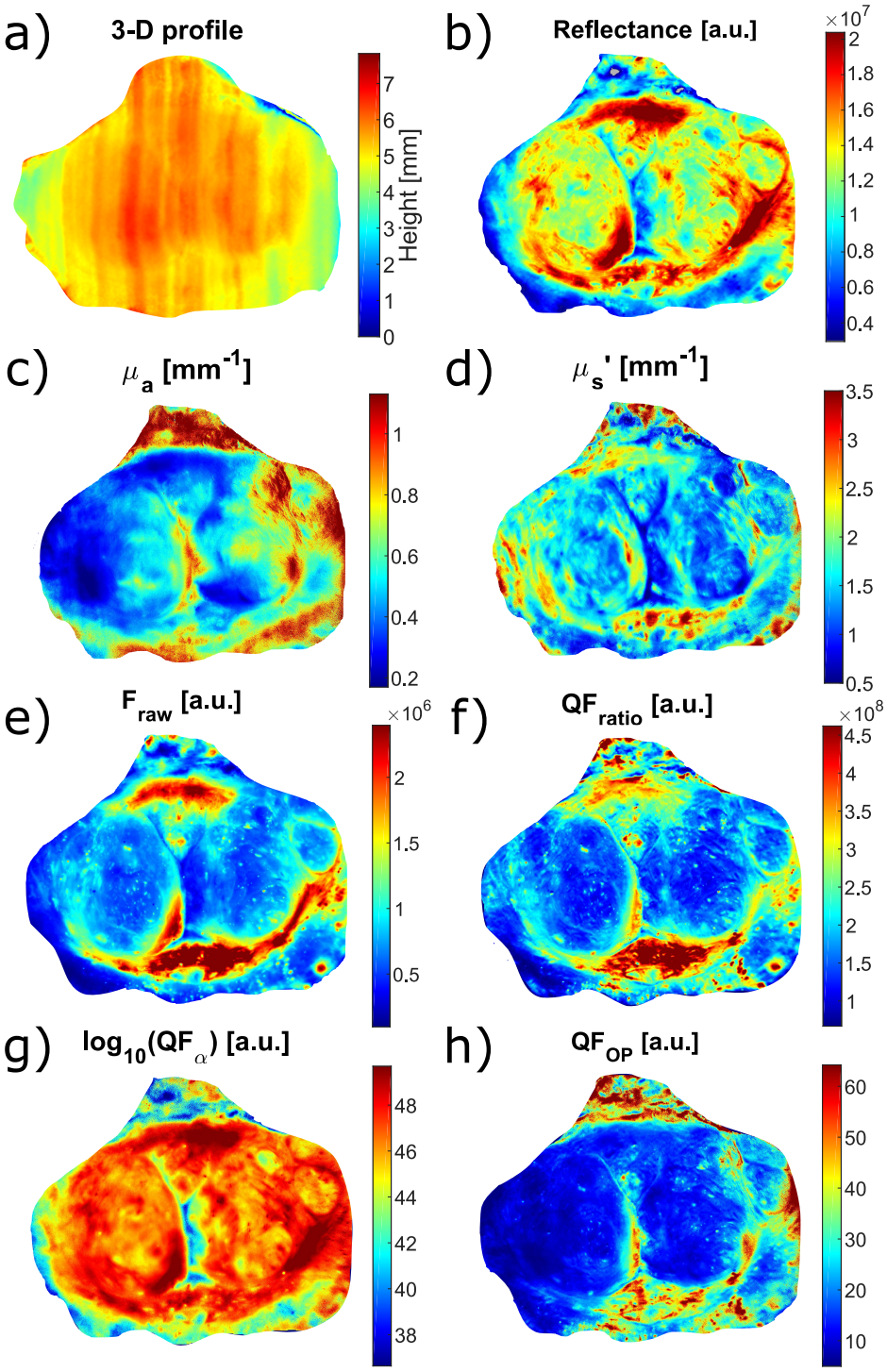

Figure 5.2 (a) Reconstructed height profile of the sample along with modalities measured by the imaging system: (b) reflectance, (c) absorption coefficient, (d) scattering coefficient and (e) fluorescence. These images are compared to the subsequent results of data processing with various fluorescence quantification techniques; (f) simple ratio, (g) weighted ratio method and (h) optical properties method.

5.2 Prostate optical properties

Several prostates were imaged before the implementation of the profilometry algorithm for SFDI. These results were excluded from the article but are still relevant to get an idea of tissue properties across multiple samples. The absorption and reduced scattering coefficients without geometrical corrections of four prostates, all using the same reference phantom, are shown in table 5.1. Prostate #4 was used in the article. Note that these biomarkers were not directly compared to histopathological gold standards outside of the analysis of prostate regions in the article since they offer no specific informations on tissue structure or chromphore presence. Since results for reflectance, fluorescence, and quantified fluorescence vary with polarisation, as explained in section 6.2.3.2, these results are not shown here. The SFDI data prior to the height correction remains valid in part because the impact of the profile correction on radical prostatectomy specimens was observed to be low on the mean values of absorption and reduced scattering coefficients, as seen in Fig. 4.11.

Table 5.1 Average and standard deviation of absorption and reduced scattering coefficients from multiple prostate samples analyzed with the multimodal spectroscopic imaging system without sample geometry corrections

Prostate #	μ_a [mm^{-1}]	μ_s' [mm^{-1}]
1	0.62 ± 0.31	1.48 ± 0.46
2	0.65 ± 0.30	1.57 ± 0.45
3	0.31 ± 0.13	1.93 ± 0.53
4	0.52 ± 0.19	1.71 ± 0.52

Average optical properties were consistent throughout the experiments, as all individual averages were within the standard deviation range of the other prostates, except absorption in prostate 3. Prostate 3 was very large due to a high degree of hyperplasia and, as Fig.4.8 showed, hyperplasic tissue has lower absorption values. This may explain the difference in the absorption average but should be investigated with additional highly hyperplasic prostates. Total values ranged from μ_a = 0.18-0.94 mm^{-1} and from μ_s' = 1.02-2.46. This data may be used to further adapt SFDI acquisition and processing to the prostate application.

5.3 Cancerous tissue differentiation

Histopathological gold standards were obtained for the imaged radical prostatectomy specimens. These HE stainings were compared to the reference photograph of the prostate sample to co-register information such as prostate regions, glandular tissue, benign hyperplasia or

cancerous tissue. An example of the gold standard referencing method is presented in figure 5.3.

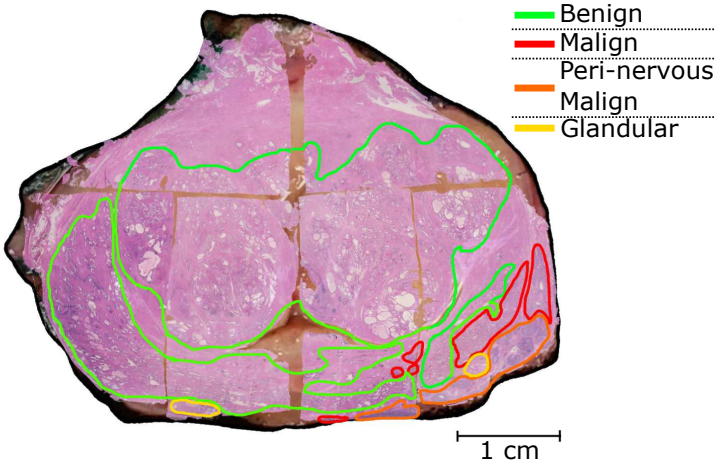

Figure 5.3 Prostate sample photograph superimposed with HE staining, allowing the correlation of measurements with benign tissue, malign and peri-nervous malign tissue, as well as glandular tissue.

Due to logistical limitations involving the delay to obtain the stainings, it was not possible to present a comparison between benign and malign tissue in the article. Although it should again be mentioned that the number of samples is too small to conduct a proper statistical analysis, observations on the benign *vs* malign regions were made some time after the submission of the paper following the same methodology as the results shown in section 4.3.3.4. The subregions used and average modalities spectra are identified in figure 5.4. Figure 5.5 presents boxplot comparisons of all the regions for μ_a, μ_s' and quantified fluorescence.

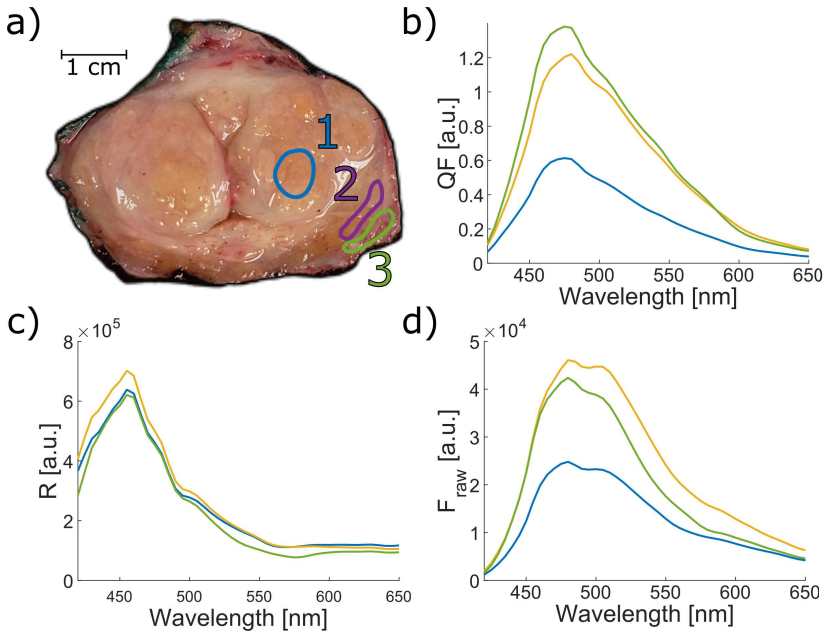

Figure 5.4 (a) Photograph of the prostate specimen with biologically distinct regions identified by a pathologist: 1) benign glands, 2) malign tissue, 3) peri-nervous malign tissue. Average spectra computed for each region of interest: (b) quantified fluorescence (QF), (c) reflectance and (d) raw fluorescence. No legend is provided for the spectra but the colors for the contour delineations in (a) match those of their associated spectra in (b), (c) and (d).

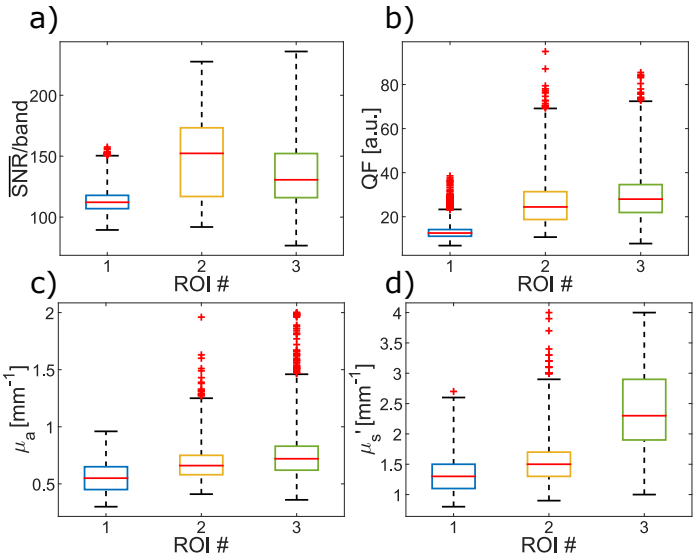

Figure 5.5 Boxplots comparing (a) the SNR per spectral band, (b) the quantified fluorescence (QF), (c) the absorption coefficient and (d) the reduced scattering coefficient of all prostate regions of interest (ROI): 1) benign glands, 2) malign tissue, 3) peri-nervous malign tissue.

The average spectra of the different regions showed that, although reflectance was similar for all regions, the two malign regions presented significant differences from the benign region in fluorescence and QF. Both malign regions also presented respective differences in these modalities. For preliminary statistical analyses, Kruskal-Wallis tests computed that all comparisons between regions showed statistically significant potential for differentiation ($p<0.01$) for all modalities. However, all three regions presented differences in median and IQR for SNR. For QF, differences in median and IQR were noted between both types of malign tissue and benign glands, but the two cancerous tissue types were very similar in distribution. For absorption, the same was observed as for QF, but with more significant differences in the maximum-minimum range for the malign and peri-nervous malign tissue. For scattering, a marked difference was observed between the two malign tissue type's median and IQR, while both malign tissues retained a higher median than benign tissue. This is particularly interesting in a biological context since peri-nervous malign tissue grows from nerves surrounding the prostate and thus should have a structure more similar to nervous tissue rather than prostate tissue. Since μ_s' is an indicator of tissue structure, it seems consequent that malign and peri-nervous malign are siginificantly different for that biomarker. These observations on benign *vs* malign tissue led to similar conclusions as the ones for prostatic *vs* extra-prostatic tissue, which is that the acquired biomarkers present potential to be used for differentiation. This lent further credence to the system and the validation of hypothesis 2.

CHAPTER 6 GENERAL DISCUSSION

This chapter focuses on methodological details regarding the system's conception and discussion of the final results. Tasks detailed here are the optical conception of the system, elaboration of the optimized acquisition process, mathematical justification of the calibration process and, finally, limitations of the imaging system in the surgical context.

6.1 Optical system design

6.1.1 System performance goals

The initial step of the project was to conceive the measurement system. First, some performance goals were set, appropriate to the application on radical prostatectomy specimens. By referencing images of prostate slices obtained from 41 patients of another study which is using the same sample acquisition protocol as the current study (data provided by post-doctoral student Kelly Aubertin), the average largest dimension of a sample was determined to be 4.5 cm with a STD of 0.8 cm. To cover a majority of prostates, the FOV objective was set to 5.25 x 5.25 cm. Although there were no specific restrictions regarding distance to the sample for the bench-top system, a potential *in vivo* PCa context was considered to be the use in a *DaVinci* robotic surgery system. Since this type of surgery takes place inside the abdominal cavity, a working distance of 10 cm was set as a target. A spatial resolution target of under 500 μm was also set considering this surgical context. Although acquisition time was not considered since the goal of the system was a proof-of-concept, a maximum of 30 minutes for a complete multimodal acquisition had to be respected due to the sample acquisition process. The final system specifications, as introduced in section 4.3.3.1, are summarized in table 6.1.

Table 6.1 Multimodal spectroscopic imaging system specifications.

Specification	System performance
Field of view	5.5 x 5.5 cm
Spatial frequency resolution	0.9 mm^{-1}
Resolution	70 μm
Depth of field	1.5 cm
Working distance	10 cm
Total acquisition time	12.4 min

Target performance goals were reached with the final system. In the following subsections, the design process is presented in two branches, which are the excitation of the sample of the

detection of the signal.

6.1.2 Excitation

6.1.2.1 Source selection

Different requirements were set for the excitation source in regards to the imaging modalities needed. By considering the various methods of fluorescence quantification, presented in section 2.3.3, the main measurements needs were established:

1. Broadband reflectance measurement ;
2. Optical properties (SFDI measurement) at fluorescence excitation wavelength ;
3. Fluorescence measurement.

It was determined that at least two sources were needed; a white-light source, for reflectance, and a source for fluorescence/SFDI excitation. Referring to table 2.1 and other endogenous fluorescence systems in literature, it was decided to use a source around 400 nm to excite endogenous fluorescence for the prostate application. While there would be a higher number of fluorophores excited by using a source in the deeper UV range, 400 nm excitation did not require the use of specialized UV optics. Moreover, no SFDI projector systems compatible with deep UV were found on the market, meaning UV excitation would also incur the design of a complete projection system. Considering the time scope of the project, this would not be possible.

With these considerations, the Spectra X light engine (Lumencor, OR, USA) was chosen as the source for the system. The Spectra X contained seven Light-Emitting Diode (LED)s with peak powers at 405, 435, 475, 515, 550, 570 and 630 nm which could all be controlled individually, save for the sources at 550 and 570 nm. The source also contained internal bandpass filters that narrowed the output of each LED. The complete spectral range of the source, both with and without filters, is presented in figure 6.1. The measurements were taken on a Maya2000 spectrometer (Ocean Optics, FL, USA).

The first LED, with a power of 205 mW peaking at 405 nm, was used to excite fluorescence. For the SFDI measurement, the second LED with a power peak of 290 mW at 435 nm was used due to low system transmission at 405 nm, as explained in section 6.1.3. For reflectance, all LEDs save for the one at 405 nm were used simultaneously. The internal filters from these LEDs were also removed. The resulting white-light source outputted from 420-650 nm with a total power of 1720 mW. In all cases, the source was outputted through a single 3 mm

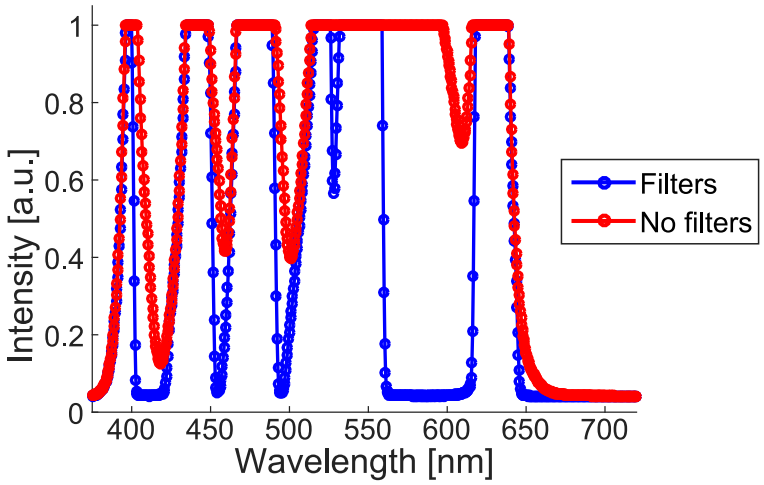

Figure 6.1 Spectral range of the multimodal imaging system's source (Spectra X) with and without internal filter. The figure is not indicative of spectral shape due to detector saturation.

Liquid Light Guide (LLG). The LLG was connected to a collimator with SM1 threading, which allowed connection to the optical system, fine adjustment of the direction and focus of the light output, and a suitable projection area on the sample. The total spectral range of interest for projection was from 400 to 650 nm.

6.1.2.2 SFDI projection

DLP systems control light projection patterns with an array of micro-mirrors integrated on a CMOS chip, forming a Digital Micromirror Device chip (Texas Instruments, TX, USA). These mirrors can be individually controlled to reflect light in two distinct directions; in the projection path or off the projection path. Grayscale intensities are achieved by switching between the two positions rapidly.

For the SFDI projection, a ready-made DLP system, the CEL5500 (Digital light innovations, TX, USA), was used. The model was compatible with wavelengths 400-700 nm, which included the 400-650 nm spectral range of interest. The 0.55" chip with 100 μm^2 micromirrors also provided a satisfactory pattern resolution of ~50 μm for a projection over a 5.25 x 5.25 cm FOV. Switching time between configurations was deemed negligible due to the high acquisition time limit. The base of this DLP system was modified by doctoral student Leticia Angulo to fit into the ocular of a surgical microscope, as required for a different project, by adding a relay lens fixed to the projector. This lens was not appropriate to get the desired FOV for prostate samples and was not interchangeable. After *Optical Studio* (Zemax, WA,

USA) tests, a bi-concave lens f = -25 mm (32-993, Edmund Optics, NJ, USA) was added to get the desired projection area.

The collimated source output was connected directly to the CEL5500. By using an optical power-meter (S121C, Thorlabs, NJ, USA) a power of 34.48 mW was measured at the exit of the collimator compared to 1.560 mW at the exit of the projector set-up, representing a transmittance of 4.52%. These significant losses may be explained by factors such as the illumination area on the micromirror chip, its fill factor and reflectivity, the use of a total internal reflection prism, and the mismatch caused by the choice of relay lens. Figure 6.2 presents a summary of the transmission factors of these various elements, obtained through manufacturer specifications. Although other factors were obtained through documentation, transmission through the final relay lens was estimated to be of ~34% with the experimental results.

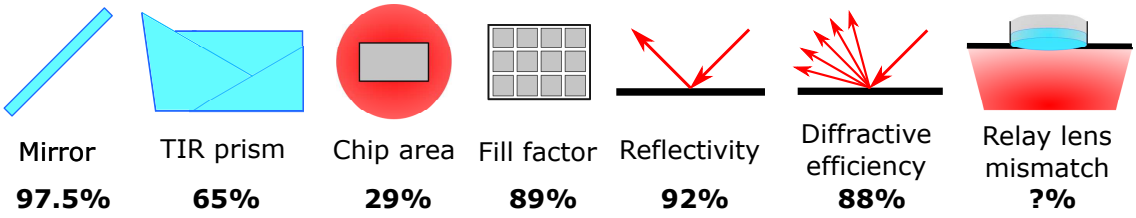

Figure 6.2 Transmission of elements in the digital light processor used for the multimodal imaging system.

6.1.2.3 Fluorescence/reflectance projection

Due to the important losses in the SFDI projector, the choice was made to build a separate projection branch for fluorescence and reflectance. The fluorescence/reflectance illumination was the direct output of the collimator, which was placed at a suitable distance to cover the desired FOV. For fluorescence, one point of concern was to avoid source bleedthrough in the measurements, as endogenous fluorescence signal was expected to be low. Figure 6.3, acquired with the Maya spectrometer, highlights the spectral range of the fluorescence source. It can be seen power is measured at over 475 nm, well beyond the 405 nm peak. Therefore, two 390 ± 40 bandpass filters with optical densities >7 (Semrock, NY, USA) were added on an optical railing after the source, which ensured the source intensity was negligible at wavelengths >418 nm. This cut-off point led to the choice of the 420-650 nm acquisition range for fluorescence and reflectance. These filters could be quickly placed out of the illumination path for reflectance measurements.

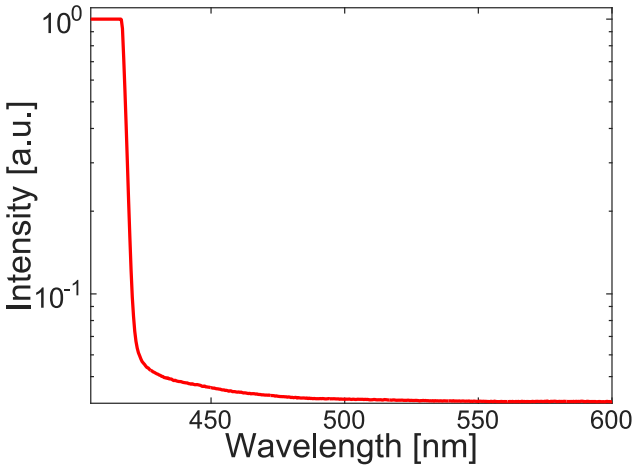

Figure 6.3 Emission spectrum of the fluorescence excitation source (Spectra X, 405 nm LED) used for the multimodal imaging system with a highlight on full spectral range.

6.1.3 Detection

6.1.3.1 Imaging detector

The detector used was an Orca Flash sCMOS camera (CC11440-22CU, Hamamatsu, Shizuoka, Japan), with a 2048 x 2048 pixel 4/3" array, 6.5 x 6.5 μm pixel size and low readout noise (0.8e median). The large array size provided an increased signal, the pixel size offered resolution lower than the 500 μm target and the low readout noise allowed for the long integration times required for sufficient SNR. An imaging objective (LM25XC, Kowa, CA, USA) suitable to 4/3" sensors was chosen with f = 25 mm, providing the desired FOV at a suitable working distance of 10 cm.

6.1.3.2 Hyperspectral imaging technology

To enable hyperspectral acquisitions, a Liquid Crystal Tunable Filter (LCTF) was integrated into the optical detection path between the camera and the imaging objective. Although a LCTF is less performant than a spectrometer, it was more suitable for a wide-field system where low bandwidth isn't necessary. Its usage also simplified the optical design and removed the need for alignment. The LCTF used was the Varispec VIS (CRI, MA, USA), with a spectral range from 400 to 720nm; covering the whole spectrum of interest. Although its spectral resolution of 7 nm (full-width at half maximum) is large, it was sufficient for the application as endogenous fluorescence does not feature slim emission peaks. The 50 ms change time between wavelengths was not a current concern since integration times were

expected to be lengthy (>1 s) due to low signal. Since the light entering the LCTF must be collimated to reduce losses, two objectives (Fotasy M3517,f = 35 mm) set at infinity were added on either side of the component by doctoral student Leticia Angulo for a previous project. Although these objectives were compatible with the system's 4/3" sensor, they were not ideally suited for the detection system, which caused some vignetting and lowered detected intensity. A caveat of the LCTF, however, was its transmission spectrum; shown in figure 6.4 as provided by the manufacturer. A marked dip in performance closer to the UV region was noticed.

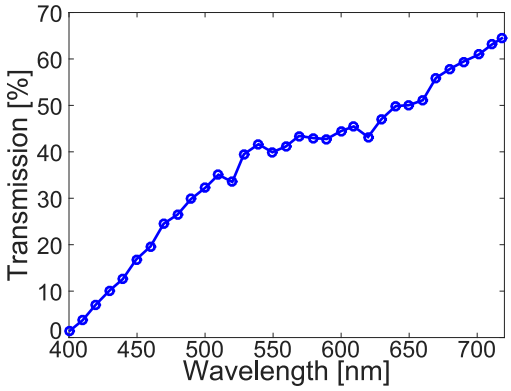

Figure 6.4 Transmission of the Varispec VIS liquid crystal tunable filter dependent on wavelength.

Total detection system transmission, obtained with the measurement of a spectral irradiance standard (63355, Newport, CA, USA), is illustrated in figure 6.5. This curve was used in the calibration process of the data.

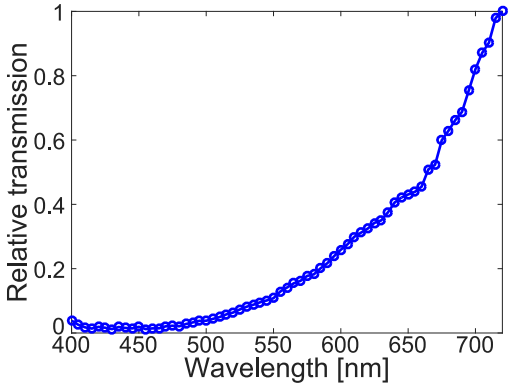

Figure 6.5 Relative transmission of the multimodal imaging system dependent on wavelength.

6.2 Acquisition process

To successfully make an acquisition, a variety of instruments needed to be controlled and synchronized:

1. Camera - control parameters, snapshot imaging, and data saving ;
2. LCTF - vary wavelength during hyperspectral acquisition ;
3. Source - Switch between different LEDs for each modality ;
4. DLP - Adjust projection frequencies and phases for SFDI.

Acquisition control was streamlined through a Labview (National Instruments, TX, USA) software. The software allowed measurement of each modality, using optimized acquisition parameters, with a single button press, and also had an option to acquire calibration data, such as dark counts. All acquisition results were saved with fixed names in labeled folders. The interface allowed snapshot images with controllable exposure time, excitation source and LCTF wavelength to simplify hardware adjustments. The visual interface of the software is presented in appendix A. However, the user had to switch the collimator between the SFDI projection and fluorescence/reflectance branches manually, and also move the filters manually between fluorescence and reflectance acquisitions. The specific optimization of parameters for each modality is presented in the subsequent subsections.

6.2.1 Spatial frequency domain imaging acquisition

There were three elements to consider for the SFDI acquisition:

1. Number and selection of spatial frequencies ;
2. Number of phases ;
3. Acquisition wavelengths.

For SFDI, the spatial frequencies used have a significant impact on the accuracy of the results. Using more frequencies results in a more accurate reflectance curve and thus reduces absorption/scattering reconstruction errors. However, in a practical context, it is not realistic to use a high number of frequencies due to longer acquisition time and diminishing returns on accuracy. The number of phases used for acquisition has a similar impact to that of the

number of frequencies on the results. Finally, the acquisition wavelengths have to be chosen depending on the fluorescence quantification algorithm used.

For the first parameter, the goal was to reduce the number of frequencies while remaining under a defined acceptable error threshold of 5% for both optical properties. To have an accurate reconstruction of the surface with profilometry, the minimal number of frequencies was set to 5. The frequencies used were determined by first making SFDI measurements with a large range of frequencies (0 to 0.45 mm^{-1}) on a 72 optical phantom dataset with μ_a = 0.022-0.44 mm^{-1} and μ_s' = 0.72-2.16 mm^{-1}. The number of phases was fixed to four due to the use of a pre-existing profilometry algorithm for SFDI sample geometry corrections, mentioned in section 4.2. Intermediate data, more precisely the M_{AC}, introduced in section 2.1.4, from a subset of phantoms is shown in figure 6.6. It was observed that there is a larger difference between the M_{AC} of phantoms at lower frequencies, which reduces coupling between different sets of optical properties. These frequencies were favored for reconstruction.

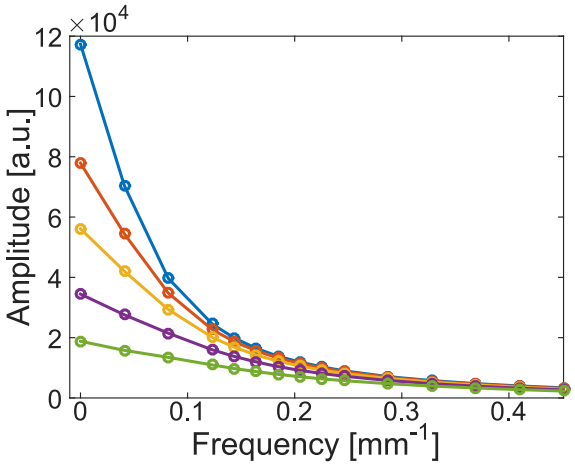

Figure 6.6 Spatial frequency domain imaging M_{AC} amplitude curves acquired with the multimodal imaging system at multiple frequencies on sample optical phantoms with various absorption and scattering properties.

Using all 15 frequencies in the range, errors of 5.54% for absorption (μ_a) and 4.34% for scattering (μ_s') were obtained. After optimization, it was found that the use of six frequencies (0.041; 0.082; 0.123; 0.144; 0.164; 0.246 mm^{-1}) was best, with errors of 5.25% and 3.87% for absorption and scattering respectively. This represented an increase in accuracy compared to the full number of frequencies, which may be explained by the high coupling in higher frequencies introducing errors in the inversion problem. The error on absorption remained slightly higher than the targeted threshold, but accuracy gains made by using more than 6 frequencies were not considered significant enough to justify the added acquisition time.

For the acquisition wavelength, although multiple model-based correction techniques were presented in section 2.3.3, the method by Kim *et al.* (Eq. 2.15) was selected. The method used by Yang *et al.* (Eq. 2.10) requires system-specific fitting, which was to be avoided due to the initial changing prototype nature of the system, and additional use of the SFDI lookup-table. The method used by Gardner *et al.* (Eq. 2.12) was also put aside since it uses the optical properties of the emission wavelengths, which would greatly extend acquisition time for endogenous fluorescence.

For the quantification method by Kim et al., the SFDI acquisition wavelength is the same as the fluorescence excitation wavelength. However, some preliminary tests on biological tissue showed that the signal obtained was too low to be detected at a reasonable SNR at 405 nm. This was due both to peak absorption by chromophores and low system transmission, as demonstrated in section 6.1.3.2. Consequently, the choice was made to measure at 435 nm, which coincided with the intensity peak of the second LED source. This LED had a power of 290 mW (compared to 205 mW at 405 nm) and remained close to the chromophore peaks, meaning it was an adequate estimation of the optical properties at 405 nm. This compromise was not expected to have a significant impact on the final results.

6.2.2 Fluorescence and reflectance acquisitions

A challenge regarding the acquisition of fluorescence and reflectance was the large variation of the sensitivity of the system over the spectral band of interest from 420 to 650 nm, as previously noted in figure 6.5. In imaging, it is good practice to use ~80% of the dynamic range of the camera to obtain optimal SNR. For the system, if the acquisition time was set to this target for the lower wavelengths, the higher wavelengths would saturate, whereas if it was set with the higher wavelengths, the SNR of lower wavelengths would be too low. It would have been possible to account for this problem by reducing the source intensity at higher wavelengths but it was chosen to use a solution minimizing the acquisition time by implementing an automatic exposure time control in the Labview software.

At each acquisition wavelength, the camera took a quick preliminary snapshot of the sample. The maximal value of intensity on that image was reported as a fraction of the targeted intensity. This was then converted to a multiplicative factor to the preliminary snapshot integration time, since intensity scaled linearly with time for the system, and thus gave the exposure time necessary to reach target intensity. The algorithm was also implemented for SFDI measurements to streamline the acquisition process. One caveat of the technique was that specular reflections on the tissue had to be minimized to have a valid maximal intensity on the snapshot image. Possible improvements may include the control of repeat acquisitions

to reach a target SNR.

6.2.3 Control of specular reflections

Avoiding specular reflections was a major concern in biological tissue, as those provide no information and thus remove portions of the image from the analysis. Although this was not a problem for fluorescence, since the excitation source was completely cut off from the measurements, reflectance and SFDI were both subject to the phenomenon. A demonstration of a prostate measurement with specular reflections is shown in figure 6.7.

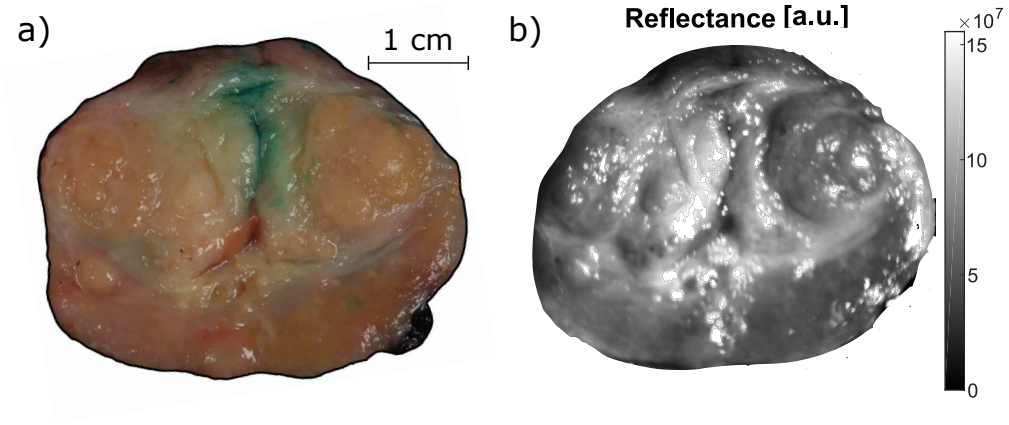

Figure 6.7 (a) Reference picture of a prostate along with (b) area under curve of reflectance acquisition using the multimodal imaging system and featuring specular reflection artefacts.

The first approach to this problem was to use angular projection to avoid placing the camera directly in the path of the reflected source. This method proved efficient for simple flat geometries, like that of optical phantoms but, since biological tissues have an uneven surface, it was not appropriate for prostate sample measurements. The second approach was the use of crossed polarisers. This technique exploits the fact that specular reflections conserve the initial polarisation of the source, whereas diffuse reflectance is unpolarised. Therefore, a preferential polarisation is given to the source by a first polariser and, by orienting a second polariser at 90° relative to the first one, that polarisation is cut off at detection. This method causes an important loss in signal since each polariser has a transmission of 50% for unpolarized light, thus, with two polarisers, only 25% of the possible signal is detected. However, when applied to the imaging system, additional adjustments had to be made to the technique.

6.2.3.1 System preferential polarisation

The initial implementation of the crossed polarisers method was unsuccessful due to very low SNR. This was due to the preferential polarisation of elements in the imaging system. Upon investigation, it was found that the source itself was polarized, meaning there would be an orientation for the polarisers in both excitation branches maximizing the intensity projected on the tissue. For SFDI projection, there were no polarising elements inside the CEL5500, meaning the collimator/CEL5500 connection angle did not have to be adjusted. Tests using a power-meter showed that the intensity variation between the polariser position maximizing and minimizing output was of ~25% for the reflectance excitation and ~30% for the SFDI excitation. For the detection branch, the LCTF was the only element with preferential polarisation and caused an intensity variation of ~26%. This meant there was an orientation of the detection polariser relative to the LCTF maximizing detection intensity.

Although individually manageable, the combination of these effects was challenging to account for, since excitation and detection polariser also had to be crossed. The orientation of the projection polariser maximizing projected intensity did not correspond to the orientation of the detection polariser maximizing detected intensity. Several techniques, such as tests on highly reflective samples or biological samples, were attempted to find a single optimal orientation of all system components to maximize detection and projection while eliminating specular reflections on the sample. However, it was not possible for a single orientation of the components to eliminate specular reflections for multiple samples. This was most likely because a specific tissue sample preferentially reflects certain polarisations. While individual variations in the intensity of each component did not appear overly high, practical tests showed that optimizing each of the parts for every acquisition may increase detected power upwards of an order of magnitude.

Therefore, it was chosen to manually adjust both the excitation and detection polarisers prior to acquisition to optimize case-by-case the detected intensity. Although the acquisition process was more tedious as a consequence, having the highest possible SNR was crucial for the quality of the final results. This meant the acquisition process required three adjustment steps:

1. Adjust the detection polariser to maximize fluorescence detection ;
2. Adjust the excitation and detection polarisers to maximize reflectance detection while eliminating specular reflections ;
3. Adjust the excitation and detection polarisers to maximize SFDI detection while eliminating specular reflections.

6.2.3.2 Data considerations with polarisation adjustements

Since the adjustment of each polariser varied from sample to sample, the excitation power, as well as the fraction of light detected, also changed. Thus, it was impossible to compare results on an absolute intensity basis. Only the optical properties, since they were reconstructed from a reference measurement taken for each acquisition, were compared directly. For quantified fluorescence, features such as the spectral shape, ratios between intensities on the curve or more general observations, regarding a relative increase in intensity when comparing histopathological regions, for example, may be used as a basis for comparison. If spectral unmixing was added to the data treatment, concentrations of fluorophores may also be compared.

6.3 Mathematical detail of calibration process

To elaborate the calibration process for fluorescence and reflectance, shown in figure 4.2, a theoretical study of the signal was done. It should be noted that, to simplify representation and since it should not influence the process, polarisation was left out of these equations. The dependence in wavelength of the parameters was denoted with a λ subscript.

The tissue signal $\boldsymbol{S}$ was modeled as the source intensity I modified according to tissue properties $\boldsymbol{F}$

$$\mathbf{S}_\lambda\mathbf{(x,y)} = I_\lambda(x,y) * \mathbf{F}_\lambda\mathbf{(x,y)} + \mathbf{BG}_\lambda\mathbf{(x,y)}. \tag{6.1}$$

The background signal **BG** was also included in this tissue signal. For the detected signal $\boldsymbol{D}$, $\boldsymbol{S}$ was influenced by the system's response *rf*, which is a representation of system transmission varying with wavelength. The detection optics also generated their own fluorescence signal *af* when excited by $\boldsymbol{S}$. Additionally, the camera detector used had its own detection efficiency QE and took the measurement at a set integration time Δt. Thus,

$$\mathbf{D}_\lambda\mathbf{(x,y)} = \{rf_\lambda * (\mathbf{S}_\lambda\mathbf{(x,y)} + af_\lambda * \mathbf{S}_\lambda\mathbf{(x,y)})\} * QE_\lambda * \Delta t. \tag{6.2}$$

As can be observed, the measurement of interest $\boldsymbol{F}$ was initially far from the only detected signal, justifying the calibration process. The first calibration measurement was background removal. To obtain these dark noise images DK, an acquisition was taken without any signal excitation

$$DK_\lambda(x,y) = QE_\lambda * \Delta t_{DK} \left\{ rf_\lambda * (\mathbf{BG_\lambda(x,y)} + af_\lambda * \mathbf{BG_\lambda(x,y)}) \right\}. \tag{6.3}$$

It was noted that the measurement depends on its own acquisition time (Δt_{DK}). A correction to remove the Δt from all measurements was to divide the acquisitions by their respective integration times. This process referred to as acquisition time normalization, could only be done since the signal is linear with exposure time for the camera used in the system. This was done in eq. 6.2, 6.3 and in all subsequent calibration measurements, where the Δt factor is not transcribed.

The second step was the shading correction R, which allowed the correction of the unevenness of illumination and spectral shape of the source. This measurement was done on a spectralon reflectance standard (Labsphere, QC, CAN) which has an even reflectance of 99.9% across all wavelengths of interest. In essence, this acquisition was a direct measurement of the source projection on the sample without the influence of the tissue F

$$R_\lambda(x,y) = \{ rf_\lambda * [(I_\lambda(x,y) + \mathbf{BG_\lambda(x,y)}) + af_\lambda * (I_\lambda(x,y) + \mathbf{BG_\lambda(x,y)})] \} * QE_\lambda. \tag{6.4}$$

Note that the **BG** was removed from this measurement using the dark noise images (eq. 6.3). Since information would be lost by dividing the detected signal **D** by R, the shading correction needed to be normalized. Here, a distinction was made between reflectance and fluorescence; reflectance used a hyperspectral R measurement but fluorescence only used R at a single wavelength. This is because the source was cut off from the fluorescence measurements, meaning the correction for the spectral shape of I was not needed. Both of these R corrections were normalized by the maximum value of the dataset, resulting in R_{01} that was used for the calibration

$$R_{01,\lambda}(x,y) = I_\lambda(x,y) + af_\lambda * I_\lambda(x,y). \tag{6.5}$$

The third and final step before quantification was the relative intensity correction RIC, used to correct for system transmission and camera detection efficiency. A calibration lamp with a known emission intensity I_{lamp} was measured directly and divided by its reference intensity spectrum. This generated a correction curve:

$$
\begin{aligned}
RIC_\lambda &= \frac{\{rf_\lambda * [I_{lamp,\lambda} + \mathbf{BG_\lambda(x,y)}]\} * QE_\lambda}{I_{lamp,\lambda}}, \\
&= \frac{\{rf_\lambda * I_{lamp,\lambda}\} * QE_\lambda}{I_{lamp,\lambda}}, \\
&= QE_\lambda * rf_\lambda.
\end{aligned} \tag{6.6}
$$

By using all the calibration measurements (DK, R, RIC) as demonstrated in the flowchart (Fig. 4.2), undesired factors were removed from the initial detected signal modeled in equation 6.2. The subsequent treatment of fluorescence quantification was used to quantify the resulting tissue response

$$
\begin{aligned}
\mathbf{D}_{processed,\lambda}\mathbf{(x,y)} &= \frac{\mathbf{D_\lambda(x,y)} - DK_\lambda(x,y)}{R_{01,\lambda}(x,y) * RIC_\lambda}, \\
&= \frac{\{rf_\lambda * [(I_\lambda(x,y) * \mathbf{F_\lambda(x,y)}) + af_\lambda * (I_\lambda(x,y) * \mathbf{F_\lambda(x,y)})]\} * QE_\lambda}{R_{01,\lambda}(x,y) * RIC_\lambda}, \\
&= \frac{\{rf_\lambda * \mathbf{F_\lambda(x,y)}\} * QE_\lambda}{RIC_\lambda}, \\
&= \mathbf{F_\lambda(x,y)}.
\end{aligned} \tag{6.7}
$$

6.4 Current system limitations

6.4.1 Spectral analysis range

While the LCTF has an operational range from 400 to 720 nm, the detection range was limited from 420 to 650nm. The lower limit was placed to cut the fluorescence excitation source and the upper limit was caused by the spectral range of the source. Without this restriction due to source range, additional information may be obtained from the fluorescence of the tissue closer to the infra-red region, notably from the porphyrins as can be seen in table 2.1. The usage a UV excitation light, which would excite additional fluorophores and be further from the hemoglobin and deoxy-hemoglobin absorption peaks, was also impossible with the current system because, additionally to the range of the LCTF, the DLP used for SFDI was unsuited for use with light beneath 400 nm as both the optics of the CEL5500 and the micromirror chip itself experience a severe degradation in performance in the UV regime.

6.4.2 Sample height

When evaluating the depth of field of the system, a value of 1.5 cm was determined. Although it was found that profilometry corrections can still work beyond that range, up to about 2.4 cm, the system is restricted in regards to other samples. Most notably, full prostates, for the considered *in vivo* robotic surgery application, exceed 1.5 cm in height.

6.4.2.1 Signal

The camera used for the system has a maximal integration time of 10 seconds. In practice, this meant that, for low signal cases, the image intensity would not reach the target 80% of the dynamic range, leading to inferior SNR. This was a problem for the near-UV wavelengths with lower transmission and highlighted a more general problem with the system; the detected signal is very low. One notable issue is that the excitation power for SFDI is particularly low due to the losses in the DLP system, as determined in section 6.1.2.2. This also made current acquisition times too long for immediate clinical application despite respecting the initial 30 minutes limit.

6.5 Expected challenges of *in vivo* transition

6.5.1 System design & Acquisition

In both categories of RP, presented in section 2.3.4, the size of the surgical cavity is a restrictive factor; especially in the considered application of the system to laparoscopic robot-assisted surgeries. Although the detection branch and excitation branches could be mounted on arms, they are not flexible and their insertion diameters would be of 31.3 and 25.4 mm respectively, which is larger than typical laparoscopic incisions. The manual adjustment of the polarizers for the acquisition and manual switching of the excitation source between fluorescence and SFDI branches are also unsuitable to the surgical workflow and would need to be automated. The system would likely require a major re-design for robotic-surgery.

For signal strength, although fluorescence is stronger *in vivo*, tissue absorption is also higher due to the high concentrations of blood. This is expected to pose a challenge for the SFDI measurements, which suffered in *ex vivo* from low excitation power and SNR. This problematic is also related to the acquisition time of the system, which is currently too long for the *in vivo* context. Ideally, it should be reduced to under a minute. Consequently, improvements in excitation power, system transmission, or even SFDI acquisition technique, would be necessary for the RP context.

One other point of concern is the depth of the surgical cavity, which exceeds the current system depth of field. This would in practice limit the view field of the system to a specific area of interest, such as the prostate surface or a specific zone of surrounding tissue, with minimal height variations. Improving depth of field would be critical to the *in vivo* implementation of the system.

6.5.2 Processing

Some aspects of the system already account for certain challenges expected in the surgical context. Notably, the effect of local blood concentrations, which would affect tissue absorption and thus fluorescence emission, is corrected by the fluorescence quantification algorithm. The presence of background light is also corrected in processing. While it is not expected to be an important factor in the robot-assisted surgical context, due to the closed surgical cavity, direct exposure from surgical lights could be a problem if the system is used in open surgery. The lights could cause specular reflection artefacts on the image. However, temporarily shutting off the surgical lights for the acquisition should be sufficient to resolve the problem.

The currently used calibration measurements are appropriate for the *in vivo* context, as they are conducted on optical phantoms and could be done before or after surgery; they would not impact procedure length. Furthermore, while the 24 mm range for which the SFDI profilometry correction was validated is appropriate for imaging the prostate and its surroundings during surgery, it is not sufficient proof in the case of imaging the whole surgical cavity. Thus, the algorithm should be tested on larger height variations following an improvement of system depth of field. However, it is not expected to require modifications. An important additional correction step should also be implemented to correct for possible tissue movement, due to factors such as breathing, during acquisition.

Although it was not considered for *ex vivo* measurements, the processing time is an important factor to deliver results quickly during surgery. SFDI processing time is highly variable since it depends on the precision used in the lookup table. For the results presented in the article, the processing time was of ~2 min for SFDI. Processing fluorescence, reflectance and obtaining quantified fluorescence for that sample took ~1.5 min. This totals 3.5 minutes for processing on a standard laptop with 16 gigabytes of RAM. It is important to note that no attention was paid to the optimization of the initial data treatment code since time was not a constraint in the *ex vivo* context. However, since the acquisition time goal for *in vivo* is of under a minute, a rework of the program would be necessary to achieve a corresponding processing time.

6.5.3 Analysis of results

As stated in the article, only a single prostate sample was analyzed in this study. This severely limits the conclusions that can be drawn for the results. While the sample presented was not preferentially selected and other samples should not present significantly different results, there is no evidence that the success of the statistical analysis will extend to other prostate specimens. To complete the proof-of-concept, it is a priority to make additional measurements to conduct a robust analysis with advanced methods (*e.g.* machine learning) and to test if it the acquired biomarkers allow correct identification biological prostate regions and cancerous/benign tissue when compared to the gold standard. Following this validation on *ex vivo* tissue, the same process could be started *in vivo* during RP, which, if successful, could lead to clinical adoption.

CHAPTER 7 CONCLUSION & RECOMMENDATIONS

For this project, a multimodal imaging system, combining endogenous fluorescence, diffuse reflectance, and SFDI, was conceived and applied to radical prostatectomy samples to produce snapshot whole-organ maps of quantitative biomarkers usable for pathological analysis and tissue differentiation. To our knowledge, this was the first system using SFDI to quantify wide-field endogenous fluorescence measurements and the first to image endogenous fluorescence, diffuse reflectance, and SFDI on the radical prostatectomy specimens in wide-field.

First, reflectance and fluorescence spectroscopy, as well as SFDI, had to be integrated into a single system. The optical conception was done according to specifications tailored for the application on the prostate; with the final specifications of a FOV of 5.5 x 5.5 cm, resolution of 70 μm and depth of field of 1.5 cm. For excitation, a single multi-LED source was used for fluorescence, reflectance and SFDI acquisitions, while for detection a LCTF was coupled to a CMOS camera. The system control software was programmed on Labview; this allowed simultaneous control of the instruments and optimal acquisition times. Robust calibration and data treatment processes were determined for every modality and tested on optical phantoms. This led to the optimization of the acquisition processes, with reflectance and fluorescence captured from 420-650 nm and SFDI measured at 435 nm with 6 frequencies and 4 phases. Further tests were made for the modalities on optical phantoms, which quantified the accuracy of SFDI to 5.2% and 4.4% for absorption and scattering, respectively, over a range of optical properties suitable for the application, and justified the selection and implementation of the fluorescence quantification technique developed by Kim *et al.*

Second, the system had to be adapted for measurements on prostate samples. Crossed polarisers were implemented in the system while considering the preferential polarisation of existing optical elements to avoid specular reflections on biological tissue and maintain sufficient signal. A SFDI profilometry algorithm for sample geometry corrections was also implemented and validated for height variations of 24 mm, reducing errors from 127% to 3.3% for μ_a and from 28% to 2.5% for μ'_s. Finally, measurements were conducted on prostate samples obtained in collaboration with the CHUM. The measured biomarkers were studied against a histopathological gold standard, which allowed a trained pathologist to identify prostate regions and benign *vs* malign tissue. Despite a sample number too low to conduct proper tissue differentiation, preliminary statistical analyses showed that the acquired biomarkers provided statistically significant differences between both prostatic *vs* extra-prostatic tissue and benign *vs* malign tissues.

Acquisitions on a high number (>20) of prostates would allow for a more thorough statistical analysis of the samples and potentially prove the power of the system to differentiate several tissue types and allow targeted resection. However, the current system remains limited in regards to spectral analysis range, depth of focus and acquisition time. Adaptations would also need to be made to system design, as well as acquisition and data processing methods before *in vivo* use in robot-assisted radical prostatectomy procedures. Several aspects of the system could be improved to address these problems and improve its clinical relevance. The optical design of the illumination and detection branches could be re-thought to allow measurements in the UV, improve the depth of field and make the system more compact. Approaches to improve acquisition time and signal strength would be to replace the LCTF with a filter wheel targeting specific spectral bands of interest, which would also have the benefit of reducing processing time, or use a more powerful source in the excitation branch since the current exposition is ~2 orders of magnitude under ANSI safety standards. A new DLP system could also be acquired, or one be custom-made for the system, to increase transmission, improving acquisition time, and to be compatible with UV wavelengths. Advanced SFDI data processing techniques such as SSOP could also be implemented to speed up the acquisition and processing of this modality.

REFERENCES

[1] N. Ramanujam, "Fluorescence Spectroscopy of Neoplastic and Non-Neoplastic Tissues," *Neoplasia*, vol. 2, no. 1-2, pp. 89–117, 2000.

[2] R. Richards-Kortum and E. Sevick-Muraca, "Quantitative Optical Spectroscopy for Tissue Diagnosis," *Annual Review of Physical Chemistry*, vol. 47, no. 1, pp. 555–606, 1996.

[3] A. Kluftinger *et al.*, "Detection of squamous cell cancer and pre-cancerous lesions by imaging of tissue autofluorescence in the hamster cheek pouch model," *Surgical Oncology*, vol. 1, no. 2, pp. 183–188, 1992.

[4] K. Koenig and H. Schneckenburger, "Laser-induced autofluorescence for medical diagnosis," *Journal of Fluorescence*, vol. 4, no. 1, pp. 17–40, 1994.

[5] J. L. Sandell and T. C. Zhu, "A review of in-vivo optical properties of human tissues and its impact on PDT," *Journal of Biophotonics*, vol. 4, no. 11-12, pp. 773–787, 2011.

[6] B. Yang, M. Sharma, and J. W. Tunnell, "Attenuation-corrected fluorescence extraction for image-guided surgery in spatial frequency domain," *Journal of Biomedical Optics*, vol. 18, no. 8, p. 080503, 2013.

[7] M. M. Center *et al.*, "International variation in prostate cancer incidence and mortality rates," *European Urology*, vol. 61, no. 6, pp. 1079–1092, 2012.

[8] A. W. Hsing, L. Tsao, and S. S. Devesa, "International comparisons of prostate cancer incidence and mortality," *International Journal of Cancer*, vol. 85, no. July 1999, pp. 60–67, 2000.

[9] C. G. Roehrborn and L. K. Black, "The economic burden of prostate cancer," *BJU International*, vol. 108, no. 6, pp. 806–813, 2011.

[10] S. R. Denmeade *et al.*, "A history of prostate cancer treatment," vol. 2, no. 5, pp. 389–396, 2014.

[11] G. D. Grossfeld *et al.*, "Impact of Positive Surgical Margins on Prostate Cancer Recurrence and the Use of Secondary Cancer Treatment: Data From the Capsure Database," *The Journal of Urology*, vol. 163, no. 4, pp. 1171–1177, 2000.

[12] I. D. Nagtegaal *et al.*, "Circumferential Margin Involvement Is Still an Important Predictor of Local Recurrence in Rectal Carcinoma Not One Millimeter but Two Millimeters Is the Limit," *American Journal of Surgical Pathology*, vol. 26, no. 3, pp. 350–357, 2002.

[13] W. Stummer *et al.*, "Counterbalancing risks and gains from extended resections in malignant glioma surgery: a supplemental analysis from the randomized 5-aminolevulinic acid glioma resection study," *Journal of Neurosurgery*, vol. 114, no. 3, pp. 613–623, 2010.

[14] B. J. Davis *et al.*, "The radial distance of extraprostatic extension of prostate carcinoma: Implications for prostate brachytherapy," *Cancer*, vol. 85, no. 12, pp. 2630–2637, 1999.

[15] A. Nakao *et al.*, "Extended Radical Resection Versus Standard Resection for," *Pancreas*, vol. 28, no. 3, pp. 289–292, 2004.

[16] D. A. Orringer, A. Golby, and F. Jolesz, "Neuronavigation in the surgical management of brain tumors: Current and future trends," *Expert Review of Medical Devices*, vol. 9, no. 5, pp. 491–500, 2012.

[17] C. Urban *et al.*, "Comparative Study of Surgical Margins in Oncoplastic Surgery and Quadrantectomy in Breast Cancer," *Annals of Surgical Oncology*, vol. 12, no. 7, pp. 539–545, 2005.

[18] G. Ayala *et al.*, "Reactive Stroma as a Predictor of Biochemical-Free Recurrence in Prostate Cancer," *Clinical Cancer Research*, vol. 9, no. 13, pp. 4792–4801, 2003.

[19] J. A. Halpern *et al.*, "Indications, Utilization and Complications Following Prostate Biopsy: New York State Analysis," *Journal of Urology*, vol. 197, no. 4, pp. 1020–1025, 2017.

[20] M. Müntener *et al.*, "Prognostic Significance of Gleason Score Discrepancies between Needle Biopsy and Radical Prostatectomy," *European Urology*, vol. 53, no. 4, pp. 767–776, 2008.

[21] M. G. Sanda *et al.*, "Quality of Life and Satisfaction with Outcome among Prostate-Cancer Surviviors," *The New England Journal of Medicine*, vol. 358, no. 12, pp. 1250–1261, 2008.

[22] J. L. Stanford *et al.*, "After Radical Prostatectomy for Clinically Localized Prostate Cancer The Prostate Cancer Outcomes Study," vol. 1024, 2015.

[23] O. Yossepowitch *et al.*, "Positive Surgical Margins in Radical Prostatectomy: Outlining the Problem and Its Long-Term Consequences," *European Urology*, vol. 55, no. 1, pp. 87–99, 2009.

[24] M. L. Blute *et al.*, "Anatomic site-specific positive margins in organ-confined prostate cancer and its impact on outcome after radical prostatectomy," *Urology*, vol. 50, no. 5, pp. 733–739, 1997.

[25] S. Rais-Bahrami *et al.*, "Optical Coherence Tomography of Cavernous Nerves: A Step Toward Real-Time Intraoperative Imaging During Nerve-Sparing Radical Prostatectomy," *Urology*, vol. 72, no. 1, pp. 198–204, 2008.

[26] P. Crow *et al.*, "Optical diagnostics in urology: Current applications and future prospects," *BJU International*, vol. 92, no. 4, pp. 400–407, 2003.

[27] O. M. A'Amar *et al.*, "Comparison of elastic scattering spectroscopy with histology in ex vivo prostate glands: Potential application for optically guided biopsy and directed treatment," *Lasers in Medical Science*, vol. 28, no. 5, pp. 1323–1329, 2013.

[28] D. Zaak *et al.*, "Photodynamic Diagnosis of Prostate Cancer Using 5-Aminolevulinic Acid—First Clinical Experiences," *Urology*, vol. 72, no. 2, pp. 345–348, 2008.

[29] J. Ebenezar *et al.*, "Stokes shift spectroscopy pilot study for cancerous and normal prostate tissues," *Optics Letters*, vol. 37, no. 16, p. 3360, 2012.

[30] G. Marriott *et al.*, "Time resolved imaging microscopy. Phosphorescence and delayed fluorescence imaging," *Biophysical Journal*, vol. 60, no. 6, pp. 1374–1387, 1991.

[31] J. Haringsma and G. N. Tytgat, "Fluorescence and autofluorescence," *Bailliere's Best Practice and Research in Clinical Gastroenterology*, vol. 13, no. 1, pp. 1–10, 1999.

[32] M. S. Patterson and B. W. Pogue, "Mathematical model for time-resolved and frequency-domain fluorescence spectroscopy in biological tissues," *Applied Optics*, vol. 33, no. 10, pp. 1963–1974, 1994.

[33] R. S. Bradley and M. S. Thorniley, "A review of attenuation correction techniques for tissue fluorescence," *Journal of The Royal Society Interface*, vol. 3, no. 6, pp. 1–13, 2006.

[34] D. J. Cuccia *et al.*, "Quantitation and mapping of tissue optical properties using modulated imaging," *Journal of Biomedical Optics*, vol. 14, no. 2, p. 024012, 2009.

[35] A. M. Laughney *et al.*, "Spectral discrimination of breast pathologies in situ using spatial frequency domain imaging," *Breast Cancer Research*, vol. 15, no. 4, 2013.

[36] M. S. Patterson, B. C. Wilson, and D. R. Wyman, "The propagation of optical radiation in tissue. II: Optical properties of tissues and resulting fluence distributions," *Lasers in Medical Science*, vol. 6, no. 4, pp. 379–390, 1991.

[37] T. Vo-Dinh and B. R. Masters, *Biomedical Photonics Handbook*, 2nd ed. Boca Raton, Florida: CRC Press, 2004, vol. 1.

[38] S. L. Jacques, "Optical properties of biological tissues: A review," *Physics in Medicine and Biology*, vol. 58, no. 11, 2013.

[39] G. Lu and B. Fei, "Medical hyperspectral imaging: a review," *Journal of Biomedical Optics*, vol. 19, no. 1, p. 010901, 2014.

[40] W.-F. Cheong, S. A. Prahl, and A. J. Welch, "A Review of the Optical Properties of Biological Tissues," *IEEE Journal of Quantum Electronics*, vol. 26, no. 12, pp. 2166–2185, 1990.

[41] L. O. Svaasand *et al.*, "Reflectance measurements of layered media with diffuse photon-density waves: A potential tool for evaluating deep burns and subcutaneous lesions," *Physics in Medicine and Biology*, vol. 44, no. 3, pp. 801–813, 1999.

[42] B. C. Wilson and G. Adam, "A Monte Carlo Model for the Absorption and Flux Distributions of Light in Tissue," *Medical Physics*, vol. 10, no. 6, pp. 824–830, 1983.

[43] C. M. Gardner, S. L. Jacques, and A. J. Welch, "Fluorescence spectroscopy of tissue: recovery of intrinsic fluorescence from measured fluorescence," *Applied Optics*, vol. 35, no. 10, p. 1780, 1996.

[44] J. Wu, M. S. Feld, and R. P. Rava, "Analytical model for extracting intrinsic fluorescence in turbid media," *Applied Optics*, vol. 32, no. 19, p. 3585, 1993.

[45] G. Zonios *et al.*, "Diffuse reflectance spectroscopy of human adenomatous colon polyps in vivo," *Applied Optics*, vol. 38, no. 31, p. 6628, 1999.

[46] A. A. Oraevsky, S. L. Jacques, and F. K. Tittel, "Measurement of tissue optical properties by time-resolved detection of laser-induced transient stress," *Applied Optics*, vol. 36, no. 1, p. 402, 1997.

[47] F. Stelzle *et al.*, "Diffuse reflectance spectroscopy for optical soft tissue differentiation as remote feedback control for tissue-specific laser surgery," *Lasers in Surgery and Medicine*, vol. 42, no. 4, pp. 319–325, 2010.

[48] G. Yu *et al.*, "Real-time in situ monitoring of human prostate photodynamic therapy with diffuse light." *Photochemistry and photobiology*, vol. 82, no. 5, pp. 1279–84, 2006.

[49] Y. Pu *et al.*, "Determination of optical coefficients and fractal dimensional parameters of cancerous and normal prostate tissues," *Applied Spectroscopy*, vol. 66, no. 7, pp. 828–834, 2012.

[50] B. W. Pogue and M. S. Patterson, "Review of tissue simulating phantoms for optical spectroscopy, imaging and dosimetry," *Journal of Biomedical Optics*, vol. 11, no. 4, p. 041102, 2006.

[51] S. L. Jacques and B. W. Pogue, "Tutorial on diffuse light transport," *Journal of Biomedical Optics*, vol. 13, no. 4, p. 041302, 2008.

[52] N. Bodenschatz *et al.*, "Model-based analysis on the influence of spatial frequency selection in spatial frequency domain imaging," *Applied Optics*, vol. 54, no. 22, p. 6725, 2015.

[53] ——, "Sources of errors in spatial frequency domain imaging of scattering media," *Journal of Biomedical Optics*, vol. 19, no. 7, p. 071405, 2014.

[54] J. Geng, "Structured-light 3D surface imaging: a tutorial," *Advances in Optics and Photonics*, vol. 3, no. 2, pp. 128–160, 2011.

[55] S. Gioux *et al.*, "Three-dimensional surface profile intensity correction for spatially modulated imaging," *Journal of Biomedical Optics*, vol. 14, no. 3, p. 034045, 2009.

[56] M. Sibai *et al.*, "Quantitative spatial frequency fluorescence imaging in the sub-diffusive domain for image-guided glioma resection," *Biomedical Optics Express*, vol. 6, no. 12, p. 4923, 2015.

[57] T. A. Erickson *et al.*, "Lookup-table method for imaging optical properties with structured illumination beyond the diffusion theory regime," *Journal of Biomedical Optics*, vol. 15, no. 3, p. 036013, 2010.

[58] S. C. Kanick *et al.*, "Sub-diffusive scattering parameter maps recovered using wide-field high-frequency structured light imaging," *Biomedical Optics Express*, vol. 5, no. 10, p. 3376, 2014.

[59] D. J. Cuccia *et al.*, "Modulated imaging: quantitative analysis and tomography of turbid media in the spatial-frequency domain," *Optics Letters*, vol. 30, no. 11, pp. 1354–1356, 2005.

[60] S. D. Konecky *et al.*, "Quantitative optical tomography of sub-surface heterogeneities using spatially modulated structured light," *Optics Express*, vol. 17, no. 17, pp. 14 780–14 790, 2009.

[61] ——, "Spatial frequency domain tomography of protoporphyrin IX fluorescence in preclinical glioma models," *Journal of Biomedical Optics*, vol. 17, no. 5, p. 056008, 2012.

[62] J. Vervandier and S. Gioux, "Single snapshot imaging of optical properties," *Biomedical Optics Express*, vol. 4, no. 12, p. 2938, 2013.

[63] M. van de Giessen, J. P. Angelo, and S. Gioux, "Real-time, profile-corrected single snapshot imaging of optical properties," *Biomedical Optics Express*, vol. 6, no. 10, p. 4051, 2015.

[64] M. Y. Berezin and S. Achilefu, "Fluorescence Lifetime Measurements and Biological Imaging," *Chemical Reviews*, vol. 110, no. 5, pp. 2641–2684, 2010.

[65] P. I. H. Bastiaens and A. Squire, "Fluorescence lifetime imaging microscopy: Spatial resolution of biochemical processes in the cell," *Trends in Cell Biology*, vol. 9, no. 2, pp. 48–52, 1999.

[66] S. Andersson-Engels *et al.*, "In vivo fluorescence imaging for tissue diagnostics," *Physics in Medicine and Biology*, vol. 42, no. 5, pp. 815–824, 1997.

[67] W. S. Tummers *et al.*, "Regulatory aspects of optical methods and exogenous targets for cancer detection," *Cancer Research*, vol. 77, no. 9, pp. 2197–2206, 2017.

[68] G. A. Wagnieres, W. M. Star, and B. C. Wilson, "ln Vivo Fluorescence Spectroscopy and lmaging for Oncological Applications of Technology," *Photochemistry*, vol. 68, no. 5, pp. 603–632, 1998.

[69] L. Z. Li, "Imaging mitochondrial redox potential and its possible link to tumor metastatic potential," *Journal of Bioenergetics and Biomembranes*, vol. 44, no. 6, pp. 645–653, 2012.

[70] V. Masilamani *et al.*, "Cancer diagnosis by autofluorescence of blood components," *Journal of Luminescence*, vol. 109, no. 3-4, pp. 143–154, 2004.

[71] A. Draaijer, R. Sanders, and H. Gerritsen, "Fluorescence lifetime imaging, a new tool in confocal microscopy," in *Handbook of biological confocal microscopy*. Springer, 1995, pp. 491–505.

[72] S. Saini, H. Singh, and B. Bagchi, "Fluorescence resonance energy transfer (FRET) in chemistry and biology: Non-Förster distance dependence of the FRET rate," *Journal of Chemical Sciences*, vol. 118, no. 1, pp. 23–35, 2006.

[73] T. K. Meyvis *et al.*, "Fluorescence recovery after photobleaching: a versatile tool for mobility and interaction measurements in pharmaceutical research," *Pharmaceutical research*, vol. 16, no. 8, pp. 1153–1162, 1999.

[74] C. Boudoux, *Fundamentals of Biomedical Optics*. Blurb, 2016.

[75] B. A. Flusberg *et al.*, "Fiber-optic fluorescence imaging," *Nature Methods*, vol. 2, no. 12, pp. 941–950, 2005.

[76] F. Leblond *et al.*, "Pre-clinical whole-body fluorescence imaging: Review of instruments, methods and applications," *Journal of Photochemistry and Photobiology B: Biology*, vol. 98, no. 1, pp. 77–94, 2010.

[77] W. C. Lin *et al.*, "In vivo brain tumor demarcation using optical spectroscopy," *Photochemistry and photobiology*, vol. 73, no. 4, pp. 396–402, 2001.

[78] J. C. Kennedy, S. L. Marcus, and R. H. Pottier, "Photodynamic Therapy (PDT) and Photodiagnosis (PD) Using Endogenous Photosensitization Induced by 5-Aminolevulinic Acid (ALA): Current Clinical and Development Status," *Journal of Clinical Laser Medicine & Surgery*, vol. 14, no. 5, pp. 289–304, 1996.

[79] B. W. Pogue *et al.*, "Review of neurosurgical fluorescence imaging methodologies," *Quantum*, pp. 1–30, 2010.

[80] P. A. Valdes *et al.*, "System and methods for wide-field quantitative fluorescence imaging during neurosurgery," *Optics Letters*, vol. 38, no. 15, p. 2786, 2013.

[81] B. Krammer and K. Plaetzer, "ALA and its clinical impact, from bench to bedside," *Photochemical and Photobiological Sciences*, vol. 7, no. 3, pp. 283–289, 2008.

[82] M. C. Grimbergen *et al.*, "Reduced specificity of 5-ALA induced fluorescence in photodynamic diagnosis of transitional cell carcinoma after previous intravesical therapy," *European Urology*, vol. 44, no. 1, pp. 51–56, 2003.

[83] V. Sharma *et al.*, "Prostate cancer detection using combined auto-fluorescence and light reflectance spectroscopy: ex vivo study of human prostates," *Biomedical Optics Express*, vol. 5, no. 5, p. 1512, 2014.

[84] Y. Pu *et al.*, "Stokes shift spectroscopic analysis of multifluorophores for human cancer detection in breast and prostate tissues," *Journal of biomedical optics*, vol. 18, no. 1, pp. 017 005–1–017 005–8, 2013.

[85] B. W. Pogue and G. Burke, "Fiber-optic bundle design for quantitative fluorescence measurement from tissue," *Appl. Optics*, vol. 37, no. 31, pp. 7429–7436, 1998.

[86] K. Vishwanath, B. Pogue, and M. A. Mycek, "Quantitative fluorescence lifetime spectroscopy in turbid media: Comparison of theoretical, experimental and computational methods," *Physics in Medicine and Biology*, vol. 47, no. 18, pp. 3387–3405, 2002.

[87] V. Ntziachristos *et al.*, "Planar fluorescence imaging using normalized data," *Journal of Biomedical Optics*, vol. 10, no. 6, p. 064007, 2005.

[88] J. M. Coremans *et al.*, "(Semi-)quantitative analysis of reduced nicotinamide adenine dinucleotide fluorescence images of blood-perfused rat heart," *Biophysical Journal*, vol. 72, no. 4, pp. 1849–1860, 1997.

[89] L. Szyc *et al.*, "Development of a handheld fluorescence imaging camera for intraoperative sentinel lymph node mapping," *Journal of Biomedical Optics*, vol. 20, no. 5, p. 051025, 2015.

[90] P. A. Valdés *et al.*, "A spectrally constrained dual-band normalization technique for protoporphyrin IX quantification in fluorescence-guided surgery," *Optics Letters*, vol. 37, no. 11, p. 1817, 2012.

[91] ——, "Quantitative, spectrally-resolved intraoperative fluorescence imaging," *Scientific Reports*, vol. 2, no. 1, p. 798, 2012.

[92] ——, "Optical technologies for intraoperative neurosurgical guidance," *Neurosurgical Focus*, vol. 40, no. March, pp. 1–18, 2016.

[93] Q. Zhang *et al.*, "Turbidity-free fluorescence spectroscopy of biological tissue," *Optics letters*, vol. 25, no. 19, pp. 1451–1453, 2000.

[94] R. B. Saager *et al.*, "Quantitative fluorescence imaging of protoporphyrin IX through determination of tissue optical properties in the spatial frequency domain," *Journal of Biomedical Optics*, vol. 16, no. 12, p. 126013, 2011.

[95] U. Sunar *et al.*, "Quantification of PpIX concentration in basal cell carcinoma and squamous cell carcinoma models using spatial frequency domain imaging," *Biomedical Optics Express*, vol. 4, no. 4, p. 531, 2013.

[96] J. Kress *et al.*, "A dual-channel endoscope for quantitative imaging, monitoring, and triggering of doxorubicin release from liposomes in living mice," *Scientific Reports*, vol. 7, no. 1, pp. 1–13, 2017.

[97] A. Kim, Y. Moriyama, and B. C. Wilson, "Quantification of in vivo fluorescence decoupled from the effects of tissue optical properties using fiber-optic spectroscopy measurements," *Journal of Biomedical Optics*, vol. 15, no. December 2010, pp. 1–12, 2010.

[98] P. A. Valdés *et al.*, "qF-SSOP: real-time optical property corrected fluorescence imaging," *Biomedical Optics Express*, vol. 8, no. 8, p. 3597, 2017.

[99] "EAU guidelines on prostate cancer. Part 1: Screening, diagnosis, and local treatment with curative intent - Update 2013," *European Urology*, vol. 65, no. 1, pp. 124–137, 2014. [Online]. Available: http://dx.doi.org/10.1016/j.eururo.2013.09.046

[100] P. M. Schlag *et al.*, *Prostate cancer*, ch. 10, pp. 163–178.

[101] D. V. Makarov *et al.*, "The association between diffusion of the surgical robot and radical prostatectomy rates," *Medical Care*, vol. 49, no. 4, pp. 333–339, 2011.

[102] A. Al-Aown *et al.*, "Laparoscopic simple prostatectomy: A reasonable option for large prostatic adenomas," *Urology Annals*, vol. 7, no. 3, pp. 297–302, 2015.

[103] V. Ficarra *et al.*, "Retropubic, Laparoscopic, and Robot-Assisted Radical Prostatectomy: A Systematic Review and Cumulative Analysis of Comparative Studies," *European Urology*, vol. 55, no. 5, pp. 1037–1063, 2009.

APPENDIX A LABVIEW SOFTWARE GUI

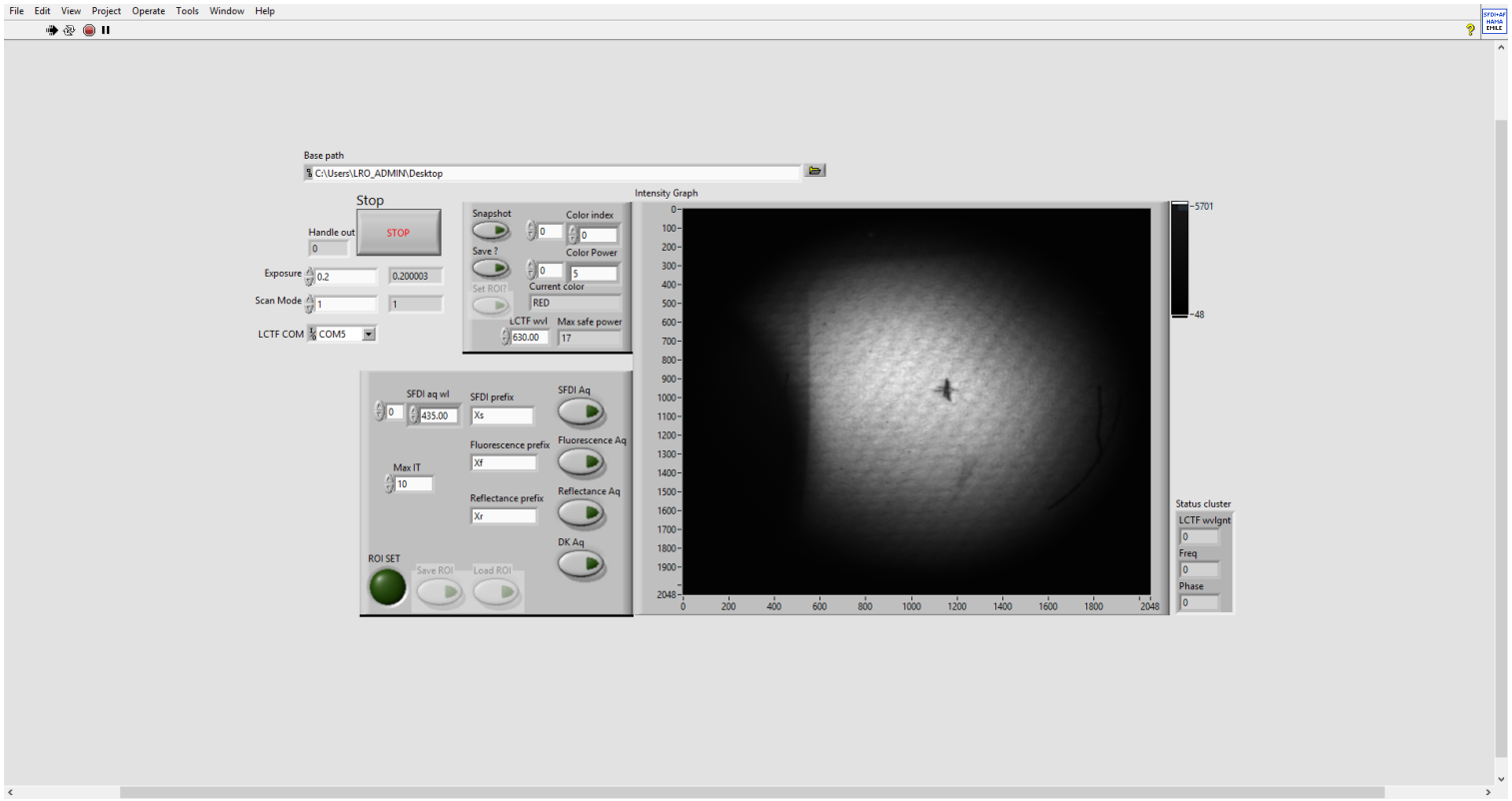

Figure A.1 User interface of the Labview acquisition software for the multimodal imaging system.